CONVECTION-ENHANCED DELIVERY OF MACROMOLECULES TO THE BRAIN USING ELECTROKINETIC TRANSPORT

by

Amir Hussein Faraji

Bachelor of Science in Chemistry, University of Florida, 2005

Submitted to the Graduate Faculty of

Arts and Sciences in partial fulfillment

of the requirements for the degree of

Doctor of Philosophy

University of Pittsburgh

2011

UNIVERSITY OF PITTSBURGH

SCHOOL OF ARTS AND SCIENCES

This dissertation was presented

by

Amir Hussein Faraji

It was defended on

July 6, 2011

and approved by

Adrian C. Michael, Ph.D., Professor of Chemistry

Billy W. Day, Ph.D., Professor of Chemistry and Pharmaceutical Sciences

Ian F. Pollack, M.D., Walter E. Dandy Professor of Neurological Surgery

Stephen G. Weber, Ph.D., Professor of Chemistry and Clinical & Translational Science

CONVECTION-ENHANCED DELIVERY OF MACROMOLECULES TO THE BRAIN USING ELECTROKINETIC TRANSPORT

Amir Hussein Faraji, Ph.D.

University of Pittsburgh, 2011

Electrokinetic transport in brain tissue represents the movement of molecules due to an applied electric field and the interplay between the electrophoretic and electroosmotic velocities that are developed. This dissertation provides a framework for understanding electrokinetic transport and how it may be utilized for short-distance ejections, relevant to capillary iontophoresis, and long-distance infusions, for the clinical management of malignant brain tumors as a novel convection-enhanced drug delivery system.

In particular, electrokinetic transport was first analyzed in a series of poly(acrylamide-*co*-acrylic acid) hydrogels that demonstrated varying electroosmotic velocities. Moreover, a hydrogel was synthesized to mimic the electrokinetic properties of organotypic hippocampal slice cultures (OHSC), as a surrogate for brain tissue. Short- and long-distance capillary infusions of molecules into the hydrogels and OHSC provided a framework to understand the relevant phenomena, such as the effect of varying the capillary tip size, applied electrical current, ζ-potential of the capillary or the outside matrix, infusion time, tortuosity, and properties of the solute (including molecular weight and electrophoretic mobility). Control of the directional transport of molecules was also demonstrated over a distance of several hundred micrometers to millimeters. Finally, electrokinetic infusions were conducted *in vivo* in the adult rat brain, with results compared to those of pressure-driven infusions.

The experiments and results described in this dissertation provide a foundation for further development, by presenting a methodical means to increase the ejection profile and attain clinically relevant penetration distances while minimizing adverse effects to the brain tissue, including from the electric field itself. The rate of electrokinetic transport is greater than the rate of diffusion, and therefore it represents a novel form of convection-enhanced drug delivery system.

TABLE OF CONTENTS

LIST OF TABLES

LIST OF FIGURES

PREFACE

This doctoral dissertation describes the development of a convection-enhanced drug delivery system for eventual application to the treatment of malignant brain tumors. It is a project that I love immensely because of its potential to provide a therapeutic benefit to a patient population with limited options. This project also represents a first-step towards my future goal of translating basic science research into patient care.

I am appreciative to have such caring and invested clinical mentors in Neurosurgery – Johnathan Engh, L. Dade Lunsford, and Robert Friedlander – who provided the clinical framework for the management of malignant brain tumors, from which the topic of this dissertation was born. The support of my doctoral committee members, Professors Billy Day, Adrian Michael, and Ian Pollack is also strongly cherished. They have provided valuable guidance for my research and thoughtful mentorship over the course of my doctoral training.

I would like to express immeasurable gratitude to my research advisor, Professor Stephen Weber, whose support and unending patience has allowed me to advance my studies in Chemistry. In fact, he was one of the first individuals I met in Pittsburgh, as I first interviewed for the medical scientist training program, and has been an indispensible scientific and personal mentor since. He has helped foster my love of basic science and Chemistry, and challenged me to be creative, pursue my research passions, and ultimately perform rigorous science.

The Department of Chemistry staff, including Chuck Fleishaker, and Tom Gasmire

provided the technical support needed to complete this dissertation. I owe a special thanks to Michele Monaco for her advice through the years. I have made many wonderful friends in the department also, including Adam Hoye, John Maciejewski, Amy Rupert, Jonathan Cui, Alec Valenta, Yifat Guy, and Andrea Jaquins-Gerstl. In particular, Yifat Guy and Andrea Jaquins-Gerstl were brilliant collaborators on this project and helped bring my dreams to experimental fruition.

My belief in God has been my bastion, to see me through the difficulties and successes of my doctoral training. I have been blessed with great family and friends, and I appreciate their unbounded support over the years. Without their love, I would not have been able to reach this point. A special thanks to my father, Hamid Faraji, for teaching me to never forget my prayers, and to my mother, Pamela Faraji, for devoting her life to raising a beautiful family. My younger brother, Ali Faraji, is one of my best friends and has never missed an opportunity to teach me humility or lend encouragement. My family has taught me the importance of serving others. The goal of my research work, clinical practice, and life is to relieve human suffering, cure human diseases, and ultimately better humanity.

This dissertation is dedicated to the memory of my grandparents, who valued education and relayed strength through memories of their love....

1.0 ELECTROKINETIC AND DIFFUSIONAL TRANSPORT IN BRAIN TISSUE

1.1 ELECTRIC FIELDS IN BRAIN TISSUE

Brain tissue is a conductive and electrically active matrix, and it creates endogenous electric fields during neuronal communication. For instance, highly localized electric fields are developed in synapses laden with ion channel transport proteins.[1] Confined electric fields also occur where extracellular electrical potential fluctuations contribute to synchronous neuronal firing, such as with paracrine-type neurotransmitter release.[2] Furthermore, the laminar structure of the hippocampus has been shown to generate endogenous extracellular electric fields of tens of millivolts per millimeter by the synchronous activation of multiple neurons, with amplification due to the orientation of neurons.[3, 4] An extreme example of the electroactive nature of brain tissue is seizures. Often, a single epileptogenic focus may trigger a rapid cascade of neuronal depolarization and seizure activity.[5] These foci may be due to the presence of a tumor, blood vessel malformation, inflammation, or even fibrosis.[5]

Leão first described slowly propagating waves of transitory neuronal and glial depolarization – referred to as spreading depression – in 1944.[6] Spreading depression is characterized by the termination of all spontaneous or evoked synaptic activity and substantial K^+ efflux into the extracellular space, escalating to concentrations exceeding 40 to 50 mM (normal cerebrospinal fluid concentration is 5 to 6 mM).[7] This is exacerbated by cellular edema

and concomitant shrinkage of the extracellular space, as water enters the cells coupled to Na^+ influx. The elevated extracellular K^+ concentration is thought to depolarize neighboring cells, with a propagating wave progressing through contiguous gray matter at an average velocity of 3 mm/min, irrespective of functional or arterial territories.[8] Spreading depression is initiated when the regional extracellular K^+ concentration exceeds a threshold of 10 to 12 mM in a minimum critical volume (~1 mm^3 in rodents)[6] due to cerebral ischemia and trauma,[9-11] elevated concentrations of excitatory amino acids (such as glutamate interacting through *N*-methyl-*D*-aspartate (NMDA) receptors),[12, 13] and/or functional inhibition or genetic mutation of the Na^+/K^+-ATPase pump.[14-18] The K^+ depolarization threshold is determined genetically and believed to be lower in patients with a propensity for developing migraines, where spreading depression is understood to play a part in migraine auras and even as a trigger for headache development itself.[18] The example of spreading depression underscores the physiological uniqueness of the brain, and its propensity to develop endogenous electric fields.

1.2 ELECTROOSMOSIS AND ELECTROPHORESIS

In 1964, Ranck theorized that electroosmotic flow might be developed in the extracellular space of brain tissue solely due to endogenous synaptic firing.[19] As described by Ranck, "when electric current flows in a liquid which is surrounded by a substance with a surface charge, the liquid will move. This is the phenomenon of electroosmosis."[19] In other words, electroosmosis is the bulk fluid flow that is stimulated when an electric field is applied in a matrix with a non-zero ζ-potential.[20] The ζ-potential is the electrical potential that exists at the slip plane between mobile ions that are associated with a charged surface and the fixed surface charges.[20] In brain tissue and

other biological matrices, this ζ-potential is a result of cell membrane phospholipid head groups, proteins, carbohydrates, and other components of the extracellular matrix that are bound to the cell.[21] Ranck estimated the ζ-potential of brain tissue to be -15 mV,[19] which is now known to be a lower magnitude than the experimentally determined value and furthermore understated the extent of electroosmosis.[22]

Electrokinetic transport results from the application of an electric field across a porous matrix, such as brain tissue. This transport depends on key properties of the matrix and solute itself. Of note, two related modes of transport occur – electrophoresis and electroosmosis. Electrophoresis represents the movement of charged solute under the influence of an applied electric field, traditionally for separation and analysis. In contrast, electroosmosis is the bulk fluid flow that is stimulated when an electric field is applied in a matrix with a non-zero ζ-potential. In other words, electroosmosis is the movement of the solvent, while electrophoresis is the movement of the solute in relation to an applied electric field.

The cells and other components of the extracellular matrix create narrow channels through the extracellular space that display an inherent ζ-potential. The resistance to current flow is lower through these extracellular channels than through the cells themselves. Thus, it is through these channels that electroosmosis occurs. To understand the phenomenon simply, the channels through the biological extracellular space may be compared to a cylindrical tube with a ζ-potential at its walls, as exists within silica capillaries.[20] When an aqueous solution at physiological pH is in contact with the silica capillary, the silanol functional groups become ionized (with development of the ζ-potential). This results in counterion attraction to the capillary walls and development of an electrical "double layer," effectively leaving the bulk solution with a net charge.[20, 23] The passage of this charged solution through the capillary

represents both a portion of the electrical current and the concomitant transport of the bulk solution.[23] If the ζ-potential is negative, as with brain tissue and silica capillaries, the bulk fluid demonstrates an effective positive charge near the capillary walls. Therefore, the direction of electroosmosis is aligned with the path of positive current flow.

Many models exist to describe the electrical double layer formed at the boundary between the capillary wall and bulk solution. The earliest theoretical description of this phenomenon was devised by Helmholtz in 1879, in which he mathematically treated the double layer as a simple capacitor with ions adsorbed onto the surface.[24] Gouy and Chapman advanced this understanding with the development of a diffuse model, where the electrical potential at the surface decreases exponentially due to adsorbed counter ions from the solution.[25, 26] The classical electrical double layer is described by Stern model, as shown in Figure 1.1, which incorporates the Helmholtz and Gouy-Chapman models as two ion layers.[27] Convention holds that the fixed Helmholtz layer is termed the "Stern layer" or "compact layer" and the dispersed Gouy-Chapman layer is termed the "diffuse layer." Some important approximations used in the Stern model are that ions are considered as point charges, that only electrostatic interactions are significant, that a constant electrical permittivity exists throughout the double layer, and that the solvent molecule distribution is uniform. The thickness of the double layer depends on the ζ-potential magnitude and ionic strength of the solution, typically ranging from less than 1 to 10 nm in aqueous solutions.[20] At further distances from the capillary wall, the ion distribution in the bulk solution reaches electroneutrality.

Electroosmosis is related to the observed velocity, v_{obs}, of a solute under the influence of an electric field, E, by the Helmholtz-Smoluchowski equation, provided as Equation 1.1.

$$v_{obs} = v_{eo} = \frac{-\varepsilon\zeta}{\eta} E = \mu_{eo} E \qquad 1.1$$

Equation 1.1 demonstrates that v_{obs} is equivalent to the electroosmotic velocity, v_{eo}, for a neutrally charged solute. The velocity is related to the ζ-potential, ζ, where ε and η are the permittivity and viscosity of the medium, respectively. Moreover, the electroosmotic mobility, μ_{eo}, is directly related to the ζ-potential of the medium. Thus, for a given medium, v_{eo} of a solute is dependent on the ζ-potential of that medium and the applied electric field. However, if the ζ-potential cannot be altered, such as in brain tissue with physiological pH and ionic strength, v_{eo} is solely dependent on the applied electric field. For charged solutes, v_{obs} is not equal to v_{eo}. A new term – the electrophoretic velocity, v_{ep} – needs to be introduced. The surface charges on a particle define its ζ-potential analogous to the silica capillary, with a slip plane between closely adherent and diffusely associated counterions. Equation 1.2 relates this ζ-potential, $\zeta_{particle}$, to v_{ep}, where μ_{ep} is the electrophoretic mobility.

$$v_{ep} = \frac{\varepsilon\zeta_{particle}}{\eta} E = \mu_{ep} E \qquad 1.2$$

In this equation, the migration of a charged particle under an applied electric field, independent of the ζ-potential of the medium, is electrophoresis. Values of μ_{ep} can be determined for compounds by capillary electrophoresis. The observed velocity for charged compounds is the vector sum of two resultant velocity vectors (v_{ep} and v_{eo}), and the observed mobility is the sum of the two mobilities (μ_{ep} and μ_{eo}). Therefore, a molecule does not move when μ_{ep} is directly opposed and of equal magnitude to μ_{eo}.

Though the silica capillary provides a model for understanding electrokinetic transport, the brain extracellular space expresses some differences. This is because the channel through a capillary has a fixed diameter with a relatively smooth surface, whereby the charge density at the

capillary walls remains relatively constant. However, the channels through the brain extracellular space are highly variable and may contain sharp turns and bends which may create local variability in the electric field, double layer thickness, and resulting electroosmosis. On a more macroscopic scale (the scale of the experiments presented in this dissertation), the electrokinetic variability between each extracellular channel does not have an effect on the average direction of transport. On this macroscopic scale, the individual mobilities within each channel are averaged together with the resultant macroscopic velocity vector having a much larger magnitude than the microscopic variability between channels. Thus, while the degree of bending in the extracellular space may not impact the overall direction of the macroscopic velocity vector, it may decrease the magnitude of the macroscopic velocity vector. This is addressed in the next section, by introduction of the tortuosity.

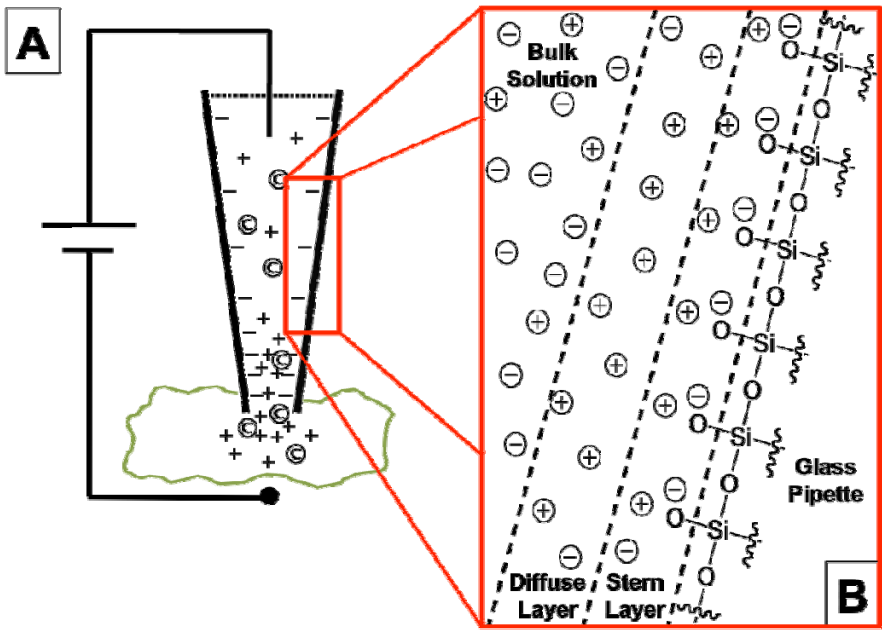

Figure 1.1. Electroosmosis in a silica capillary (**A**) and the electrical "double layer" (**B**).

1.3 TORTUOSITY AND HINDERED DIFFUSION

In the brain tissue, a compound must move throughout the tissue independent of an applied electric field. The tortuosity represents a quantification of the "twists and bends" within the extracellular space, as viewed from the perspective of a molecule.[28] The tortuosity was first described as the effective distance a solute must travel between two points in the extracellular space divided by the linear distance between those two points irrespective of any obstacles.[29] The distance a solute travels in a medium in the absence of any convective forces is related to the molecule's diffusion coefficient.

Diffusion is the net transport of a molecule along a chemical potential gradient by random molecular motion over small distances, as described initially by Fick.[30] The diffusion coefficient (D) of a molecule may be determined by the Stokes-Einstein equation, shown in Equation 1.3,

$$D = \frac{k_B T}{f} = \frac{k_B T}{6\pi\eta r} \qquad 1.3$$

where k_B is Boltzmann's constant, T is temperature, and f is the friction coefficient of the medium of interest. In particular, the friction coefficient is related to the viscosity of the medium, η, and the hydrodynamic radius, r, of the spherical particle.[31] From Fick's law of diffusion and the Stokes-Einstein equation, rates of diffusion depend on temperature, the viscosity of the medium, the magnitude of the chemical potential gradient, and the size (hydrodynamic radius) of the diffusing molecules. The rate of diffusion is slower when the friction coefficient is high, such as in a highly viscous medium, with large molecules, or at low temperatures; the converse holds for rapid diffusion. In contrast, convection represents another form of mass transport, which describes movement based on a physical or mechanical force, such as an applied pressure or

application of an electric field. Thus, the rate of transport due to convection is greater than the rate of transport due to diffusion. At a given point in time, convection results in a greater tissue distribution and transport than is achieved by diffusion alone. In contrast, the solute distribution in tissue achieved by convection and diffusion is limited by the size of the tissue itself, as the time scale approaches infinity.

In brain tissue, the extracellular space is not empty; rather, it is full of proteins, proteoglycans, and structural proteins such as collagen and elastin that surround large cells. Small molecules are able to more easily pass around these barriers when diffusing through the extracellular space as compared to larger, bulky molecules. This results in "hindered diffusion" for the larger molecules. Accordingly, a new definition for the tortuosity was related to a ratio of the diffusion coefficients for a molecule in free solution to a molecule in an obstructed medium (i.e.: the tissue of interest), as given by Equation 1.4 where λ is the tortuosity, D is the diffusion coefficient in free solution, and D^* is the apparent diffusion coefficient in the medium of interest.[28]

$$\lambda = \sqrt{\frac{D}{D^*}} \qquad 1.4$$

The tortuosity has been extensively studied in brain tissue by examining the diffusion of tetramethylammonium ion,[32-58] dextrans,[36, 59-62] other polymers,[63-65] albumin,[60] radiotracers,[66-69] neurotransmitters,[33] and other molecules.[44, 61, 70-75] Variability in the makeup of the extracellular space amongst tissue types and regions may occur, and thus tortuosity values may also vary.[33, 42, 43, 61]

The apparent diffusion coefficient in the medium, and thus the tortuosity, is influenced by the composition of the brain tissue extracellular space and the size and shape of the molecule. As

a result, this definition of tortuosity, developed by neuroscientists,[28] introduces an additional concept beyond a ratio of distances between two points – a frictional drag force – that acts to retard the progress of a diffusing molecule. The Stokes-Einstein equation accounts for the viscosity of the medium in determining the diffusion coefficient, and therefore introduction of this frictional drag force into the definition of tortuosity may be analogous to increasing the viscosity of the medium in the Stokes-Einstein equation. The frictional drag force may result from steric effects,[76] reptation[77] and entropic barrier transport[78] of flexible linear molecules, or due to changes in the extracellular space itself.

In 1958, Ogston introduced a model to describe the migration of a spherical molecule through a randomly-oriented interconnected matrix of immobile fibers by accounting for the steric effects introduced by that matrix on molecular transport,[76] which was later adapted to also describe the migration of nonspherical molecules.[79] In addition to this steric effect, reptation represents the "wormlike" movement of flexible linear molecules inside a matrix that is strongly cross-linked.[77] In a porous, heterogeneous matrix such as brain tissue, the extracellular space has different volumes (this is, the tissue has variable densities). With a larger extracellular space, a flexible linear molecule has an opportunity to become coiled and entangled.[77, 80] The degree of possible entanglement in a given matrix is related to the length of the macromolecule.[80] Thus, rather than simply moving through a heterogeneous matrix, flexible linear molecules may also fold upon themselves. Moreover, when the size of each entangled coil approximates the size of the voids within a matrix due to its heterogeneity, local entropic gradients become prominent and the molecule preferentially positions itself in the voids.[78, 81] Accordingly, these three processes may also be accounted for in the frictional drag force, especially for the large 70 kDa fluorescent dextran conjugates utilized in this dissertation.

Furthermore, this frictional drag force may be introduced as a result of changes in the diameter of the channels through a matrix, such as with the extracellular space *in vivo*. In the case of brain tissue, the diameter of the channels through the cortical extracellular matrix *in vivo* was determined to be 38 to 64 nm under homeostatic conditions, but only 10 nm after cardiac arrest.[61] Thus, a nanoparticle or macromolecule with globular size greater than 10 nm would not physically fit through the cortical extracellular matrix channels in ischemic tissue. This result for cardiac arrest is interesting and perhaps a product of vasoconstriction within the peripheral vasculature with a resultantly greater volume of blood within the internal organs, including the brain, due to activation of the sympathetic nervous system. The volumetric distribution of intracranial components is described by the Monro-Kellie hypothesis,[82-84] whereby the total intracranial volume is fixed and is a sum of the volumes of brain tissue (~80% of the total volume), cerebrospinal fluid (~10% of the total volume), and blood (~10% of the total volume). Thus, if the intracranial volume of blood increases, then the volumes of brain tissue and cerebrospinal fluid must correspondingly decrease by the same amount. Because the *in vivo* brain tissue is slightly compressed and the volume of cerebrospinal fluid decreases due to this increase in blood supply, the extracellular channels decrease in diameter. The frictional drag force for transport in this situation may correspondingly increase.

Moreover, the brain demonstrates significant anisotropy resulting from regional tissue architecture. The gray matter is composed of primarily neuronal cell bodies and glial cells, and the effective diffusivity in gray matter is isotropic.[85] In contrast, the white matter contains bundles of axons that project from those cell bodies and show directional orientation. Consequently, the effective diffusivity in white matter is anisotropic.[86-88] This principle governs fiber tracking in diffusion tensor imaging magnetic resonance imaging.[86-88] For the purposes of

transporting molecules through the white matter of the brain, the frictional drag force depends on the orientation of transport to the axonal bundles. Therefore, transport aligned with the bundle projections produces a smaller frictional drag force compared to transport perpendicular to the plane of the bundles.

Finally, the frictional drag force also accounts for the biochemical interactions of a molecule with the brain tissue milieu. In particular, if a drug is to be transported, the effects of decomposition by enzymatic processes, clearance due to vascular or cellular uptake, and immobilization and binding to receptors must all be considered.[85] As one example of this phenomenon, consider the diffusional transport of a molecule that undergoes reversible binding to a cell surface receptor. The observed diffusion coefficient can therefore be estimated by a weighted-average of the proportion of time the molecule spends between the bound and unbound states. By extension, the frictional drag force is higher when the molecule remains bound to the receptor for a longer time. Finally, the rate of fluid clearance from the given volume of brain tissue *in vivo* (such as for fluid introduced by an infusion) ranges from approximately 0.3 to 0.5 $\mu L\ min^{-1}\ mL^{-1}$.[89]

Therefore, the frictional drag force included in D^* includes processes such as steric effects, reptation, entropic barrier transport, variations in extracellular matrix channel diameter, tissue anisotropy due to architectural regions, and biochemical interactions. This drag force may also exist during molecular transport by convection, since it represents the effect of the tissue itself on a particular molecule's motion. For subsequent discussions in this dissertation, the tortuosity is defined by Equation 1.4, which includes the frictional drag force.

1.4 MEASUREMENT OF THE ZETA-POTENTIAL AND TORTUOSITY

These fundamental phenomena – electrophoresis, electroosmosis, and tortuosity – are essential to understand when electrokinetically transporting a molecule through the brain extracellular space. As mentioned previously, Ranck estimated the ζ-potential of brain tissue to be -15 mV to further determine whether electroosmosis existed within and adjacent to synapses.[19] To more accurately understand electroosmosis in brain tissue, its ζ-potential must be experimentally quantified. Moreover, for macroscopic bulk transport of molecules through the extracellular space, the tortuosity must also be quantified. Our lab previously developed a methodology for measurement of the ζ-potential and tortuosity in brain tissue using organotypic hippocampal slice cultures (OHSC) as an *in vitro* surrogate for brain tissue.[21, 22]

1.4.1 Organotypic Hippocampal Slice Cultures

The hippocampus lies deep in the brain, and comprises the medial aspects of the temporal lobes in humans. It is part of the limbic system of the brain and plays an essential role in learning, spatial navigation, and long-term memory.[90] Furthermore, the hippocampus is susceptible to damage in Alzheimer's disease, epilepsy, traumatic brain injury, and ischemia.[90] OHSC are used in neuroelectrophysiology and neuropharmacology as a model surrogate for brain tissue,[91] as they are relatively easy to obtain and culture with a preserved tissue architecture comprised of neurons and glial cells.

The OHSC preserves the laminar structure of the hippocampus with intact circuitry, as shown in Figure 1.2. The cornu ammonus (CA) is composed of pyramidal neurons and is divided into four subregions: CA1, CA2, CA3, and CA4. The most prominent regions are the CA1 and

CA3, and often only these two regions are appreciated upon microscopic inspection of hippocampal morphology. In contrast, the dentate gyrus (DG) is composed of granule neurons. Hippocampal granule neurons are tiny, typically less than 10 μm in size. Moreover, hippocampal granule neurons undergo adult neurogenesis, while cortical and cerebellar populations of granule neurons do not.[90] The entorhinal cortex (EC) receives input from other cortical areas and project axons primarily to the dentate gyrus and CA3. The subiculum (Sb) is also composed of pyramidal neurons and lies between CA1 and the entorhinal cortex in humans. It receives axonal input from CA1 and is the main output of the hippocampus with axons projecting to the nucleus accumbens, septal nuclei, prefrontal cortex, lateral hypothalamus, nucleus reuniens, mammillary nuclei, deep entorhinal cortex, and amygdala. Interspersed between these two neuron types are interneurons, which perform regulatory functions through the inhibition and modulation of neuronal firing.

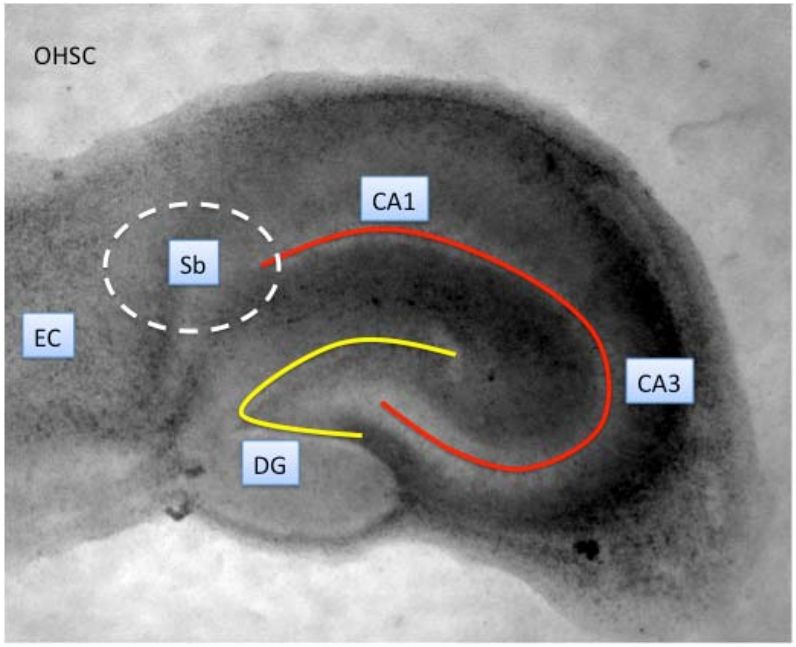

Figure 1.2. Bright field image of an OHSC and its architecture. The CA1, CA3, dentate gyrus (DG), subiculum (Sb), and entorhinal cortex (EC) are shown.

Our protocol for the preparation of OHSC follows the Stoppini method,[92] whereby thin acute hippocampal slices are placed on a porous hydrophilic insert membrane above a medium containing culture nutrients. The nutrients from the medium pass through the membrane into the OHSC, while gas exchange occurs from above. In our laboratory, the acute hippocampal slices are typically obtained from postnatal rats with ages ranging from 7 to 9 day old pups. The insert membrane is composed of modified polytetrafluoroethylene (PTFE) and is commercially available (Biopore™ Millicell Organotypic Insert, Millipore, Billerica, MA). The initial thickness of the acute hippocampal slice is essential to prolonged viability of the OHSC, as the innermost cells of slices thicker than 500 μm may be susceptible to hypoxia or other forms of nutrient deprivation. As a result, the acute hippocampal slices used in this dissertation typically have initial thicknesses ranging from 300 to 500 μm to allow for adequate nutrient and gas exchange throughout, and are approximately 150 to 200 μm thick after 2 to 4 days of culture.[93] After culturing for roughly two days, equilibration is achieved and the OHSC demonstrates synaptic rearrangement with general preservation of the *in vivo* circuitry.

1.4.2 Determination of the ζ-Potential and Tortuosity

Our laboratory has previously published a methodology to characterize the ζ-potential and tortuosity of OHSC.[21, 22] This determination was made by observing the mobilities of fluorescent dyes in OHSC while an electric field is applied across the tissue. A molecule may be transported by electroosmosis, electrophoresis, or both in brain tissue upon application of an electric field with an observed velocity and mobility (v_{obs} and μ_{obs} respectively). The observed mobility μ_{obs} for a single compound in a medium was provided by Equation 1.5, which includes μ_{ep}, μ_{eo}, and λ. In this expression, the tortuosity-corrected sum of μ_{ep} and μ_{eo} provided the μ_{obs}.

$$\mu_{obs} = \frac{v_{obs}}{E} = \left(\frac{1}{\lambda^2}\right)\left(\mu_{ep} + \mu_{eo}\right) = \left(\frac{1}{\lambda^2}\right)\left(\mu_{ep} - \frac{\varepsilon\zeta}{\eta}\right) \quad 1.5$$

In a "two-probe" experiment, two electrophoretically and spectroscopically different fluorescent probes (1 and 2) were injected into a medium and μ_{obs} for each dye was measured under an applied electric field ranging from 3.2 to 20 V/cm.[22] The observed mobilities were measured simultaneously during a single run and related to arrive at a value for the ζ-potential (Equation 1.6) and λ (Equation 1.7) for the medium where the numerical subscripts referred to each of the two probes.

$$\zeta = \frac{\mu_{obs1}\dfrac{\left(\mu_{ep1} - \mu_{ep2}\right)}{\left(\mu_{obs1} - \mu_{obs2}\right)} - \mu_{ep1}}{\left(\dfrac{-\varepsilon}{\eta}\right)} \quad 1.6$$

$$\lambda = \sqrt{\frac{\mu_{ep1} - \mu_{ep2}}{\mu_{obs1} - \mu_{obs2}}} \quad 1.7$$

The individual ζ-potential and tortuosity values were averaged to arrive at a value for the OHSC. The hippocampus is grouped into heterogeneous regions with variable populations of cells. However, there was no significant difference for the values of tortuosity between the CA1, CA3, and DG regions by one-way ANOVA (p = 0.1) in the OHSC.[22] The average OHSC ζ-potential was determined to be -22.8 ± 0.8 mV and the average tortuosity was 2.24 ± 0.10 for 70,000 MW fluorescent dextran conjugates (data presented as mean ± standard error of the mean).[22] In comparison, the tortuosity of 70,000 MW dextran conjugates in the acute rat cortical slice was 2.25 ± 0.09[59] and the cortex *in vivo* was 2.68 ± 0.11.[61]

The tortuosity difference between acute slices or OHSC and *in vivo* conditions may be not only be due to the physical dispersal of OHSC cells, but also reduced osmoregulation of the

extracellular space *ex vivo*, an increase in the extracellular fluid fraction, and tissue swelling that reduces the tortuosity. The fluid content of the extracellular space is determined by an oncotic pressure gradient *in vivo*, due to a difference in protein concentrations between the blood and extracellular space, as described by Starling in 1896.[94, 95] In his original treatises, the net fluid movement between compartments, J, was related to the difference between the capillary and interstitial hydrostatic pressures – P_c and P_i respectively – and the vascular capillary and interstitial oncotic pressures – π_c and π_i respectively,[94, 95] as shown by Equation 1.8. Two additional factors also enter into the equation: the filtration coefficient, K_f, and the reflection coefficient, σ.

$$J = K_f\left[\left(P_c - P_i\right) - \sigma\left(\pi_c - \pi_i\right)\right] \qquad 1.8$$

The filtration coefficient describes the inherent permeability of the vascular capillary to water, and is a product of the capillary surface area and its permeability to water. Capillary permeability, and hence the filtration coefficient, varies depending on tissue type and non-homeostatic conditions; for example, the capillaries of the kidney glomerulus have high filtration coefficients.[96] Moreover, histamine release results in alteration of capillary bed homeostasis and an increase in the filtration coefficient, which results in tissue swelling.[97] The reflection coefficient accounts for changes in capillary permeability to plasma proteins.[98] If a capillary bed is permeable to proteins, such as albumin, the reflection coefficient is between zero and one. If the capillary bed has a reflection coefficient close to one, as with the kidney glomerulus, it is relatively impermeable to proteins.[96] The human brain demonstrates a very low filtration coefficient of 10.4×10^{-4} cm/s and is very similar to transport by diffusion.[99] Moreover, the brain capillary reflection coefficient also approaches one for proteins, as a result of tight junctions between endothelial cells.[98] Therefore, the brain is relatively impermeable to fluid transport from

capillary beds, and as such the fluid content in the extracellular space is tightly regulated *in vivo*. Because this mechanism of osmoregulation is nonexistent in OHSC, the extracellular space is allowed to swell and its resulting tortuosity may be decreased from its homeostatic state *in vivo*.

1.5 ELECTROOSMOTIC SAMPLING OF THE BRAIN EXTRACELLULAR SPACE

With precise quantification of the ζ-potential and tortuosity, our lab has been able to transport molecules in the extracellular space of OHSC using electroosmosis. In particular, this work has focused on the minimally invasive uptake of nanoliter volumes of extracellular fluid for the sampling and determination of peptide concentrations and ectopeptidase activity with high spatial resolution in the OHSC.[100]

In these initial sampling experiments,[100] the OHSC and its insert membrane were placed in an optically transparent dish with an artificial cerebrospinal fluid solution containing the peptide of interest underneath. A 150 μm inner diameter fused silica capillary was inserted into the CA3 region of the OHSC with its distal end immersed in a second dish with the artificial cerebrospinal fluid solution; the capillary was filled with the same solution to make electrical contact between the two dishes. A platinum electrode was placed in each dish. When an electric field was applied across the two electrodes, electroosmosis the fluid beneath the OHSC insert membrane was conveyed into the OHSC where an ectopeptidase acts on its peptide substrate, with further conveyance of this extracellular fluid into the sampling capillary and towards the second dish. Diluted samples were obtained and passed through a capillary HPLC with electrochemical detection of the relevant peptides. The sampling process required only a few minutes with electric fields ranging from 30 to 60 V/cm at the capillary tip. The electric fields at

the capillary tip utilized in electroosmotic sampling were significantly larger than the fields used across the OHSC in the determination of the ζ-potential and tortuosity values by the two-probe method. This naturally begs the question: does this methodology damage, or even kill, cells in the OHSC?

In a second follow-up paper from our group, Hamsher *et al*. demonstrated the electroosmotic sampling conditions necessary to minimize damage to the OHSC.[101] To assess OHSC viability, propidium iodide was co-incubated with the tissues for up to one day before electroosmotic sampling. Propidium iodide is a salt that is soluble in physiological buffer solutions, such as artificial cerebrospinal fluid. Because of its charge, it is unable to appreciably pass through the cell membranes by diffusion. However, when a cell is damaged, propidium intercalates DNA and forms a strongly fluorescent complex. Thus, propidium iodide is an indirect marker of cell death. As described in this paper, "safe" sampling conditions were taken as less than 10% of the fluorescence of a positive methanol-stained control after correction for the negative control.[101]

A wide array of experimental parameters was evaluated, including the region of the OHSC sampled from, the depth of capillary insertion into the OHSC (or distance of the capillary tip away from the tissue surface itself), the inner diameter of the capillary, and the applied voltage. For electroosmotic sampling with lower than 1,300 V, the average propidium fluorescence (± standard error of the mean) increased only 1.0 ± 0.3 % and there was no difference between the CA1 and CA3 regions ($p > 0.08$).[101] At conditions greater than 1,400 V, CA1 was more vulnerable than CA3 ($p < 0.007$).[101] The observed fluorescence increases, and by extension tissue damage, were seen at the sampling site and not at remote areas of the OHSC. Capillaries of 150 μm inner diameter resulted in less tissue damage (≤ 10% propidium

fluorescence increase) across all tested voltages (≤ 2,000 V), while larger 280 μm inner diameter capillaries demonstrated an approximately 20 to 25 % propidium fluorescence intensity increase at more than 900 V.[101] As a general rule, when the power dissipated in the OHSC was less than 120 μW, the cell death was less than 10% of the positive control as measured by propidium fluorescence. To calculate the power dissipated, the resistance of OHSC was estimated as 40% of the resistance of the electrolyte buffer solution, as the extracellular volume fraction in OHSC was approximated as 40%.[101]

In summary, these two papers described the methodology for electroosmotic sampling and parameters whereby it could be applied to OHSC with minimal damage.[100, 101] Our lab has demonstrated the utility of electroosmotic uptake of peptides for analysis. However, the focus of this dissertation utilizes electroosmosis to deliver compounds over short distances, with relevant discussion to capillary iontophoresis, and longer distances, as applied to the clinical treatment of malignant brain tumors and convection-enhanced delivery.

2.0 SYNTHESIS AND CHARACTERIZATION OF A GEL MODEL WITH THE ELECTROKINETIC PROPERTIES OF ORGANOTYPIC HIPPOCAMPAL SLICE CULTURES

2.1 INTRODUCTION

When an electric field is applied across an electrolyte-filled, porous matrix electrophoresis and electroosmosis occur. This electrokinetic transport depends on key properties of the matrix and solutes. Electrophoresis is the movement of a charged solute under the influence of an applied electric field, traditionally used for separation and analysis. In contrast, electroosmosis is the bulk fluid flow that is stimulated when an electric field is applied to an electrolyte solution in a porous matrix with a non-zero ζ-potential. In other words, electroosmosis is the movement of the solvent, while electrophoresis is the movement of the solute in an applied electric field. The electroosmotic velocity is proportional to the ζ-potential that exists at the boundary between the fluid in the porous space and the stationary walls that contain the fluid. For example, fixed charges on cell-surface functional groups and membrane-bound constituents of the extracellular matrix create a ζ-potential.[21] The electroosmotic velocity of a neutral solute molecule – the direction and distance traveled under an applied electric field in a given time – in a particular medium is thus governed by the ζ-potential of that medium, and the direction and magnitude of the electric field. This relationship is described by the Helmholtz-Smoluchowski equation as

shown in Equation 2.1, where v_{eo} is the electroosmotic velocity, η is the viscosity of the medium, ε is the permittivity of the fluid, ζ is the ζ-potential, μ_{eo} is the electroosmotic mobility, and E is the applied electric field.

$$v_{obs} = v_{eo} = \frac{-\varepsilon\zeta}{\eta} E = \mu_{eo} E \qquad 2.1$$

Poly(acrylamide)-based hydrogels applied to separations were first developed over fifty years ago, and their utility was explored for separation of proteins, DNA, and other macromolecules.[102-105] One reason for the wide acceptance of poly(acrylamide) over other matrices used for electrophoresis is the lack of significant electroosmotic flow, and thus a ζ-potential. Interestingly and in contrast, there has been considerable work in recent years for the development of separations matrices that provide electroomosis to separate both neutral and charged molecules.[106-111] For example, Fujimoto *et al*. introduced negatively charged sulfonate moieties into an acrylamide-based hydrogel to increase separation of neutral molecules under physiological pH.[110] Anionic gellan gels can be crosslinked by Ca^{2+}, but the resulting gel is not neutral. The additive poly(ethylene oxide) reduces electroosmotic flow in these gellan gels to aid with electrophoretic separation.[108] Negatively charged polyacrylamide-based matrices have also been synthetically prepared for capillary electrochromatography.[110, 112] Acrylates have also been used as the organic component in organic-silica hybrid monolithic capillary columns.[111-113] Multilayered polyelectrolytes incorporating acrylic acid have been developed for control of electroosmotic flow in capillaries and microfluidic channels. By suitable control of the surface modification chemistry, a range of electroosmotic mobilities can be obtained at pH 7.4 (or other values).[114] Thus, the development and fine control over electroosmotic flow in polymeric gels,

and in channels with walls of multilayered polyelectrolytes, have been of long-standing interest and practical importance.

Diffusion also plays a role in molecular transport. It is related to the rate of net transport of a molecule along a chemical potential gradient. Rates of diffusion depend on temperature, the viscosity of the medium, the magnitude of the chemical potential gradient, and the size of the moving molecules. In a medium such as a hydrogel or tissue in which there are obstructions, the diffusion rate is lower than it would be in an unobstructed medium. The presence of obstructions gives rise to tortuosity. The tortuosity of a medium can be determined as a ratio of the diffusion coefficients for a molecule in free solution to a molecule in the tortuous medium (i.e.: the matrix of interest), as given by Equation 2.2 where λ is the tortuosity, D is the diffusion coefficient in free solution, and D^* is the diffusion coefficient in the medium of interest.[59]

$$\lambda = \sqrt{\frac{D}{D^*}} \qquad 2.2$$

The diffusion coefficient in the medium, and thus the tortuosity, depends upon the three-dimensional structure of the hydrogel matrix, the solute size and shape, and any frictional or viscous drag forces the solute experiences in the matrix.[31]

Translational motion of molecules in the extracellular space of biological tissues is typically viewed as occurring by diffusion and tortuosity.[28] Electroosmotic flow represents an additional transport mechanism that occurs in tissues due to natural processes, such as neuronal depolarization[1, 19] or due to applied electric fields.[23, 115-120] We have previously measured the ζ-potential and tortuosity of organotypic hippocampal slice cultures (OHSC) as a representative for living brain tissue. The ζ-potential of OHSC is -22.8 ± 0.8 mV and the tortuosity is 2.24 ± 0.10.[22] The ζ-potential of skin pores is also important, as electroosmosis is a fundamental component of

transdermal iontophoresis.[121] While electroosmotic transport in skin has been investigated for many years, the understanding that the ζ-potential in brain is significant is recent. We have demonstrated the application of electroosmosis in OHSC for drawing peptides through the OHSC, followed by analysis of the captured sample to infer peptidase activity in the extracellular space.[100] However, in this work, or any related attempt to use electroosmosis in brain, it is necessary to assess the degree to which electroosmosis contributes to solute transport. Unfortunately, it is impossible to control the ζ-potential in the extracellular space of a living tissue, as the ζ-potential is intrinsically tied to the physical composition of the tissue.

As such, we developed poly(acrylamide-*co*-acrylic acid) hydrogels with a range of ζ-potentials and tortuosities. At physiological pH, the acrylic acid exists as the negatively charged acrylate species. These fixed anions create a ζ-potential in the gel polymer matrix. Three hydrogels were prepared with 0, 10, and 25% (w/w) acrylic acid. These three types of hydrogel had distinctly different ζ-potentials and degrees of electroosmosis, with the highest acrylate content hydrogel demonstrating a ζ-potential comparable to the OHSC. This work describes the synthetic preparation of the three hydrogel compositions, as well as the determination of their ζ-potentials and tortuosities. The result is a set of gels with well-known ζ-potentials and tortuosities.

2.2 EXPERIMENTAL

2.2.1 Chemicals

All reagents used to make the poly(acrylamide-*co*-acrylic acid) hydrogels were purchased

from Aldrich (St. Louis, MO) and were used without additional purification. Fluorescent dyes – Texas Red dextran conjugate 70 kDa (**TR70**), fluorescein dextran conjugate 70 kDa (**FL70**), and Texas Red dextran conjugate 3kDa (**TR3**) – were purchased from Invitrogen/Molecular Probes (Eugene, OR).

2.2.2 Standard Solution Preparations

A glucose-free HEPES-buffered salt solution (GF-HBSS) containing (mM): 143.4 NaCl, 5 HEPES, 5.4 KCl, 1.2 $MgSO_4$, 1.2 NaH_2PO_4, and 2.0 $CaCl_2$. GF-HBSS was prepared with 18 MΩ purified water from a Millipore Synthesis A10 system (Millipore, Billerica, MA), filtered, adjusted to pH 7.40, and refrigerated at 2.6 °C. It was warmed to 37 °C before use. **TR70** and **FL70** were dissolved in GF-HBSS to make 0.34 mM and 0.67 mM solutions, respectively, then filtered with 13 mm, 0.45 μm nylon filter units or equivalents (Millipore) and frozen until use. Before use, dextran conjugates were modestly diluted with GF-HBSS to final concentrations of 0.19 mM for **TR70**, 0.29 mM for **FL70,** and 0.40 mM for **TR3**.

2.2.3 Synthesis of Hydrogels

Poly(acrylamide-co-acrylic acid) hydrogels were prepared by a thermally-initiated radical polymerization reaction. The total weight of reagents was kept constant (279 mg/5 mL) while the component w/w ratios of acrylic acid and acrylamide were varied, as described in Table 2.1. The gels had an acrylic acid percentage of 25%, 10%, and 0% (weight of acrylic acid/weight of all monomer species). The bisacrylamide cross-linker was maintained at a fixed weight percentage of approximately 1.4%. Early efforts to weigh this small amount of cross-linker with a standard

electronic balance (Mettler-Toledo, Columbus, OH, Model AG245; readability 0.1 mg) resulted in somewhat variable gel parameters, In later experiments, the cross-linker was more accurately weighed (Mettler-Toledo, Columbus, OH, Model XS105DU; readability 0.01 mg) with variability less than 0.1 mg. This is described further in the results and discussion section.

Table 2.1. Table of reagents for each synthetic gel type.

	25% Acrylic Acid		**10% Acrylic Acid**		**0% Acrylic Acid**	
	weight (mg)	**mmol**	**weight (mg)**	**mmol**	**weight (mg)**	**mmol**
Acrylamide	206.0	2.90	247.5	3.48	275.0	3.87
Acrylic Acid	69.0	0.96	27.5	0.38	0.0	0.00
Bisacrylamide	4.0	0.03	4.0	0.03	4.0	0.03

The reagents were weighed and dissolved in 4.5 mL of ultrapure water (Cayman Chemical, Ann Arbor, MI) each and stirred vigorously for 5 minutes. The solutions were then titrated to a pH range of 7 to 8 using an aqueous 1 M NaOH solution. The final solution volumes were brought to 5.0 mL with ultrapure water. The three solutions were then deaerated with nitrogen for 20 minutes at room temperature. Immediately after deaerating, 5.0 mg of ammonium persulfate (0.02 mmol) and 5.2 μL of tetramethylethylenediamine (TEMED, 0.03 mmol) were quickly added to each solution, which was vigorously stirred for another 3 minutes at room temperature. Each clear solution was poured in a 50 mm x 16 mm Pyrex glass dishes and placed inside an oven at 100 ± 5 °C for 2 hours. The Pyrex dishes were removed from the oven and allowed to cool for 10 minutes at room temperature. The clear, colorless gels were separated from the Pyrex dish walls and slowly peeled from the dish. Each gel was individually placed in a covered plastic dish filled with approximately 25 mL GF-HBSS solution and shaken lightly at 10 °C overnight. The buffer solution was exchanged the following day with 25 mL of fresh GF-HBSS, placed back in the shaker at 10 °C for another 24 hours. Finally, the GF-HBSS was

exchanged once more (25 mL), and the gels were placed in the refrigerator where they were allowed to complete the equilibration. A final pH check was performed to assure the gels were pH 7.40 with full immersion of the probe into the gel before further characterization

2.2.4 Characterization of the ζ-Potential and Tortuosity

The experimental apparatus was used without modification from our previously reported setup.[22] A four-electrode potentiostat coupled with a differential amplifier and reference Luggin capillary electrodes was used to provide feedback control of the electric field in the gel. GF-HBSS was used as the electrolyte solution in the reservoirs. Imaging of the experiment was done with an Olympus IX-71 inverted fluorescence microscope with an Olympus UPlan Apo 4× objective lens (Melville, NY), and a charge-coupled device camera (ORCA-285 Hamamatsu, Hamamatsu City, Japan). A DA/Fl/TA-3X-A triple-band "Pinkel" filter set (Semrock, Rochester, NY), with exciter 1 at 387 nm, exciter 2 at 494 nm, exciter 3 at 575 nm, triple-band dichroic mirror: 394-414 nm, 484-504 nm, 566-586 nm, emitter: 457, 530, 628 nm were used according to the fluorescent properties of the molecules. SimplePCI 6.0 software (Compix, Cranberry, PA) was used for image acquisition and processing.

Prior to the start of the ζ-potential measurements, the gel was injected with each fluorophore solution separately to set exposure times for each fluorophore. A fresh piece of gel was cut to size and placed in the apparatus channel over the objective lens. Using a P-2000 capillary puller from Sutter (Novato, CA), a 150 μm inner diameter (ID) fused silica capillary was pulled to a tip opening of approximately 12 μm to create an injection capillary. The injection capillary was filled with the **TR70**/**FL70** or **TR3** fluorophore solution and lowered perpendicularly into the gel using a MP-285 micromanipulator (Sutter, Novato, CA) to a depth of

half the gel's thickness. The distal end of the injection capillary was connected to the FemtoJet® express (Hamburg, Germany), pressurized via a compression nitrogen tank from Valley Natural Gas (Wheeling, WV). The FemtoJet® express was set to deliver an injection pressure of 200 to 250 hPa for 0.2 to 0.5 seconds, with a compensation pressure of 0 to 20 hPa. The exact parameters were varied within these ranges so that the volume of ejected fluorophore was appropriate for the sensitivity and dynamic range of the CCD camera. Once the injection was complete, the injection capillary was raised from the OHSC and moved aside. The Luggin capillaries were lowered to a depth of half the gel's thickness on either side of the injection spot. This process was completed an average of two times per gel piece, and all experiments were conducted at ambient temperature (24 to 26 °C).

An electric field between 60 and 250 V/m was applied to each gel. One image was acquired every second. The electric field was monitored at the two Luggin capillaries and at the platinum electrodes in the reservoirs by two multimeters to ensure accurate control of the electric field. Movement of a fluorophore towards the cathode was defined as positive movement. The velocities of the **TR70** and **FL70** fluorophores were measured post-analysis using Simple PCI. Specifically, the velocity was measured as the distance that the fluorophore moves over a period of time. The locations of the fluorophores were defined by their maximum peak intensities at time zero and at one other time during the experimental run. Typically, 6 to 9 timepoints (30 to 60 seconds apart) were analyzed per run to arrive at an average velocity. The ζ-potential and tortuosity for each gel were extracted with this analysis, as previously described.[22]

2.2.5 Measurement of Solute Diffusion Coefficients in the Hydrogels

Prior to the start of the diffusion measurements, a characterized 25% and 0% acrylic acid

gel were independently injected with a **TR70** or **TR3** fluorophore solution to set each exposure time. The fused silica injection capillaries used were the same as previously described. The injection capillary was filled with the fluorophore solution and lowered perpendicularly into the gel using a micromanipulator to a depth of half the gel's thickness. The injection capillary was connected to the FemtoJet® express set to deliver an injection with the same parameters as described previously. Following ejection, the injection capillary was immediately withdrawn by the micromanipulator and moved aside. After each ejection, an image was taken every 2 to 5 seconds for a total duration of 3 to 6 minutes to record the diffusion of the fluorophore. All experiments were conducted at ambient temperature (24 to 26 °C). This was repeated for each gel and fluorophore type. Imaging of the experiment was done with the fluorescence microscope as described earlier, and SimplePCI 6.0 software was used for image acquisition and processing.

Following acquisition, the images at 10 second time intervals were exported as an (*x,y*)-matrix of fluorescence intensities. These data matrices were imported into OriginPro 8.1 software (OriginLab, Northampton, MA). A three-dimensional Gaussian surface was fit to the data set in order to find the peak. The image was then cropped three standard deviations from the peak's center in the *x*- and *y*-directions. With this reduced data set, a second Gaussian fit was performed yielding the standard deviations of the Gaussian fit in both the *x*- and *y*-directions. The standard deviations in the *x*- and *y*-directions were very similar and consistent with the Gaussian fit. The variance was obtained by squaring the average of the two standard deviations. The variance was plotted against time and a linear regression was performed. If a line fit had an R^2 value less than 0.95, it was not included in the final average. As with work by Nicholson *et al.*, dividing the slope of this line by four afforded the diffusion coefficient.[59] Averaging the diffusion coefficients from each run (typically 3 to 6 runs per gel) allowed determination of a

final diffusion coefficient with standard error.

2.2.6 Free Diffusion Coefficients of Dextran Conjugates

Free diffusion coefficients were determined as described by Beisler *et al*.[122] GF-HBSS mobile phase pumped through the system using a Pico Plus syringe pump (Harvard Apparatus, Holliston, MA). The sample solutions were injected using an HP 1050 autosampler (Hewlett-Packard, Palo Alto, CA) into a 1.0 μL loop in a VICI 6-port Cheminert Injector (Houston, TX). An ISCO 3850 Capillary Electropherograph UV detecctor (Teledyne ISCO, Lincoln, NE) was used for detection (215 nm) of the fluorophores. Signals were collected by Peaksimple 3.29 software (SRI Inc., Torrance, CA) for analysis. The data were imported into OriginPro for differentiation, followed by the determination of the first and second central moments using PeakFit 4.0 software (Systac Software Inc., San Jose, CA). Diffusion coefficients were calculated from the slopes of second moment versus first moment linear plots. In addition, errors for the diffusion coefficients were calculated based on the error of the slope, assuming negligible error in the flow rate, capillary length, and capillary diameter.

2.2.7 Characterization of the Hydrogel Water Content

The water content of each gel was determined by dehydration weighing. A 10 mm by 10 mm piece of gel was cut and placed inside of a pre-weighed 1.8 mL ROBO autosampler vial (VWR, West Chester, PA). The aggregate weights were recorded for each vial, and they were placed in an oven at 110 °C overnight. The vials were removed from the oven and reweighed. The water content, by weight, was determined by subtracting the post-dehydration weight from

the pre-dehydration weight, controlling for the autosampler vial weight and residual salt content within the GF-HBSS buffer. Six runs were completed for each gel type, with the final water content data provided as an average with standard error.

2.2.8 Statistics

All data are presented as mean ± standard error of the mean (SEM), where *N* represents the number of experimental runs. Comparisons among groups were made by one-way analysis of variance (ANOVA) with $p < 0.05$ considered as significant.

2.3 RESULTS AND DISCUSSION

As demonstrated in Figure 2.1, while under a constant electric field, in the 0% acrylic acid gel composition there was significant movement of the anionic **FL70** dextran conjugate (electrophoretic mobility -8.80 ± 0.2 $\times 10^{-9}$ m^2/Vs, $N = 3$)[21] towards the cathode and negligible movement of the weakly cationic **TR70** dextran conjugate (electrophoretic mobility 0.46 ± 0.03 $\times 10^{-9}$ m^2/Vs, $N = 3$, slightly different from published value due to commercial batch),[21] The 10% acrylic acid gel composition showed movement of the **TR70** dextran conjugate towards the anode and negligible movement of the **FL70** dextran conjugate, while the 25% acrylic acid gel composition showed movement of both the **FL70** and **TR70** dextran conjugates towards the anode. These results indicate qualitatively that as the percentage of acrylic acid increases, the ζ-potential becomes more negative, and there is an increasing contribution of electroosmosis to the observed field-induced velocity.

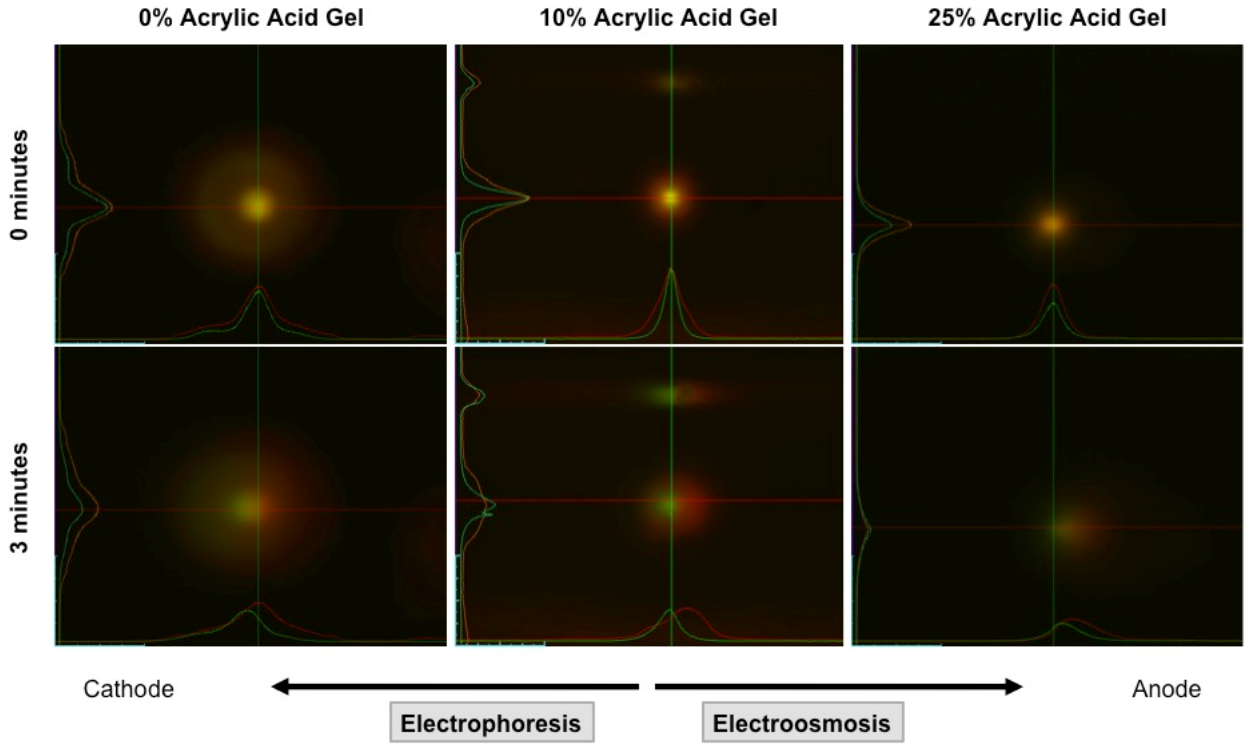

Figure 2.1. Electrokinetic transport in the three hydrogels. **TR70** (red) and **FL70** (green) dextran conjugates move differently under a uniformly applied electric field in the poly(acrylamide-co-acrylic acid) gels prepared at 0%, 10%, and 25% w/w acrylic acid.

The magnitudes of the ζ-potential and tortuosity were determined for each hydrogel, as displayed in Table 2.2. Of note, the ζ-potential was consistent within each set of gels with the same nominal composition, with a linear correlation describing the w/w percentage of acrylic acid and the ζ-potential. One-way ANOVA analysis for the effect of composition (percent acrylic acid) on ζ-potential shows that the effect was significant ($p < 0.001$). Furthermore, as a general trend, for every 1% increase in acrylic acid added to reaction mixture, the ζ-potential changed by -0.9 mV, as shown in Figure 2.2. Regression of all ζ-potential values versus percentage of acrylic acid yielded a correlation that was highly significant ($R^2 = 0.91$, $p < 0.001$). Moreover, the 25% acrylic acid gel composition demonstrated a ζ-potential similar to the OHSC.

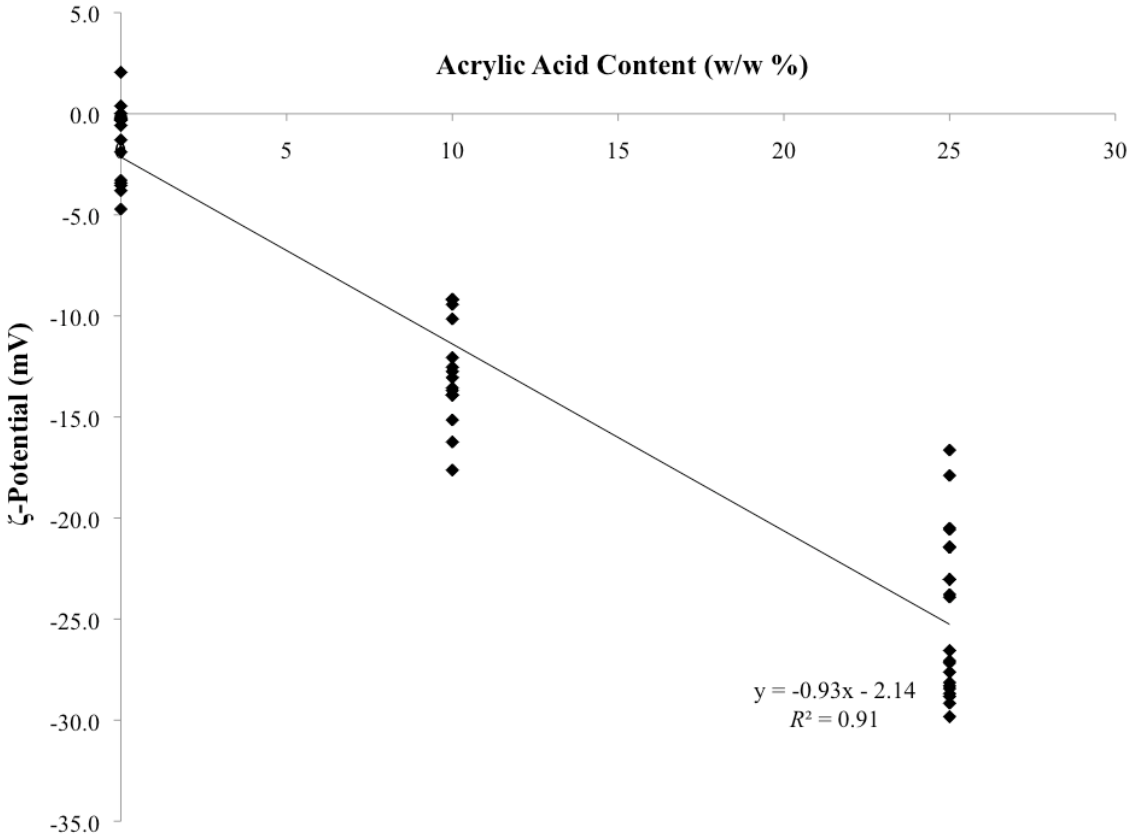

Figure 2.2. Summary of the ζ-potential of each hydrogel as a function of the w/w% acrylic acid. Linear regression fit, $R^2 = 0.91$.

To determine the mass of water within the hydrogels, a series of dehydration experiments was performed, the results of which are shown in Table 2.3. The 25% acrylic acid gel composition had a larger percentage of water than the gels with lower w/w percentages of acrylic acid, with one-way ANOVA revealing a significant difference among the gel types ($p < 0.001$). The fluid content was correlated with the percentage of acrylic acid ($R^2 = 0.73$, $p < 0.001$). This was consistent with the observation that there was greater swelling in gels containing more acrylate as the negative charges attracted counterions with a concomitant fluid influx.[123] It is for this reason that careful equilibration of the gels in HBSS was conducted following synthesis and prior to characterization, with all experimentation utilizing careful control of the pH.

Table 2.2. Summary of ζ-potentials and tortuosities determined by the electrokinetic method.

Gel Type	Gel Code	ζ-Potential (mV)	Tortuosity (λ)	Replicates (N)	Average ζ-Potential (mV)	Average Tortuosity (λ)
0%	0A	-0.3 ± 0.04	1.69 ± 0.16	4	-1.3 ± 0.5[§] (N = 16)	2.28 ± 0.13[§] (N = 16)
	0B	-1.6 ± 1.1	2.56 ± 0.16	6		
	0C	-1.9 ± 0.6	2.39 ± 0.18	6		
10%	10A	-13.1 ± 0.3	2.21 ± 0.12	6	-12.8 ± 0.7[§] (N = 15)	1.80 ± 0.10[§] (N = 15)
	10B	-15.2 ± 0.8	1.46 ± 0.07	5		
	10C	-9.5 ± 0.2	1.61 ± 0.08	4		
25%	25A	-27.9 ± 0.4	1.39 ± 0.03	6	-24.9 ± 0.9[§] (N = 21)	1.44 ± 0.09[§] (N = 21)
	25B	-22.1 ± 0.6	1.07 ± 0.03	6		
	25C	-24.7 ± 1.7	1.71 ± 0.18	9		
25%*	25*	-23.0 ± 0.3	2.36 ± 0.18	4	Not Included	

*Note: the pH for this 25% gel was not adjusted to pH 7-8 before radical polymerization, and is not included in statistical calculations or comparisons.
[§]Note: Groups are statistically different by one-way ANOVA ($p < 0.05$).

The tortuosities for the 70,000 MW fluorescent dextran conjugates as determined by application of an electric field within each gel type are shown in Table 2.2. One-way ANOVA demonstrated a significant effect of composition on tortuosity ($p < 0.001$). Additionally, the tortuosity of each gel measurement was significantly correlated with the percentage of acrylic acid added during synthesis ($R^2 = 0.24$, $p < 0.0002$). Even though there was a significant difference between gel types, there was also a range of tortuosity values within each gel type. This range may be due to minor variability in gel synthesis as a result of imprecise weighing of reagents, measurement error in determining the observed velocity of dextran conjugates in the applied electric field, heterogeneity of the gel matrix itself, and to a much lesser extent, affinity of a molecule for the gel matrix and shrinking or swelling of a gel in response to an applied electric field.[124-130] Shrinking and/or swelling may result from local pH changes and the movement of counterions once an external electric field is applied. This local physical distortion may alter the tortuosity from its equilibrium state in the absence of an applied electric field.

Typically, gels that demonstrate this phenomenon involve higher concentrations of acrylic acid and lower cross-linker concentrations.[128]

Table 2.3. Summary of water content in the various gel types.

Gel Type	Gel Code	Percentage of Water in Gel	Number of Runs (*N*)
25%	25C	98.3 ± 0.1 %	6
10%	10C	97.5 ± 0.3 %	6
0%	0C	96.6 ± 0.1 %	6

To determine whether there is an effect of electric field-inducing shrinking or swelling, the tortuosity in the absence of an electric field in the 25% acrylic acid gel (which is most susceptible to the electric field) was determined. From Equation 2.2, the tortuosity of a system without application of an electric field is obtained by merely observing the diffusion of a fluorescent molecule of interest in the gel, yielding D^*. To arrive at a value for D, we performed Taylor dispersion measurements of the fluorescent dextran conjugates. The results for these experiments are shown in Table 2.4. The resulting diffusion coefficient-based tortuosities for the 70,000 MW **TR70** dextran conjugate in the 25% acrylic acid gel (Gel Code 25C) were compared to the tortuosities obtained electrokinetically. The two tortuosities were not significantly different (p = 0.39). Unlike the 25% acrylic acid gels, the 0% acrylic acid gel should be immune to electric field effects. Thus, as a test of this assumption, D^* for TR70 was also measured in a 0% acrylic acid gel (Gel Code 0C). Again, the resulting diffusion coefficient-based tortuosity was not significantly different from the tortuosity obtained from application of an electric field using ANOVA (p = 0.87). Each of the high and low ζ-potential gel types has a tortuosity that was independent of the characterization method. If electric field-induced swelling or shrinking occurred to a large extent, the two tortuosity measurements would be different in the 25% acrylic acid hydrogels, but not the 0% acrylic acid hydrogels. This was not the case, and therefore the effect of swelling or shrinking of our gels in an electric field was not appreciable.

Table 2.4. Summary of **TR70** and **TR3** Diffusion Coefficients and Tortuosities in 25% and 0% Acrylic Acid Gels.

	Observed Diffusion Coefficient (*D*) (10^{-7} cm^2/s) *25% Gel (25C)***	**Observed Diffusion Coefficient (*D***) (10^{-7} cm^2/s) *0% Gel (0C)***	**Free Diffusion Coefficient (*D*) (10^{-7} cm^2/s) *Free D (CE)***	**Tortuosity *25% Gel***	**Tortuosity *0% Gel***
TR70	0.94 ± 0.09 (*N* = 3)	0.62 ± 0.05 (*N* = 3)	3.66 ± 0.16 (*N* = 32)	1.97 ± 0.20	2.43 ± 0.11
TR30	10.12 ± 1.19 (*N* = 5)	8.44 ± 0.51 (*N* = 4)	10.48 ± 0.48 (*N* = 48)	1.02 ± 0.06	1.11 ± 0.04

The tortuosity, as measured according to Equation 2.2, is to a degree dependent on the hydrodynamic radius of the solute, and by extension its molecular weight.[21, 45, 131] We determined *D** of the smaller **TR3** in the same hydrogels and *D* by Taylor dispersion measurements, with results also shown in Table 2.4. As expected, **TR3** demonstrated faster diffusion than **TR70** in the hydrogels. The tortuosities of the gels as perceived by the solute **TR3** in the 25% and 0% acrylic acid gels were 1.02 ± 0.06 and 1.11 ± 0.04 respectively. These values approached unity and reflect that the diffusion of smaller molecules was relatively unhindered compared to larger molecules.

Other potential sources of error in tortuosity measurement include affinity-type interactions of the fluorophore with the hydrogel matrix and error in determining the diffusion coefficients themselves. Affinity-type interactions are observed in gel electrophoresis applications between the gel matrix and ligand, including with proteins, DNA, and small molecules.[132-134] An affinity-type interaction would result in a slower observed velocity when an electric field is applied, and thus alter both the tortuosity (as measured by electrokinetic or diffusional characterization methods) and ζ-potential measurements. However, our Texas Red dextran conjugates are commercial products that demonstrate very low affinity for biological

extracellular matrices and similarly charged components.[21] Finally, the method of determining diffusion coefficients described in this work was susceptible to error also. The largest source of error was probably the shape of the initial spot of fluorophore. An extended spot will lead to a non-Gaussian profile at short times. This may become almost Gaussian with time, of course. It was for this reason that we rejected experiments in which the fit to the two-dimensional Gaussian curve was poor ($R^2 < 0.95$). Retrospective analysis of these omitted runs demonstrated abnormal fluorophore injections and pressure-induced deformation of the gel matrix.

Aside from measurement errors, there may be gel-to-gel differences among gels of the same nominal composition. For example, differences within a gel type may perhaps arise from the accuracy of weighing small amounts of the bisacrylamide cross-linker used in the hydrogel synthesis. Altering the bisacrylamide cross-linker concentration (and also the total acrylamide concentrations) was shown to alter dramatically the apparent gel pore size and relative mobilities of small nucleic acids.[135] To determine whether the accuracy of the weight of crosslinker was responsible for some of the variability, the bisacrylamide was more accurately weighed (see section 2.2.2) to prepare a series of three 10% acrylic acid gels (Gel Codes 10D,E,F) for comparison to the other 10% acrylic acid gels presented in Table 2.2. The diffusion coefficient (D^*) of **TR70** was then characterized in each of these gels, with data shown in Table 2.5. The average tortuosity for the three gels is 1.62 ± 0.08 (N = 13). This can be compared to the electrokinetically determined tortuosity value of 1.80 ± 0.10 (N = 15) in Table 2.2. While the two methods yielded statistically indistinguishable tortuosity results (p = 0.19), accurate weighing of the bisacrylamide cross-linker reduced the variability of the tortuosity results (variance reduced to 0.07 from 0.16). As such, tortuosity may be better controlled by using a more consistent

bisacrylamide cross-linker concentration. Of note, higher cross-linker concentrations resulted in brittle and opaque hydrogels.

Table 2.5. Summary of **TR70** Diffusion Coefficients and Tortuosity in 10% Acrylic Acid Gel with 4.0 ± 0.1 mg bisacrylamide.

10% Gel Code	Observed Diffusion Coefficient (D^*) (10^{-7} cm^2/s)	Free Diffusion Coefficient (D) (10^{-7} cm^2/s)	Tortuosity
10D	1.07 ± 0.11 (N = 4)	3.66 ± 0.16 (N = 32)	1.85 ± 0.10
10E	2.10 ± 0.10 (N = 5)		1.32 ± 0.04
10F	1.22 ± 0.07 (N = 4)		1.73 ± 0.06

2.4 CONCLUSIONS

Ultimately, poly(acrylamide-*co*-acrylic acid) hydrogels were relatively easy to produce and may represent a useful matrix for analytical or preparative separations and a synthetic surrogate for biological tissue to understand tissue-related electrokinetic phenomena in a simpler, more controllable environment than tissue itself. The ζ-potential of these gels in physiological buffer was, remarkably, nearly directly proportional to the percentage of acrylic acid used in the hydrogel synthesis. As a result, we were able to mimic the electrokinetic properties of brain tissue, as well as removing the ζ-potential from the matrix. This capability will allow for quantitative determination of the degree to which the ζ-potential contributes to solute transport in brain tissue in an electric field. Moreover, the tortuosities of the hydrogels were determined by application of an electric field and by measurement of field-free diffusion coefficients, with the two methods yielding statistically indistinguishable results. While the tortuosities were different

amongst gel types, there was significant variability within each gel type. This variability was probably due to a slight inconsistency between syntheses. It is noteworthy that there is also a considerable difference between the tortuosity of acute rat cortical slices (2.25 ± 0.09)[59] and the tortuosity of rat cortex *in vivo* (2.68 ± 0.11)[61] by measurement of diffusion coefficients. Clearly, the tortuosity of 'soft' matter is highly dependent on conditions.

The ζ-potential, tortuosity, and equilibrium fluid content of the hydrogels were all correlated with the percentage of acrylic acid added during synthesis. This was inconvenient from the perspective of determining the relative importance of the ζ-potential and tortuosity on molecular transport because a change in the acrylate percentage changes both the ζ-potential and tortuosity. However, this correlation is expected. The higher the acrylic acid content, the more swelling is expected – that is, the equilibrium water content is higher. The higher water content leads to a more dilute gel with a larger spacing between polymer chains and thus a lower tortuosity. This internal consistency suggests that the gels studied were at equilibrium, and thus that the results were equilibrium properties of the gels. Moreover, the tortuosities derived from electrokinetic and two-dimensional diffusion coefficient methods were not significantly different. This is the first report in which tortuosity of a material was determined both electrokinetically and by diffusion. This is also, to our knowledge, the first report of the determination of the ζ-potential and tortuosity of hydrogels with correlation of these electrokinetic transport properties with synthetic procedure. Besides representing a synthetic tissue surrogate, the ability to control the gel's properties may afford further utility in the fields of separations, biomaterials, and polymer science.

2.5 ACKNOWLEDGEMENTS

This work was made possible by grant numbers UL1 RR024153 from the National Center for Research Resources (NCRR) and R01 GM044842 from the National Institute of General Medical Sciences, both components of the National Institutes of Health (NIH). Jonathan Cui helped determine the diffusion coefficients in the hydrogels. Yifat Guy assisted in gel preparation and synthesis. Ling Li provided the Taylor dispersion measurement data.

3.0 SHORT-DISTANCE ELECTROKINETIC INFUSION OF MACROMOLECULES AND SMALL MOLECULES IN A GEL MODEL AND ORGANOTYPIC HIPPOCAMPAL SLICE CULTURES

3.1 INTRODUCTION

Our laboratory has demonstrated the utility of electroosmosis for the sampling of extracellular fluid from OHSC.[100] However, it is also theoretically possible to deliver molecules into the extracellular fluid. As discussed previously, this electrokinetic delivery also utilizes the electrophoretic and electroosmotic mobilities of the molecules, the properties of the matrix being ejected into (including the ζ-potential, viscosity, and permittivity), and the applied electric field. The poly(acrylamide-*co*-acrylic acid) hydrogels developed in the previous chapter provide a robust model system to control the degree of electroosmosis that may occur during delivery into a matrix of interest. In fact, localized ejections of molecules have already been implemented in neuroscience research using iontophoresis, though a widespread misconception regarding the mechanism of ejection seems to exist amongst neuroscientists.[136-139]

Iontophoresis includes the movement of ions into biological tissue resulting from the conveyance of an electric current through a solution in contact with that tissue. It is a method of localized delivery that utilizes an electrical current to circumvent the blood-brain barrier,[117] and has even been used to deliver compounds to the brain through the nasal mucosa.[118] Capillary

iontophoresis is used to locally stimulate neuronal pathways by ejections from tiny micrometer sized borosilicate capillary tips to understand neuronal physiology. Traditionally, these ejections utilize low currents (≤ 100 nA) and pulsed millisecond ejection times. In contrast, iontophoresis has been used to deliver solutes outside of the brain by transdermal, transocular,[140, 141] and transurethral routes.[142] Initial experiments by Sir Henry Barcroft and colleagues in 1943 applied epinephrine by 'iontophoresis.'[143] This technique involved wrapping epinephrine-soaked bandages around the arm to determine causes of forearm blood flow variability following nerve blockage. Current transdermal methods traditionally use a pad as a source for solutes being transported into the tissue rather than a capillary. In fact, much of the understanding of electroosmosis in biological systems derives from transdermal iontophoresis, including a well-established appreciation of electroosmosis within the skin pores. Skin has an appreciable ζ-potential within pores and a low ζ-potential elsewhere.[121] However, placement of a pad to perform iontophoresis is only applicable to a target tissue near the surface or deeper tissue exposed through surgery.

With capillary iontophoresis, multi-barrel capillaries became used in standard practice over the course of fifty years of experimental refinement, conventionally composed of two to nine barrels.[144-149] In the most straightforward example, each barrel of the capillary assembly is filled with a solution of ionized drug and the solution is connected to an iontophoresis apparatus (typically a constant-current source) by a suitable electrical lead. The establishment of a potential difference between the drug solution and the medium surrounding the capillary tip causes the movement of ions from the tip, termed the ejection current.[23] The direction of current flow is customarily defined as the flow of positive charges. Thus, an outward, or positive, current causes the ejection of cations, while an inward, or negative, current causes the ejection of anions.

Generally, a small retaining current is applied to prevent movement of the drug from the capillary tip into the extracellular environment due to diffusion and the hydrostatic pressure of the fluid within the capillary.[23] This retaining current has the opposite direction of the ejection current. The discussion thus far, and the literature in general, has been limited to electrophoretic effects, despite the ejection capillary demonstrating a ζ-potential and the opportunity for electroosmotic flow.

Iontophoresis is traditionally believed to be due to electrophoresis within the capillary and resulting diffusion in the tissue,[136-139] despite the derivation of a relationship to explain the contribution of electroosmosis to iontophoretic drug delivery. According to Hill-Smith and Purves, Equation 3.1 gives the electroosmotic volume flow rate, V_{eo}, within a capillary, where ε is the permittivity of the solution, i is the applied current, η is the solution viscosity, σ is the solution conductivity, and ζ is the ζ-potential of the capillary.[150]

$$V_{eo} = \frac{\varepsilon \zeta i}{\eta \sigma} \qquad 3.1$$

Thus, for a given solution, an increased electroosmotic flow rate can be achieved by increasing the applied current or by increasing the ζ-potential within the capillary. The relationship shown in Equation 3.1 was initially developed in 1978 to explain the diminished iontophoretic ejection of anionic molecules into cultured cardiac myocytes.[150] Until recently, the literature was silent regarding electroosmosis within the capillary.[151]

Experimental studies of the electrically induced release of ionized substances from capillaries, such as iontophoresis, must therefore include the contribution of electroosmosis. The transport number is used to mathematically describe the ejection, or flux, of ions from capillaries by an applied iontophoretic current. According to Equation 3.2, the molar flux, Q, is dependent on the applied current, i, the charge valency, Z, Faraday's constant, F, and the transport number,

t.[23, 150]

$$Q = \frac{it}{FZ} \qquad 3.2$$

In current applications of capillary iontophoresis, such as the delivery of compounds into neurological tissue, theoretical descriptions do not take into account the contributions of electroosmosis and correspondingly do not utilize true transport numbers.[23, 152, 153] Therefore, all experimentally observed "transport numbers" are only apparent values, and require an additional term to account for electroosmosis. The true transport number refers to the fraction of iontophoretic current carried by an ion, and can only be estimated by calculation after the contributions of electroosmosis are accounted for. Resultantly, a quantitative understanding of the drug efflux from the capillary tip has not been obtained.[154-156] As there is currently an incomplete theoretical understanding regarding the transport number in iontophoretic ejections, researchers have used microelectrodes[28, 157-162] and fluorescence microscopy[163, 164] to measure the ejection profile of a solute outside of the capillary tip.

Recently, Herr *et al.* showed that electrokinetic transport within the iontophoresis capillary was significant, and furthermore the authors were able to eject neutral solutes,[151] corroborating the theoretical description presented by Hill-Smith and Purves thirty years earlier.[150] The magnitude of electroosmosis developed within a capillary is proportional to the capillary's ζ-potential.[20] The magnitude of the ζ-potential is governed by the surface charge density and the ionic strength of the bulk solvent.[20, 23] Just as the incorporation of electroosmosis into transport models led to better predictions of solute delivery in transdermal iontophoresis,[165, 166] it must also be applied to capillary iontophoresis.

Recent work from our group has demonstrated that the ζ-potential of the matrix being ejected into plays a significant role in the ejection profile of a solute.[164] In the three hydrogels prepared in Chapter 2 with varying ζ-potential, ejections of fluorescent dextran conjugates resulted in penetration distances that were dependent on the ζ-potential of the matrix.[164] Therefore, to more accurately define the ejection profile of a solute into biological tissue, the ζ-potential of the tissue must be known. This previous work also developed a semi-empirical equation to describe the ejection profile of a solute outside of the capillary tip, which is fundamentally based upon electrokinetic transport in the hydrogel or OHSC, including the contributions from electrophoresis and electroosmosis, and diffusion.[164] It has been postulated that electrokinetic transport within the tissue itself may account for the discrepancy between the predicted and experimental ejection profiles during capillary iontophoresis,[167] however this theory was refuted as pulsed iontophoretic currents are traditionally very low (≤ 100 nA) and on too short of a timescale for electrokinetic transport to contribute significantly.[137-139] While this may in fact be true for short, pulsed sequences, the contribution of electrokinetic transport in the tissue remains unknown for more sustained ejection times.

This chapter evaluates the ejection profiles and the distances impacted resulting from ejections in the hydrogel models described in Chapter 2 and in OHSC. This work also exploited longer and more sustained ejection times than used in iontophoresis to approximate steady-state conditions to fit a theoretical description of the concentration profile from a capillary tip. Moreover, the effect of varying a solute's size and electrophoretic mobility and the applied electrical current was evaluated over short-distance electrokinetic transport. Finally, analyzing the current density and tortuosity can account for variable penetration distances between equivalent hydrogels and OHSC.

3.2 THEORETICAL DESCRIPTION OF ELECTROKINETIC TRANSPORT IN TISSUE

The theoretical derivation of the concentration profile of a solute emanating from a pulled capillary tip into a medium with a non-zero ζ-potential was recently derived,[164] with a brief review provided herein.

The Peclet number, *Pe*, is defined by Equation 3.3 as the dimensionless ratio of the time a molecule needs to diffuse a particular distance, *a*, and the time the molecule needs to move the same distance with a particular velocity, *v*, where *D* is the molecule's diffusion coefficient. Thus, *Pe* can provide an indication of the relative degree of convection-enhanced delivery – as compared to diffusion alone – of a molecule from the capillary tip.

$$Pe = \frac{va}{D} \tag{3.3}$$

The concentration profile of a molecule being transported into tissue where μ_{ep} and μ_{eo} are both zero is solely governed by diffusion. At steady-state, the diffusional concentration profile may be described by Equation 3.4, where the concentration, *C*, is a function of the concentration from hemispherical source with radius *a*, the maximal concentration within that hemispherical source, C_0, and the distance from the hemispherical source, *r*.[168]

$$C = C_0 \frac{a}{r} \tag{3.4}$$

In contrast, when both convection and diffusion contribute to the transport from an iontophoresis capillary tip, the steady-state condition in the hemispherical coordinate system can be mathematically described by Equation 3.5.

$$J = Cv - D\nabla C \tag{3.5}$$

where J and v are the flux and velocity of the molecule, respectively, and D is the diffusion coefficient of the molecule. The first term refers to the contribution of convection to overall flux, which includes v_{eo} and v_{ep}. The second term describes the contribution of diffusion to overall flux, which results from a concentration gradient, as described by Fick's first law.[30] It is assumed that the electric field emanating from the iontophoresis capillary tip into the medium of interest (i.e.: tissue) is equivalent to the field from a hemispherical electrode, as described by Equation 3.6, where the electric field, E, at a particular distance from the source, r, is related to the radius of the hemispherical source, a, and the maximum electric field where r is equal to a, E_0.

$$E(r) = \frac{a^2}{r^2} E_0 \tag{3.6}$$

The electric field determined by Equation 3.6 may be multiplied by the observed mobility, μ_{obs}, of a compound to arrive at the velocity term in Equation 3.5. The differential equation is solved to result in Equation 3.7, where Pe is the Peclet number. This expression describes the concentration of molecule expected at a dimensionless distance, ρ, during iontophoretic ejections. When electrokinetic effects become negligible (such as with no applied electric field), Pe is approximately zero. If the exponentials in Equation 3.7 are expanded as a Taylor series, with truncation of the quadratic and higher order terms, Equation 3.4 may be recovered.

$$C(\rho) = C_0\left(\frac{1-e^{-Pe/\rho}}{1-e^{-Pe}}\right) \qquad 3.7$$

3.3 EXPERIMENTAL

3.3.1 Chemicals and Solutions

The following materials were purchased from Sigma (St. Louis, MO) and used as received, unless otherwise noted. Solutions were prepared with Millipore Synthesis A10 system 18 MΩ purified water (Millipore, Billerica, MA). Glucose-free HEPES-buffered salt solution (GF-HBSS) contained in mM: 143.4 NaCl, 5 HEPES, 5.4 KCl, 1.2 $MgSO_4$, 1.2 NaH_2PO_4, and 2.0 $CaCl_2$. GF-HBSS was filtered, stored frozen, warmed to room temperature, and ultrasonicated for ten minutes prior to use. HBSS contained the same component concentrations as GF-HBSS, with an additional 10 mM *D*-(+)-glucose, and underwent the same preparation and storage process. GBSS was made up of 27.5 mM *D*-(+)-glucose and 2.7 mM $MgSO_4$ supplemented to Gey's Balanced Salt solution. GBSS was filtered, stored in the refrigerator, and warmed to 37 °C prior to use. The OHSC culture medium contained the following components from Gibco (Invitrogen, Eugene, OR): 50% Opti-MEM, 25% heat-inactivated Horse Serum, and 25% Hanks' Balanced Salt Solution, supplemented with 2% vitamin B-27 and 1% *D*-(+)-glucose.[169] The medium was filtered, stored in the refrigerator, and warmed to 37 °C prior to use.

Texas Red dextran conjugate 70 kDa (**TR70**) and Texas Red dextran conjugate 3 kDa (**TR3**) were obtained from Invitrogen and diluted to 0.06 mM and 0.2 mM respectively with GF-HBSS and filtered. The fluorophore solutions were frozen until use. Tris(2,2'-

bipyridine)ruthenium (abbreviated $Ru(bpy)_3^{2+}$) was obtained from Sigma and diluted to make a solutions of 1.3 mM $Ru(bpy)_3^{2+}$ in 150 mM aqueous NaCl supplemented with 5 mM HEPES buffered at pH 7.4. A mixture of 0.19 mM **TR70** and 0.29 mM **FL70** in GF-HBSS was made for use in ζ-potential measurements, as described in Chapter 2. For the diffusion coefficient measurements, solutions were made in GF-HBSS to concentrations of: **TR70** (0.03 mM), **FL70** (0.03 mM), **TR3** (0.67 mM), and $Ru(bpy)_3^{2+}$ (3.51 mM). For cell death analysis, a stock solution of 0.35 mM propidium iodide in GBSS was prepared and frozen until use.

3.3.2 Determination of Free Diffusion Coefficients

Diffusion coefficients were determined by Taylor dispersion measurements, as described in section 2.2.6.

3.3.3 Determination of Electrophoretic Mobilities

The electrophoretic mobilities of the fluorophores were determined in GF-HBSS by capillary zone electrophoresis (CZE) with a diode array UV absorbance detector using 50 μm inner diameter (ID) fused silica capillaries and an Agilent CE system (Agilent Technologies, Palo Alto, Ca). Hydrodynamic injections (25 mbar, 4 second) were employed, and all experiments were performed at 25 °C. For **TR70** ($\lambda_{detection}$ = 595 nm), **TR3** (595 nm), **FL70** (494 nm), and $Ru(bpy)_3^{2+}$ (452 nm), an unmodified fused silica capillary (Polymicro Technologies, Phoenix, AZ) was employed. The capillary was preconditioned with 1 M NaOH for 15 minutes, 18 MΩ-cm water for 15 minutes, GF-HBSS for 15 minutes, and was flushed with running GF-HBSS for 2 minutes in between fluorophore injections. Rhodamine B (544 nm) was used as a

neutral flow marker. The capillary was 33.0 cm in total length, 8.5 cm to the detector, and the separation voltage was 6.0 kV (182 V/cm). Fluorophores were dissolved in GF-HBSS and had concentrations ranging from 0.3 to 1.7 mM.

3.3.4 Synthesis of Hydrogels

Poly(acrylamide-*co*-acrylic acid) hydrogels were prepared with the purpose of creating matrices with different ζ-potentials and tortuosities similar to those of brain tissue by a thermally-initiated radical polymerization reaction, as described in the procedure presented in section 2.2.3.

3.3.5 Characterization of the ζ-Potential and Tortuosity

The experimental apparatus was used without modification from our previously reported setup.[22] A four-electrode potentiostat coupled with a differential amplifier and reference Luggin capillary electrodes was used to provide feedback control of the electric field in the gel. The ζ-potential and tortuosity for each gel were determined with this setup,[22] as described in greater detail in section 2.2.4.

3.3.6 Water Content of Hydrogels

The water content of each hydrogel was determined by dehydration and the mass of water lost, as described in section 2.2.7.

3.3.7 Conductivity of Hydrogels

Due to the high water content of the hydrogels, as determined in Chapter 2, the conductivity was assumed to be equivalent to the fluid (GF-HBSS). The conductivity of GF-HBSS was measured using a CON 6/TDS 6 conductivity/TDS meter (Eutech Instruments Pte Ltd/Oakton Instruments, Vernon Hills, IL).

3.3.8 Organotypic Hippocampal Slice Cultures (OHSC)

The organotypic hippocampal slice culture (OHSC) method was developed by Stoppini *et al.,*[92] and used with slight modification. This procedure was approved by the University of Pittsburgh Institutional Animal Care and Use Committee. Bilateral dissections of the hippocampi were done on 9-day postnatal Sprague-Dawley albino rat pups. The hippocampi were chopped along their transverse axes using a McIlwain tissue chopper (Mickle Laboratory Engineering, Surrey, England) to yield 350 μm thick slices. The slices were positioned on 0.4 μm PTFE insert membranes (Millipore, Bedford, MA) and incubated over 1.2 mL of culture medium at 36.5 °C in 5 % CO_2/95 % air for 6 to 8 days. The culture medium was exchanged every 2 to 3 days. Prior to use, the culture medium was substituted with 37 °C GBSS and incubated for thirty minutes. A second exchange with GBSS was conducted with for incubation for another 30 minutes. A final exchange to HBSS warmed to 37 °C was conducted and incubated for 30 minutes.

3.3.9 Electrokinetic Ejections into Hydrogels

Borosilicate capillaries (1 mm by 0.58 mm, 4 inches long) with filaments (A-M Systems, Inc., Carlsborg, WA) were pulled to tips of approximately 2 μm inner radii using the Sutter P-2000 capillary puller. Tip sizes and shape were measured using an Olympus BX41 optical microscope. Figure 3.1 shows a 0.25 inch thick PVC cell with a 1 cm by 1 cm space at its center. This cell has a 1 mm wide by 1 mm high by 2.2 cm long channel milled at its base. The cell was slightly larger than the standard cover slip glued to its base. The cell was secured on an Olympus IX-81 inverted fluorescence microscope stage, and experiments were imaged with a high-resolution charged-coupled device camera (ORCA-ER).

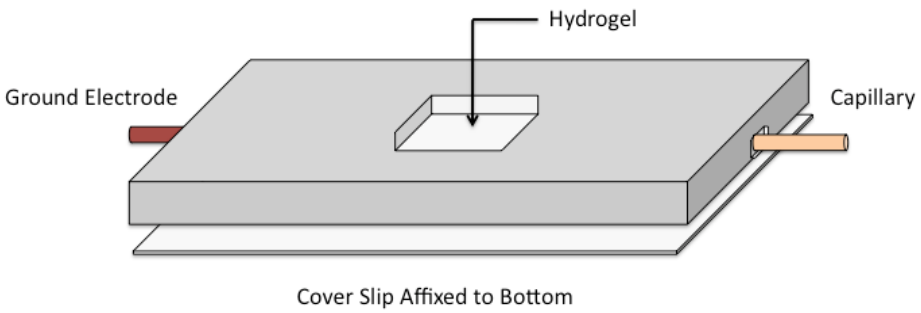

Figure 3.1. Experimental setup for electrokinetic ejections into hydrogels. A glass coverslip was affixed to the bottom of the PVC cell. A hydrogel square was placed in the center space of the cell. A pulled borosilicate capillary (pipette) was inserted into the hydrogel through the channel. On the other end of the channel, an Ag ground electrode was inserted into the hydrogel.

Hydrogel pieces were cut and placed in the cell to completely cover the exposed glass cover slip below. The hydrogel thickness was greater than 5 mm in all instances. The pulled borosilicate capillary was carefully inserted through one side of the channel and into the hydrogel. On the other side of the channel, an Ag ground electrode (0.3 mm diameter) was inserted a few millimeters into the hydrogel. The distance between the capillary tip and the

ground electrode was always greater than 3.5 mm. A second Ag working electrode was inserted into the back end of the capillary to complete the electrical circuit. A Digital Midgard™ Precision Current Source iontophoretic pump (Stoelting Co., Wood Dale, IL) or Princeton Applied Research 173 potentiostat (PAR) (Princeton, NJ) were used as the constant current source. The current source was attached to the secured Ag electrodes through a circuit containing a relay switch, as reported previously.[164] Image sequences were acquired using MetaMorph 7.6.2.0 software (MDS Analytical Technologies, Sunnyvale, CA) using an UPlan Fl 4×, UPlan S Apo 10×, or a long working distance LUCPlan Fl N 40× Olympus objective lens. The MetaMorph software triggered the initiation and termination of the current during image acquisition. The PAR was used for **TR70** with 0.1, 0.2, 0.4, 0.5, and 0.6 μA currents. Additionally, the PAR setup incorporated a 0.3 mm diameter platinum electrode as the working electrode (instead of Ag) to avoid capillary obstruction due to precipitation of AgCl. The Midgard™ pump or the PAR potentiostat monitored the electrical potential across the system as a constant current was applied. The currents ran from 270 to 840 seconds.

The penetration distance was obtained from image sequences by utilizing a line scan from approximately the center of the capillary tip to the edge of the viewfield on the same plane as the injection capillary. The intensity data were recorded along the line scan prior to the initiation of current (to obtain the background intensity) and at 30 seconds intervals following initiation of the current. The background intensity was subtracted from the corresponding intensity along the line scan. Given that concentration is related to the fluorescence intensity measured, the concentration, C, was replaced in Equation 3.7 with intensity, I. The reported fluorescence intensity values were between 0 and 4,095. Values of I_0, I_1, and Pe were obtained

by nonlinear fitting of Equation 3.8 to the line scan data using Mathcad 14 (PTC, Needham, MA). I_1 was included in this equation to correct for the background intensity.

$$I(\rho) = I_0\left(\frac{1-e^{-Pe/\rho}}{1-e^{-Pe}}\right) + I_1 \qquad 3.8$$

The dimensionless penetration distance, ρ, which was obtained from Equation 3.8 may be multiplied by the capillary tip radius to arrive at the penetration distance in SI units of distance, otherwise denoted as r.

3.3.10 Electrokinetic Ejections into OHSC

Experiments in the OHSC were conducted, as shown in Figure 3.2, with the Digital Midgard™ iontophoresis pump as the constant current source. An insert membrane with an OHSC was placed in a glass dish with HBSS. An Ag ground electrode was secured remotely and immersed in the HBSS bath. A pulled borosilicate capillary was filled with a fluorophore solution and positioned at a 20° angle versus the plane of the OHSC and insert membrane using a manipulator arm affixed to a Narishige NMN-21 micromanipulator (Tokyo, Japan). The capillary tip was introduced into the CA1 region of the OHSC. An Ag working electrode was inserted into the distal end of the capillary to make electrical contact. The electrode circuitry and imaging parameters were analogous to the hydrogel experiments.[164] A 0.5 μA current was applied using the iontophoresis pump for up to 270 seconds.

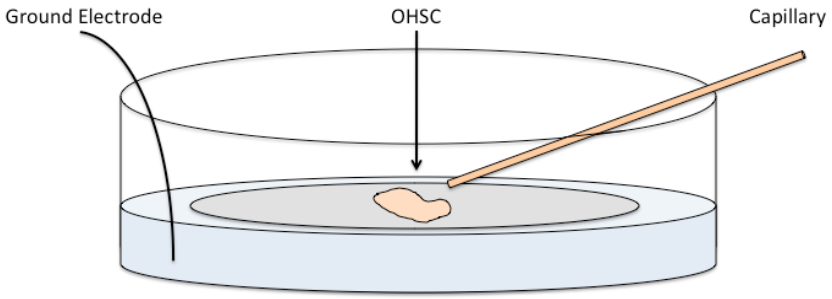

Figure 3.2. Experimental setup for electrokinetic ejections into OHSC. An OHSC and its insert membrane are placed over HBSS in a glass dish. An Ag ground electrode is placed remotely in the bath. An Ag working electrode is placed distally in a borosilicate capillary that is inserted into the OHSC at a 20° angle.

3.4 RESULTS AND DISCUSSION

3.4.1 Fluorophore, Hydrogel, and Capillary Properties

The free solution diffusion coefficients (D), as measured by the Taylor dispersion method, and the electrophoretic mobilities (μ_{ep}) of the fluorophores, as measured by capillary zone electrophoresis, are provided in Table 3.1. As described in Chapter 2, **TR70** demonstrated an approximately zero μ_{ep}, while **FL70** had a more negative μ_{ep}. The small, divalent cation, $Ru(bpy)_3^{2+}$, had a substantial and positive μ_{ep}. Furthermore, the observed diffusion coefficients were inversely correlated with molecular weight and size. These two properties of the fluorophore helped determine the ejection profile and penetration distances resulting from electrokinetic ejections.

To assess the relative degree of electrophoresis versus electroosmosis that was likely to be observed during electrokinetic transport of the solutes in the gels, a ratio of the ζ-potential of the hydrogels to the ζ-potential of the solute was compared to unity, as previously described.[164]

All of these ratios were substantially larger than unity except for two conditions – **TR70** and **TR3** in the 0% acrylic acid hydrogel. Therefore, the transport of dextran conjugates in an applied electric field was dominated by electroosmosis within the more highly charged hydrogels with a ζ-potential similar to brain tissue.

Table 3.1. Fluorophore properties (mean ± SEM).

	Observed Free Diffusion Coefficient (*D*) (10^{-10} m^2/s)	**Electrophoretic Mobility (μ_{ep}) (10^{-9} m^2/Vs)**
TR70	0.37 ± 0.02 (*N* = 32)	0.46 ± 0.03 (*N* = 3)
FL70	0.38 ± 0.01 (*N* = 48)	-8.80 ± 0.2 (*N* = 3)
TR3	1.05 ± 0.05 (*N* = 48)	2.56 ± 0.04 (*N* = 3)
$Ru(bpy)_3^{2+}$	3.70 ± 0.34 (*N* = 48)	25.86 ± 0.02 (*N* = 3)

The ζ-potentials, tortuosities, and fluid content of the hydrogels were extensively described in Chapter 2. Of note, the 25% w/w acrylate gel had a similar ζ-potential to the OHSC. Because the fluid fraction was so high in the hydrogels (roughly 96 to 98%), the electrical conductivity of the hydrogel was approximated as the fluid fraction of the hydrogel multiplied by the GF-HBSS buffer solution. The conductivity of GF-HBSS, was measured to be 1.62 S/m. At pH 7.40, GF-HBSS demonstrated an ionic strength of 0.15 M.

The approximately -10 mV ζ-potential calculated for the borosilicate capillary was consistent with other forms of borosilicate glass.[170-173] In addition, a ζ-potential of approximately -10 mV was also consistent with the experimental observation that the borosilicate capillary ζ-potential must be more positive than -11 mV, as ζ-potentials less than -11 mV (and thus a greater magnitude) are capable of ejecting **FL70** (μ_{ep} = -8.8 × 10^{-9} m^2/Vs)[21] from the capillary tip. In

fact, no ejection of **FL70** from the capillary into the -23.0 mV ζ-potential hydrogel was observed.[164]

The rate of electroosmotic transport within the capillary tip may not equate to the same rate of electroosmotic transport outside of the tip. This may be due a difference between the ζ-potential within the capillary and the ζ-potential of the matrix outside of the capillary. Two adjacent media with different ζ-potentials in an electric field create a pressure at the interface between the two media, in a phenomenon termed "ζ-potential mismatch."[20, 174] Thus, when the hydrogel ζ-potential magnitude is smaller than the capillary ζ-potential magnitude, such as with the lowest acrylic acid content hydrogels, the possibility exists for pressure development and hydrogel deformation near the tip. For example, if a solution containing a neutral molecule is ejected into a neutral gel, the *Pe* in the gel is theoretically zero. However, the negative ζ-potential within the capillary will result in expulsion of some of the solution into the hydrogel. This generates a positive pressure at the interface between the capillary tip and hydrogel, and thus provides the potential for pressure-driven transport, in addition to diffusional transport away from the tip. As a result, the *Pe* that is observed under these conditions may actually be greater than zero due to pressure-driven transport. The extent of the developed pressure relies on a myriad of factors, and therefore estimating its true effect is not trivial. No pressure deformation of the hydrogels or OHSC was observed during electrokinetic ejections, however.

3.4.2 Time to Steady-State During Ejections

Steady-state was defined in this work as a constant fluorescence intensity at $\rho = 1$ (just outside of the capillary tip) for more than two 30 second time intervals. Table 3.2 provides the times to reach steady-state for each experiment. The average times to steady-state for **TR70** were

207 seconds and 233 seconds for 1.0 μA current ejections into the -0.25 and -9.5 mV ζ-potential hydrogels respectively. The same current for ejection of **TR70** into the -23.0 mV ζ-potential hydrogel did not reach steady-state, however. The average times to steady-state for 1.0 μA current ejections of **TR3** into the -0.25 and -9.5 mV ζ-potential hydrogels were 423 and 510 seconds respectively. The same current for ejection of **TR3** into the -22.1 mV ζ-potential hydrogel also did not reach steady-state. Taking this data as an example of a trend, increasing the ζ-potential, and by extension the degree of electroosmosis, of a medium subsequently increased its time to steady-state. Of note, the **TR70** and **TR3** experiments were truncated at 270 and 540 seconds respectively (sometimes before reaching steady-state) due to the possibility of electrochemical reactions within the capillary and dehydration of the hydrogel during a prolonged experiment.

Table 3.2. Experimental parameters for each data series.

Solute	Hydrogel ζ-Potential (mV)	$\left\lvert \frac{\zeta_{Hydrogel}}{\zeta_{Solute}} \right\rvert$	Current (μA)	Average Time to Steady-State (seconds)	*Pe*	*Pe* SEM	*N*
TR70	-0.25	0.43	1.0	207	6	0.74	9
TR70	-9.5	16	0.5	240	12	0.34	5
TR70	-9.5	16	1.0	233	13	2.1	11
TR70	-23.0	40	1.0	Non Steady-State	27	1.4	9
TR70	-24.7	43	0.1[§]	366	15	0.47	3
TR70	-24.7	43	0.2[§]	492	18	0.88	5
TR70	-24.7	43	0.4[§]	780	27	0.76	4
TR70	-24.7	43	0.5[§]	953	36	1.5	4
TR70	-24.7	43	0.6[§]	1030	39	4.6	3
TR3	-0.25	0.077	1.0	423	16	0.36	11
TR3	-15.2	4.7	0.5	498	37	1.3	13
TR3	-15.2	4.7	1.0	510	51	1.3	8
TR3	-22.1	6.8	1.0	Non Steady-State	52	3.2	10
TR3	-24.7	7.6	0.5	Non Steady-State	69	4.9	6
TR3	-24.7	7.6	1.0	Non Steady-State	73	2.5	6

[§]Current applied through the PAR circuit. All other experiments were run using the Digital Midgard™ Precision current source.

Increasing the applied electrical current for **TR70** ejections into the -24.7 mV ζ-potential hydrogel also increased the time to steady-state from 366 seconds at 0.1 μA to 1,030 seconds at 0.6 μA (with 1.0 μA not reaching steady-state during the experimental time), as shown in Figure 3.3. In contrast, ejections of **TR3** into the same hydrogel were not at steady-state for any current tested. Our data indicated that smaller molecules require a longer time to achieve steady-state during constant-current ejections. Under constant-current conditions from a hemispherical microelectrode, comparable to the experimental setup described in this chapter, the time to steady-state depended on the diffusion coefficient of the molecule and the electrode size.[175] With a constant capillary tip size, the time to steady-state also appeared to be correlated with molecular weight, as indicated by **TR70** reaching steady-state much faster than **TR3** for equivalent ejections.

Steady-state is achieved when the flux of molecules through the capillary tip equals the flux of the same molecules away from the capillary tip into the matrix. These two processes may not always occur with the same rates, and thus one may be rate-limiting. These rates are a function of the ratio of the electroosmotic flow that exists between the capillary and the outside matrix, the diffusion coefficient of the molecule, and the tortuosity of the matrix. If the outside matrix was held at a constant -24.7 mV ζ-potential, as shown in Figure 3.3, the time to steady-state was linearly dependent on the applied current for **TR70** ejections (R^2 = 0.994) from 0.1 to 0.6 μA. Assuming this linear relationship holds at slightly higher currents, the time to steady-state for 1.0 μA ejections of **TR70** can be estimated as 1,610 seconds. This was not determined experimentally due to truncation of ejection times. In contrast, Table 3.2 indicates the time to steady-state for 1.0 μA ejections of **TR70** as 207 seconds and 233 seconds in the -0.25 and -9.5 mV ζ-potential hydrogels respectively.

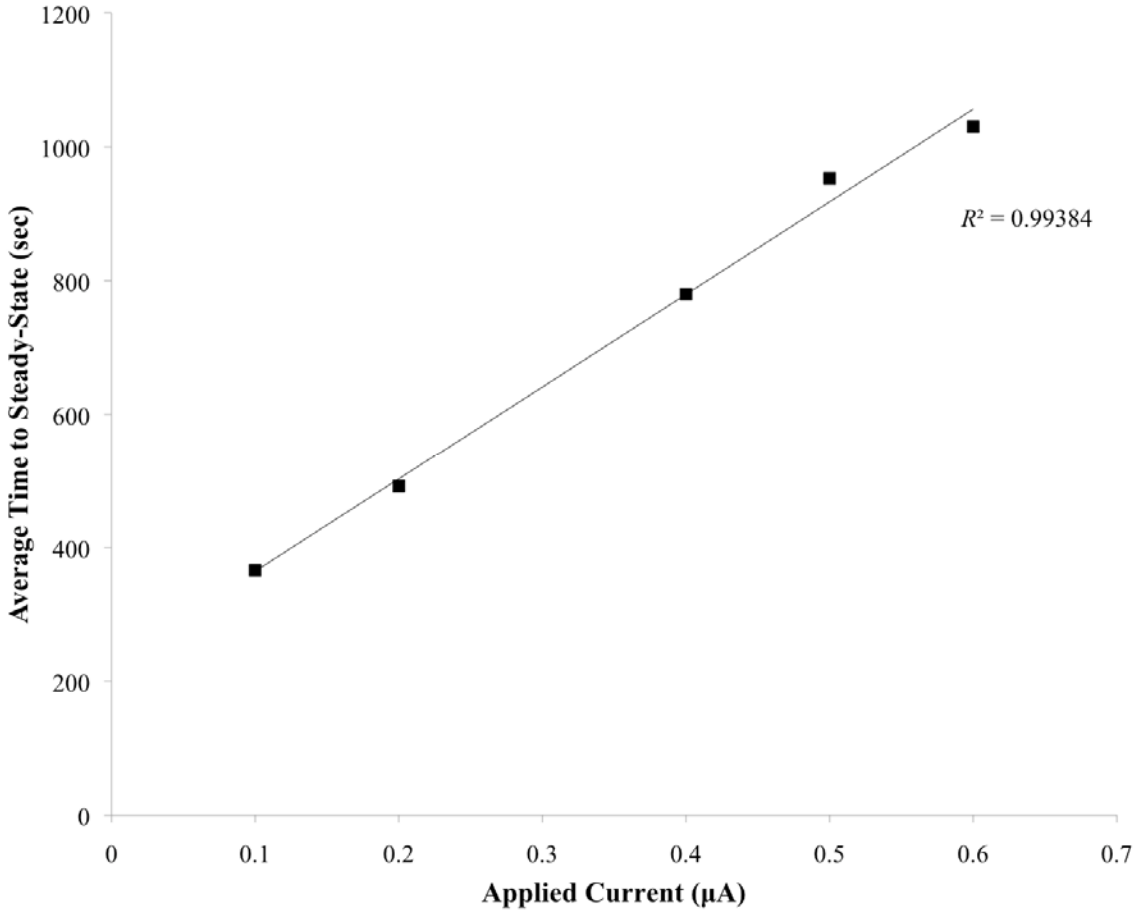

Figure 3.3. Average time to steady-state for ejections of **TR70** under variable currents in a hydrogel with -24.7 mV ζ-potential demonstrated a linear correlation with $R^2 = 0.994$.

In the case of the -0.25 and -9.5 mV ζ-potential hydrogels, the capillary ζ-potential was of greater magnitude than that of the hydrogel. Thus, for a given current, the borosilicate capillary developed a greater degree of electroosmosis than the hydrogel, with a concomitant ejection. Because the flux of molecules through the capillary tip was larger than the transport of the molecules away from the tip and into the matrix, there was a faster accumulation of molecules just outside of the capillary tip at $\rho = 1$. This resulted in a shorter time to steady-state. Conversely, a similar ejection of **TR70** into the -24.7 mV ζ-potential hydrogel demonstrated a much slower time to steady-state. In this instance, the magnitude of the hydrogel ζ-potential

greatly exceeded that of the borosilicate capillary. As a result, the transport of molecules away from the tip and into the matrix was larger than the flux of molecules through the capillary tip. This resulted in a slower accumulation of molecules just outside of the capillary tip at $\rho = 1$, with a resulting slower time to steady-state.

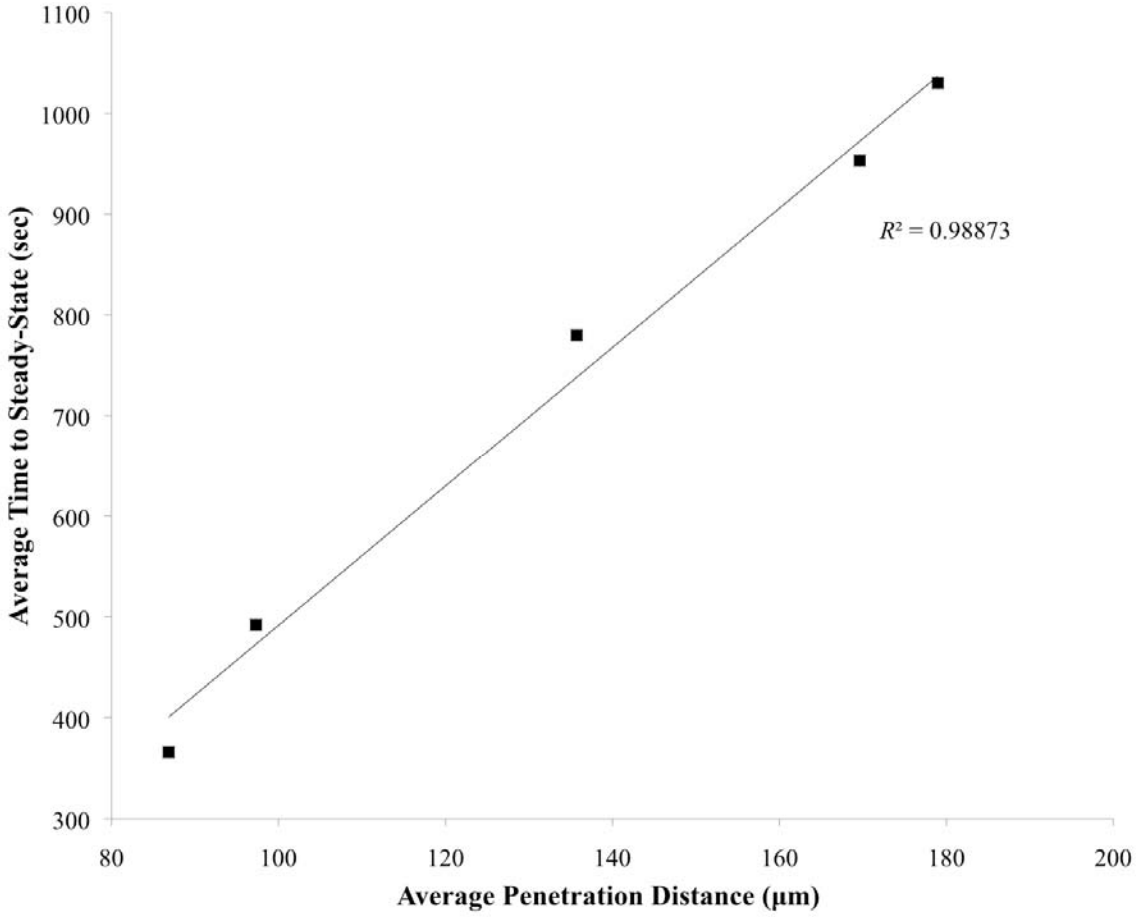

Figure 3.4. Relationship of the average penetration distance (µm) where $I(\rho)/I_0$ was equal to 0.25 with the average time to steady-state for ejections of **TR70** in a hydrogel with -24.7 mV ζ-potential with 0.1, 0.2, 0.4, 0.5, and 0.6 µA demonstrated a linear correlation with $R^2 = 0.989$.

Furthermore, the average penetration distance in micrometers, r, where $I(\rho)/I_0$ was equal to 0.25 was also linearly correlated with the time to reach steady-state for **TR70** ejections into a -24.7 mV ζ-potential hydrogel with currents ranging from 0.1 to 0.6 µA ($R^2 = 0.989$), as shown in

Figure 3.4. This further supported the hypothesis that the rate of molecular transport away from the capillary tip determined the time to steady-state. The rate of electrokinetic transport away from the capillary tip into the matrix depends on the applied electrical current and the electric field at the capillary tip. Therefore the average penetration distance is greater for ejections with higher currents with a particular capillary tip size and at a given point in time.

In hydrogels of varying ζ-potentials, the time to steady-state may also be correlated with the Peclet number. With transport solely due to diffusion, where *Pe* is zero, the time to steady-state depends on the radius of the capillary tip. However, introduction of convective transport, such as though electrokinetic means, increases the *Pe*. Figure 3.5 shows the linear relationship between *Pe* and the time to steady-state for **TR70** ejections into a -24.7 mV ζ-potential hydrogel with applied electrical currents ranging from 0.1 to 0.6 μA (R^2 = 0.985). Since *Pe* was determined at $\rho = 1$ and was related to the flow rate of a molecule through the capillary tip, this data further substantiated the hypothesis that an increased time to steady-state may result from an increase in the flux of a molecule through the capillary tip. Similar to the discussion a moment ago, the electric field at the capillary tip determines the rate of electrokinetic transport away from the tip into the matrix. Increasing the applied electrical current has two effects: it increases the rate of fluid moving through the capillary tip resulting in a higher *Pe*, but it also increases the rate of electrokinetic transport away from the tip into the matrix, which ultimately results in a greater penetration distance at a given point in time.

Finally, if a molecule with zero electrophoretic mobility is assumed, as is roughly the case for **TR70**, its observed velocity is the electroosmotic velocity of the solvent. The electroosmotic velocity through the capillary tip may be calculated from the Helmholtz-Smoluchowski equation for each applied electrical current.[20] The value of ζ used in this

calculation reflected the -10 mV ζ-potential of the borosilicate capillary.[170-173] The volumetric flow rate through the capillary tip was linearly related to the average time to steady-state for **TR70** ejections, as shown in Figure 3.6 (R^2 = 0.994), indicating that increased an increased flow rate resulted in an increased time to steady-state in a hydrogel with a ζ-potential similar to OHSC.

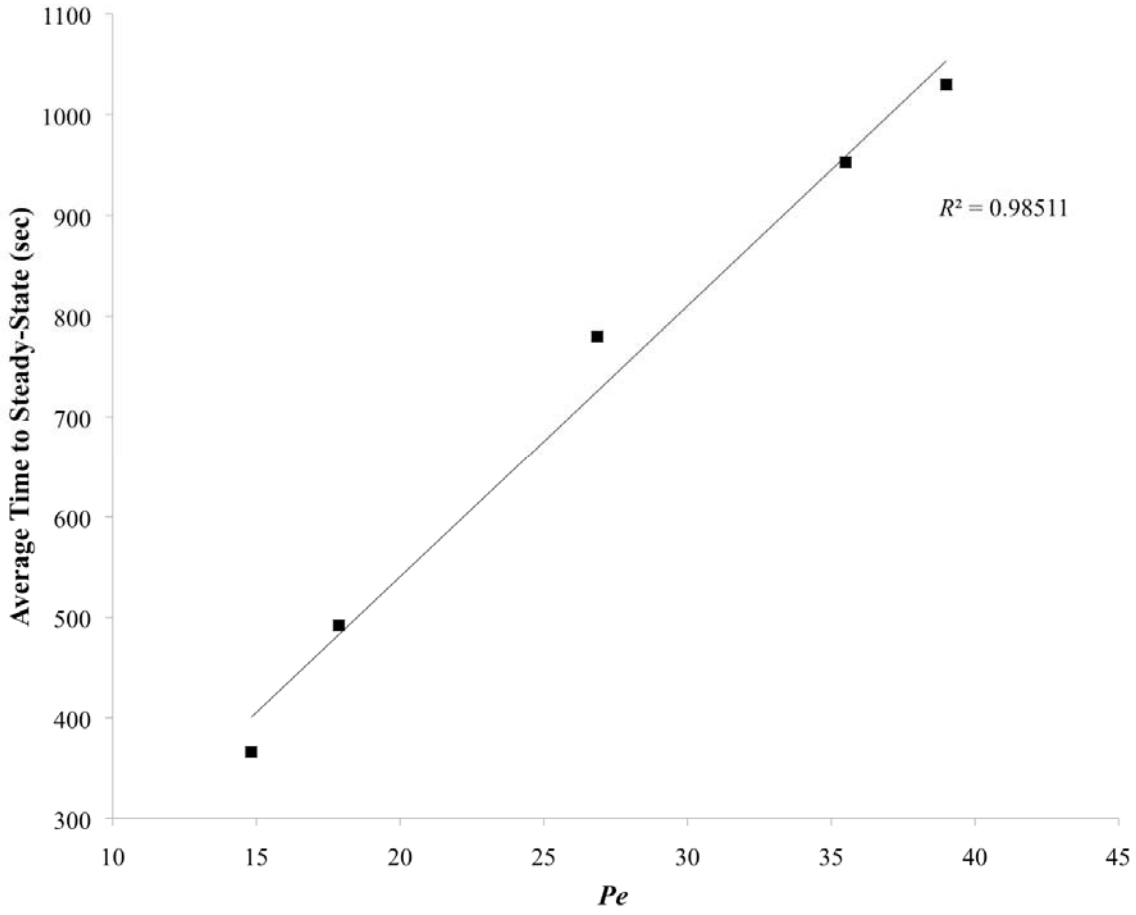

Figure 3.5. Relationship of Peclet number (*Pe*) with the average time to steady-state for ejections of **TR70** in a hydrogel with -24.7 mV ζ-potential with 0.1, 0.2, 0.4, 0.5, and 0.6 μA demonstrated a linear correlation with R^2 = 0.985.

Thus, this discussion has described the factors correlated with the time required to achieve steady-state. These factors include varying the applied current, the ζ-potential of the

medium outside the capillary tip, the penetration distance a molecule achieves, *Pe*, and the flow rate from the capillary tip. Furthermore, the time required to reach steady-state could be especially long with certain experimental parameters, such as with larger capillary tip sizes due to an increased flow rate.

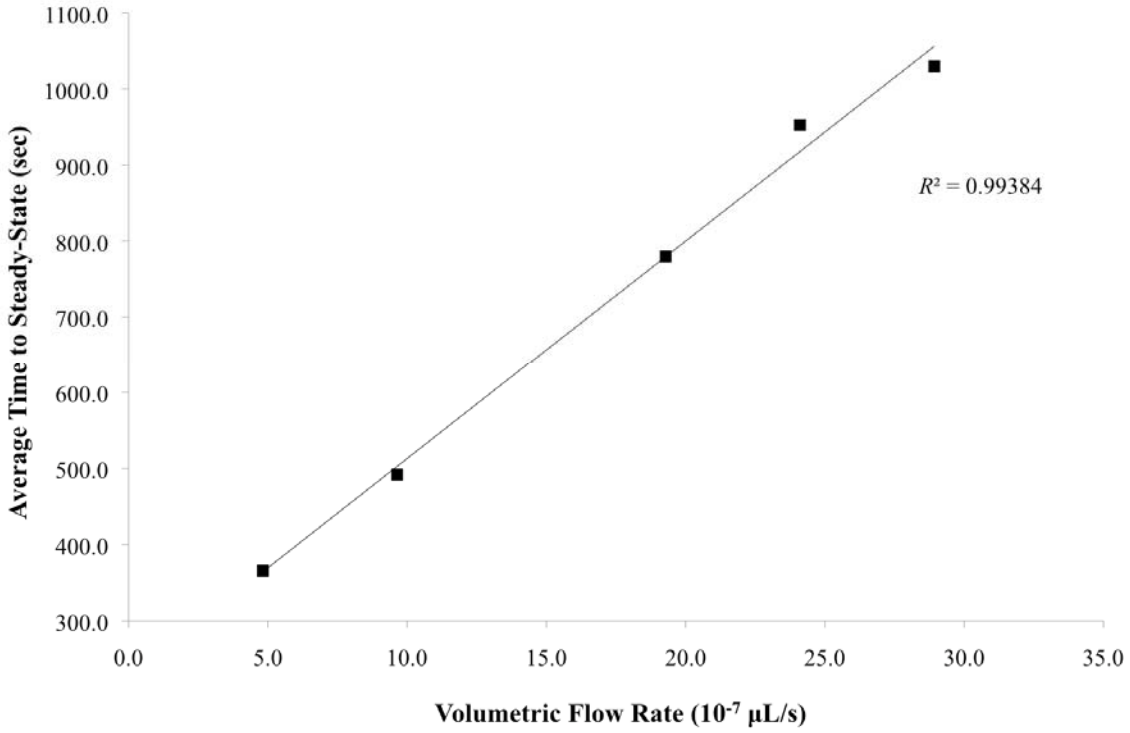

Figure 3.6. Relationship of the average time to steady-state (sec) with the volumetric flow rate through the capillary tip for ejections of **TR70** in a hydrogel with -24.7 mV ζ-potential with 0.1, 0.2, 0.4, 0.5, and 0.6 µA demonstrated a linear correlation with $R^2 = 0.994$.

3.4.3 Evaluation of the Penetration Distance During Ejections

Fitting the fluorescence intensity profiles to Equation 3.8 yielded values for *Pe*, in addition to characteristic penetration distances where $I(\rho)/I_0$ was equal to 1, 0.75, 0.50, and 0.25. The fits for each experiment produced R^2 greater than 0.98, despite some hydrogels (-23.0 and -

24.7 mV ζ-potential) only approaching steady-state with 1.0 μA in the experimental time frame. The dimensionless penetration distance, ρ, which was obtained from Equation 3.8, may be multiplied by the capillary tip radius to arrive at the penetration distance in SI units of distance, otherwise denoted as r. The results of these experiments are shown in Table 3.3.[164]

The nearly neutral dextran conjugate, **TR70**, represents a marker for electroosmosis occurring within each hydrogel. Of note, **TR3** was carried much deeper into the hydrogels, presumably due to its slightly positive electrophoretic mobility, smaller molecular size, and lower tortuosity in the hydrogel matrix. In the hydrogels with biologically-similar ζ-potentials of -23.0 and -24.7 mV, r where $I(\rho)/I_0$ was equal to 0.25 were approximately 90 and 330 μm for 1.0 μA ejections of **TR70** and **TR3** respectively. In contrast, similar 1.0 μA ejections of **TR70** and **TR3** in the hydrogel with the lowest ζ-potential (-0.25 mV) yielded r where $I(\rho)/I_0$ was equal to 0.25 of only roughly 25 and 115 μm respectively. Thus, a matrix with a higher magnitude ζ-potential outside of the capillary tip developed a greater degree of electrokinetic transport with a resultantly greater penetration distance.

Table 3.3. Penetration distances for **TR70** and **TR3** as a function of hydrogel ζ-potential (data mean ± SEM).

Solute	Hydrogel ζ-Potential (mV)	Current (μA)	ρ $I(\rho)/I_0 = 0.75$	ρ $I(\rho)/I_0 = 0.50$	ρ $I(\rho)/I_0 = 0.25$	*Pe*	*N*
TR70	-0.25 ± 0.04	1.0	2.80 ± 0.20	6.42 ± 0.57	16.37 ± 1.52	6.0 ± 0.7	9
TR70	-9.5 ± 0.2	1.0	8.07 ± 0.68	15.28 ± 1.62	28.46 ± 2.60	13.4 ± 2.1	11
TR70	-23.0 ± 0.3	1.0	16.70 ± 0.88	27.94 ± 1.05	45.47 ± 1.46	27.3 ± 1.4	9
TR3	-0.25 ± 0.04	1.0	8.86 ± 0.41	22.88 ± 0.54	57.93 ± 1.93	16.2 ± 0.4	11
TR3	-15.2 ± 0.8	1.0	18.21 ± 1.37	47.68 ± 2.92	113.60 ± 3.57	44.3 ± 2.6	13
TR3	-22.1 ± 0.6	1.0	22.57 ± 1.20	57.62 ± 3.12	132.58 ± 6.56	51.9 ± 3.2	10

Furthermore, the penetration distances for the 0% acrylic acid hydrogel (ζ = -0.25 mV) should be similar to that for diffusion alone for molecules with an electrophoretic mobility equal to zero. However, the penetration distances of both **TR3** and **TR70** in the 0% acrylic acid

hydrogels were considerably larger than the distance calculated for diffusion alone.[164] It is likely that there was some contribution from pressure-induced transport in these instances due to ζ-potential mismatch. Moreover, there was a significant transport contribution from electrophoresis in the case of **TR3**, in addition to the possibility for pressure involvement.

With a particular capillary tip size, the most direct method to control *Pe* and the ejection profile was to alter the applied electrical current or alter the ζ-potential of the medium being ejected into (which is not readily achievable for biological tissue). The fluorescence intensity at $\rho = 1$, corresponding to the maximal concentration of a molecule ejected just outside of the tip, and *Pe* were both linear functions of the applied current from 0.1 to 0.6 μA.[164] Increasing the current resulted in an approximately linear increase in the fluorescence intensity at $\rho = 1$, and concomitantly the concentration of ejected solute just outside the tip ($R^2 = 0.985$).[164] Moreover, there was a linear relationship between *Pe* and the applied current over the range of experimental currents ($R^2 = 0.988$).[164] This quantitative linear correlation has been previously described by Guy, though no other literature illustrated this relationship,[23, 151, 163, 164] likely due to capillary iontophoresis ejections not occurring at steady-state and instead at very short timescales.

The maximum concentration for molecules with a zero or positive electrophoretic mobility that is achievable just outside of the capillary tip is related to the concentration of the molecule within the ejection capillary, if a pressure does not develop as a result of ζ-potential mismatch and no difference exists between a molecule's velocity within the capillary and the outside medium. As these molecules are ejected, they are electrokinetically transported from the capillary tip or simply diffuse away.

In the case of ζ-potential mismatch, the development of a significant pressure just outside the capillary tip can produce further buildup of the molecule, which may even slightly exceed the

concentration inside the capillary. The pressure resulting from ζ-potential mismatch is also a function of the applied electrical current.[20] While it may still be possible to eject a molecule with a negative electrophoretic mobility from the capillary tip, its negative electrophoretic mobility may also slow its electrokinetic transport away from the capillary tip. In contrast, the solvent molecules may still undergo electroosmotic transport away from the tip. Thus, an even greater concentration of the molecule accumulates just outside of the capillary tip.

This can be semi-quantitatively compared with a ratio of the electrophoretic mobility to the electroosmotic mobility. The electroosmotic mobility of the ejected solvent is provided by the Helmholtz-Smoluchowski equation, and is equal to $-\varepsilon\zeta/\eta$.[20] For a borosilicate capillary with a ζ-potential of approximately -10 mV,[170-173] the electroosmotic mobility of the solvent was 7.8×10^{-9} m^2/Vs. Therefore, when the electrophoretic mobility of a solute is more negative than -7.8×10^{-9} m^2/Vs, as with **FL70**, the molecule will not be ejected from the capillary. For the sake of further illustration, consider a molecule with an electrophoretic mobility of -5×10^{-9} m^2/Vs. It will still be ejected from the borosilicate capillary; however, its negative electrophoretic mobility slows its electrokinetic transport away from the capillary tip, while the velocity of the solvent remains proportional to the electroosmotic mobility within the outside medium and the electric field.

In addition, a flux balance of a molecule through the capillary tip exists at steady-state. If the velocity in the hydrogel is less than the velocity in the capillary, then the concentration of a molecule within the gel must be higher than the concentration inside the capillary. For borosilicate capillaries ejecting into a hydrogel with no ζ-potential, the velocity outside of the capillary is a product of diffusion alone and is expected to be slower than the velocity inside the capillary. As such, the concentration of a molecule outside of the capillary is expected to exceed

the concentration within the capillary. However, in a hydrogel with a ζ-potential similar to brain tissue (i.e.: a ζ-potential of -22 to 25 mV), the electrokinetic velocity is expected to be greater than the velocity inside a borosilicate capillary (ζ-potential of approximately -10 mV).[170-173] For flux balance to exist in this situation, the concentration outside the capillary tip cannot exceed the concentration inside the capillary.

Ultimately, as currents are increased beyond the 0.6 μA that have been previously examined,[164] it is theoretically possible for the linear relationship between the applied current and the maximum fluorescence intensity outside the capillary tip to degenerate due to ζ-potential mismatch between the capillary and outside medium and with molecules of different electrophoretic mobilities. Flux balance also dictates the maximum concentration, and therefore the fluorescence, achievable outside of a capillary tip.

Furthermore, the dimensionless penetration distances where $I(\rho)/I_0$ was equal to 0.75, 0.50, and 0.25 were also correlated with the applied electrical current. As shown in Figure 3.7, increasing the applied current from 0.5 to 5.0 μA for **TR70** ejections into a -9.5 mV ζ-potential hydrogel resulted in a linear increase in the dimensionless penetration distances with R^2 greater than 0.99 in all instances. This same trend held for **TR3** ejections also, with analogous linear correlations having R^2 greater than 0.99. Therefore, it can be concluded that increasing the applied current not only increased *Pe* and the fluorescence intensity just outside of the capillary tip, but that it also increased the penetration distances achieved by a molecule. This is consistent with the hypothesis that the rate of electrokinetic transport outside of the capillary tip increases with higher applied currents, and may therefore transport a molecule over a further distance.

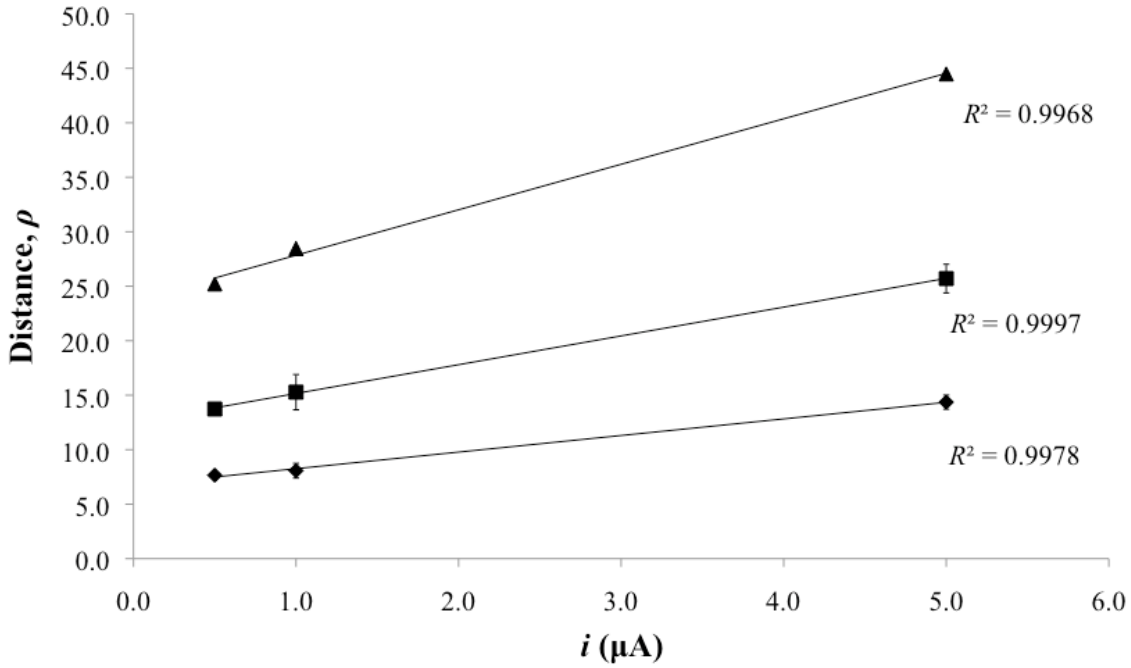

Figure 3.7. Impact of the current (i) on **TR70** ejection penetration distances (ρ) in a -9.5 mV ζ-potential hydrogel, where $I(\rho)/I_0$ equal to 0.75 (diamonds), 0.50 (squares), and 0.25 (triangles). Values are taken at 270 seconds.

If a molecule with zero electrophoretic mobility is assumed, as is roughly the case for **TR70**, its observed velocity is the electroosmotic velocity of the solvent. The electroosmotic velocity through the capillary tip may be calculated from the Helmholtz-Smoluchowski equation for each applied electrical current.[20] The value of ζ used in this calculation reflected the -10 mV ζ-potential of the borosilicate capillary.[170-173] The volumetric flow rate through the capillary tip is linearly related to the penetration distance in micrometers for **TR70** ejections, as shown in Figure 3.6 ($R^2 = 0.978$).

For a given porous matrix with a ζ-potential, the volumetric flow rate through the capillary tip was correlated with the average penetration distance in micrometers where $I(\rho)/I_0$ was equal to 0.25. For a given solution composition, the volumetric flow rate depends on the ζ-potential of the capillary, the electric field (and the applied electrical current), and the cross sectional area of the capillary tip. The y-intercept for the equation presented in Figure 3.6

indicates that even with no flow through the capillary tip, the average penetration distance in micrometers where $I(\rho)/I_0$ is equal to 0.25 still occurs at 62.6 μm. This can be rationalized in the following way: the penetration distance is also a function of the degree of electroosmotic flow developed in the matrix outside of the capillary tip and diffusion. With miniscule flow rates due to an extremely low applied electrical current, electroosmotic flow and diffusion still occur to some extent outside of the capillary tip resulting in a greater than expected penetration distance.

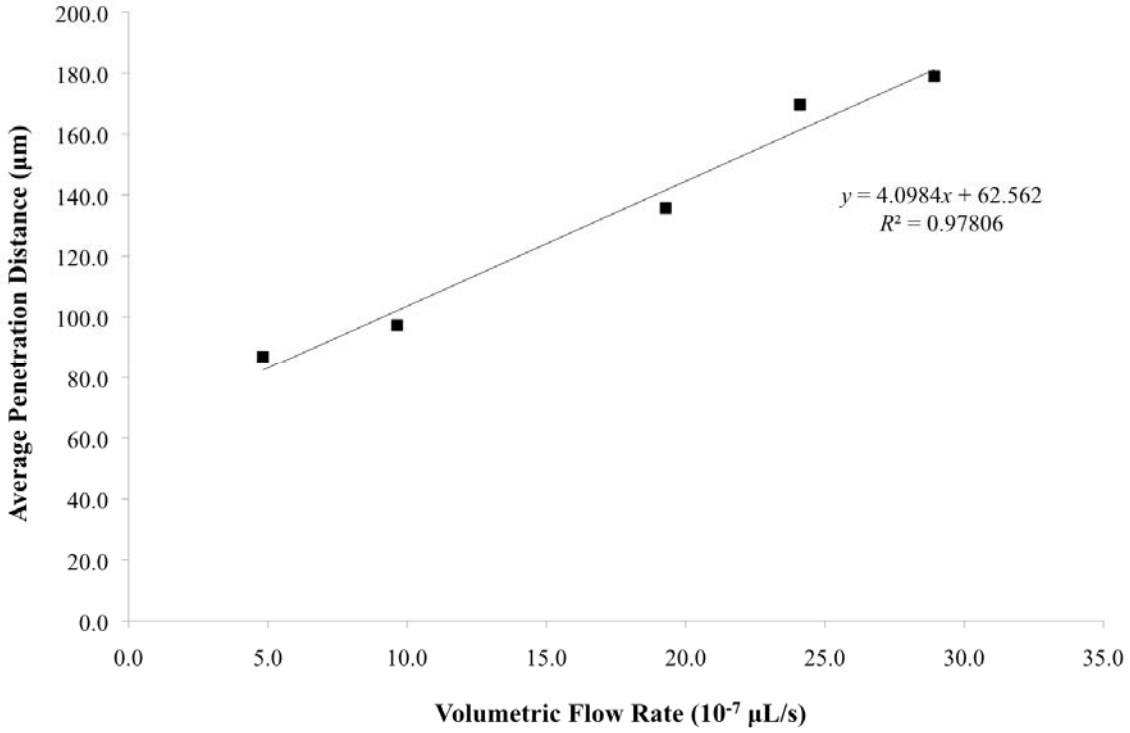

Figure 3.8. Relationship of the average penetration distance (μm) where $I(\rho)/I_0$ was equal to 0.25 with the volumetric flow rate through the capillary tip for ejections of **TR70** in a hydrogel with -24.7 mV ζ-potential with 0.1, 0.2, 0.4, 0.5, and 0.6 μA demonstrated a linear correlation with $R^2 = 0.978$.

Finally, it should be noted that with the extremely small capillary tips utilized in these experiments, with radii of ranging from roughly 1.5 to 2 μm, that fluorescent dextran conjugates may be transported over a relatively large distance. The penetration distance corresponding to $I(\rho)/I_0$ equal to 0.25 for the **TR70** dextran conjugate in the highest ζ-potential magnitude

hydrogel (the hydrogel with ζ-potential closest to OHSC) was approximately 90 μm. The analogous penetration distance for **TR3** was approximately 330 μm. The typical size of a pyramidal neuron soma in OHSC is roughly 20 μm,[90] thus the penetration distances achieved with this method describe more extended ejections that may impact a local region and several neurons. Furthermore, the penetration distance appeared to be correlated with molecular weight and the applied electrical current. In the case of **TR3**, it also has an appreciably positive electrophoretic mobility and experienced a lower tortuosity.

3.4.4 Ejections Into OHSC

The penetration distances for **TR70** ejections from a capillary tip positioned into CA1 of an OHSC with 0.5 μA were also determined.[164] Bright field imaging taken during the ejection demonstrated that the application of 0.5 μA of current created no visible distortion of the tissue. Moreover, 0.5 μA ejections into the CA1 of OHSC for up to 300 seconds demonstrated no increased cell death at the ejection site when compared to controls by propidium iodide staining.[164]

Steady-state iontophoretic ejections of **TR70** into the OHSC using 0.5 μA (r = 108.6 μm) traveled only two-thirds the distance, where $I(\rho)/I_0$ was equal to 0.25, than similar ejections of **TR70** into a -23.0 mV ζ-potential hydrogel using a 0.5 μA current (r = 164.5 μm).[164] Current was applied for the same amount of time in both cases. Why may a molecule travel a different distance in the OHSC than in a hydrogel with similar ζ-potential applied current? Perhaps the answer lies in understanding the tortuosity, current density, and electric field profile in the OHSC versus the hydrogel.

First, the current density and electric field profile are analyzed. The extracellular fluid content of the OHSC was initially determined to be roughly 20%,[28, 164] whereas the fluid content of the hydrogels ranged from approximately 96 to 98%. Thus, the electrical current experienced a more restricted path than in the OHSC than in the hydrogels, due to less fluid space, as it traveled through the extracellular space. As a result, the resistance to current flow was higher in the OHSC than in the hydrogels. Thus, Ohm's law dictates that the current is lower in the OHSC than in the hydrogels at a particular distance away from a specific electric field emanating from the capillary tip.[176] The magnitude of electrokinetic transport in the OHSC was therefore less than in the hydrogels for a given applied current and distance away from the capillary tip, though its overall ejection profile shape was very similar to those in hydrogels (fitting the experimental OHSC data to Equation 3.8 resulted in R^2 greater than 0.98).

The electric field and current density at the point where $I(\rho)/I_0$ was equal to 0.25 can be determined for a -24.7 ± 1.7 mV ζ-potential hydrogel and OHSC (ζ-potential of -22.8 ± 0.8 mV)[22] for an 0.5 μA applied current. The OHSC has an extracellular space free volume, α, of 20%,[28] and the 25% acrylic acid hydrogel has an α of approximately 98%. As the electrical current passes primarily through the fluid spaces, the electrical conductivity of the extracellular fluid (σ_f) – taken as GF-HBSS – can be multiplied by α for a given medium to arrive at an estimation for the conductivity for the medium (σ_m); thus, the σ_m for OHSC was estimated to be 0.32 S/m and σ_m for the hydrogel was estimated to be 1.59 S/m. The electric field at the tip (E_0) was calculated as the applied electrical current divided by σ_f. The electric field where $I(\rho)/I_0$ was equal to 0.25 multiplied by the capillary tip radius (thus the penetration distance, r, had SI units of distance), termed here as E_r, was determined by Equation 3.6. Finally, the current density at

the same distance, $J_i(r)$, was calculated by multiplying E_r by σ_m, with the results shown in Table 3.4.

Table 3.4. Determination of the current density, $J_i(r)$, at the point where $I(\rho)/I_0$ was equal to 0.25 away from the capillary tip (r) for **TR70** ejections in a hydrogel and OHSC.

	Current (μA)	E_0 **(V/m)**	E_r **(V/m)**	σ **(S/m)**	r **(10^{-6} m)**	$J_i(r)$ **(A/m^2)**
25% Hydrogel (α = 98%)	0.5	26,100	3.6	1.588	164.5	5.8
OHSC (α = 20%)	0.5	23,840	8.3	0.324	108.6	2.7
OHSC (α = 40%)	0.5	23,840	8.3	0.648	108.6	5.4
Note: Free volume is denoted as α.						

Table 3.4 shows that $J_i(r)$ for the OHSC was significantly different when α was assumed to be 20% or 40%, with the result from the 40% estimation providing a $J_i(r)$ that was similar to the hydrogel. This result can be analyzed in two ways: that the rate of electrokinetic transport depended on changes in free volume, which has previously been refuted,[174, 177] or that the free volume of the OHSC was not actually 20% (and in fact was closer to 40%). Furthermore, the free volume of the hippocampus was measured in acute hippocampal slices immersed in an artificial cerebrospinal fluid solution obtained from postnatal (p4 to p7) rats, and had an α of 0.41 ± 0.01 (N = 10).[178] This result was roughly twice as large as the free volumes determined in the adult rat hippocampus.[42, 43, 45]

Moreover $J_i(r)$ in the OHSC, assuming α equal to 40%, was similar to that of the hydrogel though the ultimate penetration distance was less (r = 108.6 μm, $J_i(r)$ = 5.4 A/m^2 and r = 164.5 μm, $J_i(r)$ = 5.8 A/m^2 respectively). Thus, r occurred when the current density was only 0.01% of its maximum at the capillary tip in both media for **TR70** ejections. At any particular distance from the capillary tip, the current density was higher in the hydrogel than in the OHSC.

At a specified distance of 108.6 μm from the capillary tip, the current density was calculated as 13.2 A/m^2 in the hydrogel and only 5.4 A/m^2 in the OHSC. Because the current density is lower in the OHSC compared to the hydrogel, electrokinetic transport occurs to a smaller degree at any given distance from the capillary tip.

Finally, electrokinetic transport of a molecule through the extracellular space of OHSC, hydrogels, or *in vivo* brain tissue must also account for differences in tortuosity. The tortuosity determined for **TR70** in the hydrogel and OHSC were 1.71 ± 0.18 and 2.24 ± 0.10 respectively.[22] In particular, the frictional drag force that exists in the OHSC and hydrogels may be strikingly different (see discussion in Chapter 1). The OHSC has a free volume that is less than half of that of a hydrogel, and it can be expected that a large, flexible 70 kDa molecule would experience a greater frictional drag force resulting in a decreased penetration distance.

3.5 CONCLUSIONS

Under the set of conditions for the experiments in this chapter, the transport of a molecule into a porous, aqueous medium strongly depended on the ζ-potential of the medium. Furthermore, a molecule's penetration distance was affected by properties of the solute (such as the electrophoretic mobility and molecular weight), the applied current, the flow rate through the capillary tip, and properties outside of the capillary tip, such as the medium's ζ-potential, its conductivity, and its tortuosity. Consequently, this methodology may be applied to living systems for molecular transport over distances of up to several hundred micrometers. The work developed in this chapter sets the foundation for the development of subsequent chapters,

whereby the penetration distances will be expanded to clinically relevant distances and this methodology will be elucidated *in vivo*.

3.6 ACKNOWLEDGEMENTS

This work was made possible by grant numbers UL1 RR024153 from the National Center for Research Resources (NCRR) and R01 GM044842 from the National Institute of General Medical Sciences, both components of the National Institutes of Health (NIH). This work was completed hand-in-hand with Yifat Guy. Capillary zone electrophoresis data was obtained by Aravinda Seneviratne in Timothy Strein's research group. Special thanks goes to Chuck Fleishaker and Tom Gasmire in the Department of Chemistry electronics and machine shops for their respective assistance in developing the electronics and setup required for these experiments.

4.0 LOCALIZED DELIVERY OF MOLECULES FOR THE TREATMENT OF MALIGNANT BRAIN GLIOMAS

4.1 MALIGNANT GLIOMAS

Malignant gliomas account for approximately 70% of new malignant primary brain tumor diagnoses each year in the United States.[179] Moreover, gliomas are associated with disproportionately high morbidity and mortality, with only a 12 to 15 month median survival for patients with glioblastomas and 2 to 5 years for patients with anaplastic gliomas, irrespective of treatment.[179] Gliomas represent a category of malignant primary brain tumors that originate from the supporting cells – oligodendrocytes and astrocytes – of the central nervous system. The tumors are histologically disparate and are classified into four prognostic grades: grade I (pilocytic astrocytoma), grade II (diffuse astrocytoma), grade III (anaplastic astrocytoma), and grade IV (glioblastoma). Grade III and IV tumors are considered as malignant gliomas.[179]

Malignant transformation in gliomas may be a ramification resulting from the accrual of genetic aberrations and de-regulation of cellular signaling pathways (particularly involved in cell division and growth factor signaling).[179-181] Several "molecular markers" for gliomas exist and are applied diagnostically. Primary glioblastomas generally manifest in patients older than 50 years of age, and are categorized by mutations and amplification of the epidermal growth factor receptor (EGFR), loss of heterozygosity of chromosome 10q, excision of the phosphatase and

tensin homologue on chromosome 10 (PTEN), and p16 deletion.[179, 181, 182] In contrast, secondary glioblastomas occur in younger patients as low-grade or anaplastic astrocytomas, and transform over a period of several years into higher-grade tumors or glioblastomas. They are characterized by mutations in the p53 tumor suppressor gene, increased expression of the platelet-derived growth factor receptor (PDGFR), loss of heterozygosity of chromosome 10q, and aberrations in the p16 and retinoblastoma (Rb) pathways.[179, 181-183] Moreover, these two types may be distinguished by differences in transcriptional patterns and irregular DNA copy numbers.[180]

4.2 CURRENT THERAPEUTIC STRATEGIES FOR GLIOMAS

The current standard therapy for newly diagnosed malignant gliomas involves surgical resection when feasible, radiotherapy, and chemotherapy.[179, 184] This multimodal treatment strategy is a result of the infiltrative nature of gliomas. As a result, complete surgical resection is not possible, and adjuvant therapy is required. The addition of radiotherapy – 60 Gy of external beam irradiation delivered 5 days per week in fractions of 1.8 to 2.0 Gy as a convention – to surgery increases survival amongst patients from a range of 3 to 4 months to a range of 7 to 12 months.[179, 185, 186] However, even with this standardized therapy, 90% of the tumors recur within 2 centimeters of the original site.[186] A 2005 phase III trial with comparing the aforementioned radiotherapy alone to radiotherapy plus temozolomide, an oral DNA alkylating chemotherapy agent, demonstrated an acceptable side-effect profile and, as compared with radiotherapy alone, increased median survival from 12.1 months to 14.6 months.[184] Moreover, the survival rate at two years amongst the patients who received radiation and temozolomide was 26.5%, and was significantly greater than the 10.4% survival rate amongst patients receiving radiation alone.[184]

This landmark clinical trial established a new standard of care known as the Stupp regimen,[184] utilizing radiation with concomitant and adjuvant temozolomide for newly diagnosed glioblastomas. However, tumor recurrence still remains a significant issue despite this therapy, with more than 72% of tumor recurrence within the radiotherapy field and tumor resection margins.[187] Moreover, the therapeutic window for temozolomide dosage is narrowed because of its systemic administration and resultant myelotoxicity.[188]

Prior to the establishment of this new standard of care, investigators took note of this predilection for local recurrence of glioblastoma. Two primary strategies for the localized delivery of chemotherapy were developed – implantable polymeric wafers and pressure-driven infusion. Despite the advent of the Stupp regimen, significant ongoing research seeks to understand and apply these two strategies to clinical patient care. These two methods circumvent systemic toxicities, and instead administer chemotherapy to a localized area within the brain itself.

4.3 DIFFUSION-BASED BIODEGRADABLE WAFERS

Biodegradable polymer wafers (Gliadel® wafers) containing carmustine were approved by the FDA in 1999 and implanted into the tumor bed following resection, with a gradual diffusion-based release of carmustine to affect residual localized tumor cells.[189] In a randomized, placebo-controlled phase III trial in newly diagnosed malignant gliomas, the median survival in treated patients increased from 11.6 months to 13.9 months with this survival advantage maintained at 2 and 3 years.[190, 191] Diffusion is the motivating force behind chemotherapy penetration into the brain tissue with this technique. Pharmacokinetic and distribution studies in non-human primates

have determined that Gliadel® releases carmustine over a 5 day period when in complete contact with interstitial fluid, with biodegradation of the wafers occurring over a period of 6 to 8 weeks.[192] Animal and computational studies have demonstrated millimolar concentration dose-delivery within millimeters of the wafer, with limited spread of carmustine at further distances.[192] However, a study in non-human primates demonstrated significant convective flow due to postsurgical edema that augmented the diffusion of carmustine with the drug being detected over a centimeter away for up to a week following wafer implantation.[193]

Because wafer implantation requires an invasive craniotomy and tumor resection, there are limited opportunities for placement. A large clinical trial reported a greater occurrence of cerebrospinal fluid leak and intracranial hypertension in patients who received Gliadel® versus placebo (5% versus 0.8% and 9.2% versus 1.7% respectively), which may result in reoperation or ventricular drain placement.[190] Moreover, malignant gliomas typically develop deep within the subcortical white matter and periventricular zones, and may not be amenable to resection (and thus Gliadel® implantation).[179] Finally, Gliadel® (carmustine) may preclude patients from entering some ongoing clinical trials with newly developed chemotherapy agents.

4.4 CONVECTION-ENHANCED DELIVERY UTILIZING PRESSURE

Pressure-driven infusion of molecules was first described in 1994 to introduce locally high concentrations of macromolecules and small molecules into the brains of cats.[194] In this initial study, the volume of distribution to volume of infusion (V_d / V_i) ratios were 6:1 and 13:1 for a radiolabeled transferrin macromolecule and radiolabeled sucrose molecule respectively.[194] The V_d / V_i ratio describes the difference between the volume of infusate introduced into the brain

relative to its ultimate distribution at a particular timepoint. The infusates were introduced over 1 to 4 hours with flow rates that were gradually increased from 0.5 to 4 μL/min. Quick calculation yields that these parameters result in a range of infusion volumes of approximately 30 μL (0.5 μL/min for 60 min) to 960 μL (4 μL/min for 240 min). Immediately after perfusion, transferrin dispersed approximately 1.5 cm and sucrose dispersed approximately 2.0 cm in the anterior-posterior plane, though this infusion was predominately within the white matter (less dense, more free volume) with partition into the gray matter (more dense, less free volume) occurring much later.[194] The authors termed the pressure-driven infusion of molecules "convection-enhanced delivery," as the distribution volume observed was greater than could occur by diffusion alone in the same time frame.

This pressure-driven infusion was extensively evaluated over the subsequent ~17 years until present day. In a rat model, the effects of varying the rate of infusion, cannula size, concentration of the infusate, and pre-infusion sealing time to allow tissue accommodation of the infusion cannula were evaluated.[195] Only the rate of infusion and cannula size significantly altered the convective distribution of the infused molecule. Of note, the authors described significant backflow and infusate leak along the implanted cannula tract, which resolved at infusion rates less than 1 μL/min. Percentage of leak and backflow observed at 1 and 5 μL/min were 22.7 ± 11.7% and 30.3 ± 7.8% respectively (mean ± standard deviation).[195] Clearly, backflow represents a significant obstacle with pressure-driven delivery despite refinement of the cannula tip,[196-200] which limits the rate of infusion and subsequent volume of drug distribution. It should be noted that at very low infusion volumes ranging from 80 to 120 μL, no neurological deficit or tissue deformation was observed in non-human primates.[201] However, subcortical infusion in a canine glioma model demonstrated significant ventricular compression due to mass

effect.[202] The infusion volume that caused complete ventricular occlusion was determined to be 407 ± 59 μL in dogs and 672 ± 52 μL in non-human primates.[202] The authors of this study commented that ventricular compression in humans would be a serious complication requiring immediate neurosurgical intervention.

Over the previous decade, more than 17 clinical trials have examined the efficacy and safety profile of "convection-enhanced delivery" in human patients. In one of the first clinical trials to release safety data that included 22 human patients with glioblastoma, 59% of the adverse effects related to catheter placement and infusion were neurological or psychiatric with 9% due to infection; the most common adverse effects included headache, gait disturbance, and fever.[203] In other human clinical trials, pressure-driven infusion into brain tumors resulted in seizure activity and hemiparesis from peritumoral edema and mass effect.[204, 205] Several animal models and small human clinical trials demonstrated that the infusion volumes and infusion rates were limited by deep tissue deformation, separation of white matter tracts, and tearing, leakage of the infusate into the cerebrospinal fluid spaces or prior resection beds/catheter tracts as they represent areas of least pressure resistance, and resultantly unpredictable intraparenchymal drug delivery.[195, 202, 203, 205-210] Additional limitations became increasingly evident in a large human clinical trial, the PRECISE trial.[211]

In the PRECISE trial (296 patients with glioblastoma), variability of placement of the infusion catheter was significant despite rigorous training and protocol development with only 49.8% of catheters placed appropriately.[211, 212] Catheter placement had significant effect on progression-free survival with recurrent glioblastoma.[211, 212] Moreover, coverage of relevant target areas was low, with only 20.1% of the 2 cm penumbra surrounding the resection cavity covered by the infusate on average.[211, 212] As expected, delivery to target areas correlated with

catheter placement and progression-free survival.[211, 212] The results for this clinical trial were somewhat discouraging, as a major limitation involved placement of the infusion catheter and the subsequent directionality of flow from the catheter tip.

To sum up pressure-driven infusion ("convection-enhanced delivery"), an infused drug is able to penetrate a much further distance than by diffusion alone (such as with Gliadel® wafers). However, infusion under constant pressure may produce transient deformation of brain tissue, potential tissue tearing and leakage of the infusate into prior resection beds/catheter tracts or the cerebrospinal fluid spaces or the brain, ineffective and unpredictable infusion profiles due to catheter placement and backflow up along the catheter itself, and an inability to reliably direct the infusion to the target site. Just as Gliadel® wafers are more suited for cortical or surface lesions, pressure-driven infusion is more suitable for deeper lesions, as attempts to infuse superficial brain areas result in spreading of the infusate across the cortical surface.

The following chapter describes the development, preliminary optimization, and *in vivo* proof-of-principle for an electroosmotic convection-enhanced delivery system that may address many of the limitations observed with pressure-driven infusion.

5.0 LARGE-DISTANCE ELECTROKINETIC INFUSION OF MACROMOLECULES AND SMALL MOLECULES IN A GEL MODEL, ORGANOTYPIC HIPPOCAMPAL SLICE CULTURES, AND IN VIVO

5.1 INTRODUCTION

Building upon the experiments conducted previously[164] and in Chapter 3, whereby macromolecules and small molecules were transported over distances up to a few hundred micrometers from the capillary tip, this chapter seeks to address the clinical limitations encountered by pressure-driven convection-enhanced delivery for the treatment of malignant gliomas.[195, 202, 203, 205-212] This methodology examines drug infusion and penetration over a significantly greater distance than is achievable by diffusion alone (such as with Gliadel® wafers).[189-192] Moreover, infusion under constant pressure may generate a transient deformation of the brain tissue with temporary (or possibly permanent) neurological deficit.[204, 205] Furthermore, the potential exists for tissue tearing and leakage of the infusate into prior resection beds or catheter tracts or even the cerebrospinal fluid spaces or the brain.[211, 212] Clinical trials for pressure-driven delivery were limited by ineffective and unpredictable infusion profiles as a result of improper catheter placement and backflow along the catheter itself.[211, 212] Finally, pressure-driven delivery demonstrated an inability to reliably direct the infusate towards a target

site, and is similarly not feasible for transcortical perfusions of drugs over wide surface areas.[211, 212]

Previous experiments with small-scale, localized perfusions demonstrated that the transport of a molecule into a porous, aqueous medium depends on the properties of the solute (such as its electrophoretic mobility and molecular weight and size), the ionic strength of the fluid used during the infusion,[164] the applied electrical current, and properties outside of the capillary tip, such as the medium's ζ-potential and tortuosity. A mathematical description of the ejection of a molecule was derived to explain the Peclet number, *Pe*, which indicates the relative contribution of convection-enhanced delivery versus diffusion alone.[164] The distance scale for these previous experiments ranged from only a few micrometers to several hundred micrometers, and moreover these experiments were performed in homogenous hydrogel matrices or OHSC.[164] These penetration distances are not clinically relevant for the treatment of malignant gliomas; penetration distances on the order of millimeters (and most desirably, centimeters) are needed to achieve infusions with relevant volumes of distribution.[186, 187]

The brain is a heterogeneous organ composed of not only several cell types, but also of varying regional architecture. From a simplistic viewpoint, the brain is divided into three primary regions – the cerebrum, cerebellum, and brainstem – which are further segmented based on function, histological appearance, and vascular distributions.[213] For instance, the folded outer 2 to 5 mm of the cerebrum contains the soma of roughly 10^{10} interconnected neurons, termed the cortex or gray matter.[213] Just below the gray matter lies the white matter, comprised of the downward axonal projections of these neurons, which terminate in the thalamus, spinal cord, or other brain stem nuclei. Most malignant gliomas arise deep within this white matter near the natural cerebrospinal fluid-portions of the brain, termed ventricles.[179] Located adjacent to the

ventricles are a myriad of other bilateral structures – the thalami, hypothalami, basal ganglia, hippocampi, and the white matter tracts which give rise to the cerebral peduncles. Each of these structures has different densities, arrangements of soma or axons, and ultimately may result in variable transport of a molecule due to heterogeneous tissue permeabilities.[213] As such, *in vivo* infusions of wide areas are necessary to evaluate transport over a range of tissue architectures and subregions.

While capillary tips with radius of approximately 2 μm were used in the short-distance perfusions in Chapter 3, this chapter utilized fused silica capillaries with a more negative ζ-potential and larger tips with radii of 25 and 50 μm.[170, 173, 214, 215] The ζ-potential of fused silica capillaries induce greater electroosmosis at a given electric field when compared to the borosilicate capillaries with a lower magnitude ζ-potential. Furthermore, a range of applied electrical currents was examined to deliver reproducible long-distance infusions of a small, cationic molecule – $Ru(bpy)_3^{2+}$. This molecule was previously used for short-distance infusions due to its substantial and positive electrophoretic mobility and small size.[164] This methodology was further developed to rapidly deliver a molecule to large surface areas from a hydrogel doped with a molecule of interest. Control of directional transport was also achieved from capillary tips over distances ranging from several hundred micrometers to more than one millimeter. Finally, this work culminated in an *in vivo* proof-of-principle in the adult rat brain, in an experiment designed to evaluate the volume of distributions attained by electrokinetic infusion.

5.2 EXPERIMENTAL

5.2.1 Chemicals and Solutions

Unless otherwise noted, the following materials were purchased from Sigma (St. Louis, MO) and used as received. Solutions were prepared with Millipore Synthesis A10 system 18 MΩ purified water (Millipore, Billerica, MA). Glucose-free HEPES-buffered salt solution (GF-HBSS) contained in mM: 143.4 NaCl, 5 HEPES, 5.4 KCl, 1.2 $MgSO_4$, 1.2 NaH_2PO_4, and 2.0 $CaCl_2$. GF-HBSS was filtered, stored frozen, warmed to room temperature, and ultrasonicated for ten minutes before use. HBSS contained the same quantities as GF-HBSS with an additional 10 mM *D*-(+)-glucose and underwent the same preparation and storage process. GBSS was made up of 27.5 mM *D*-(+)-glucose and filtered 2.7 mM $MgSO_4$ supplemented Gey's Balanced Salt solution. GBSS was stored in the refrigerator and warmed to 37 °C before use. Culture medium contained the following from Gibco (Invitrogen, Eugene, OR): 50 % Opti-MEM, 25 % heat-inactivated Horse Serum, and 25 % Hanks' Balanced Salt Solution, supplemented with 2 % B-27 vitamin and 1 % *D*-(+)-glucose from Sigma.[169] Medium was filtered, refrigerated for storage, and warmed to 37 °C before use. Texas Red dextran conjugate 70 kDa (**TR70**), Texas Red dextran conjugate 3 kDa (**TR3**), and boron-dipyrromethene dextran conjugate 10 kDa (**BODIPY10**) were obtained from Invitrogen. A 0.10 mM solution of **TR70** and **BODIPY10** was made in GF-HBSS, filtered, and frozen until use. Tris(2,2'-bipyridine)ruthenium (abbreviated $Ru(bpy)_3^{2+}$) from Sigma was diluted to 45 mM in GF-HBSS. The free diffusion coefficients and electrophoretic mobilities were determined as described in Chapters 2 and 3.

5.2.2 Synthesis and Characterization of Hydrogels

A 25% weight/weight acrylic acid poly(acrylamide-*co*-acrylic acid) hydrogel was prepared with the purpose of creating a matrix with a similar ζ-potential to brain tissue by a thermally-initiated radical polymerization reaction, as described in Chapter 2. It was subsequently characterized and the ζ-potential, tortuosity, porosity, and conductivity were determined, as described in Chapters 2 and 3.

5.2.3 Organotypic Hippocampal Slice Cultures (OHSC)

The organotypic hippocampal slice culture (OHSC) method, developed by Stoppini *et al.,*[92] was used with slight variations. The following procedures were approved by the University of Pittsburgh Institutional Animal Care and Use Committee. Bilateral dissections of the hippocampi were done on 9-day postnatal Sprague-Dawley albino rats. The hippocampi were chopped along the transverse axis to 400 μm thick slices using a McIlwain tissue chopper (Mickle Laboratory Engineering, Surrey, England). The slices were placed on 0.4 μm PTFE insert membranes (Millipore, Bedford, MA) and incubated over 1.2 mL of medium at 36.5 °C in 5 % CO_2/ 95 % air for 6 to 8 days. Culture medium was exchanged every 2 to 3 days. Prior to experiments, culture medium was replaced with 37 °C GBSS and incubated for thirty minutes. A second GBSS exchange followed for another incubation period of 30 minutes. A last exchange to 37 °C HBSS and incubation for 30 minutes was done prior to experimental use.

5.2.4 Electrokinetic Infusions into Hydrogels

Fused silica capillaries of two types: (1) 50.0 ± 0.1 μm inner diameter, 358.5 ± 1.5 μm outer diameter, length 10 cm and (2) 99.5 ± 0.2 μm inner diameter, 361.1 ± 0.7 μm outer diameter, length 10 cm (Polymicro Technologies, Phoenix, AZ) were cleanly cut to a blunt tip with the same dimensions. The capillary was filled with the 45 mM $Ru(bpy)_3^{2+}$ solution. The PVC cell, as described in section 3.3.9, was secured on an Olympus IX-81 inverted fluorescence microscope stage and imaged with a high-resolution charged-coupled device camera (ORCA-ER).

A 25% acrylic acid poly(acrylamide-*co*-acrylic acid) hydrogel section was cut to size and carefully placed in the cell. Careful attention was made to ensure complete hydrogel contact with the exposed cover slip. The fused silica capillary was carefully threaded through one side of the channel and into the hydrogel. The distal end of the fused silica capillary was immersed in a vial containing GF-HBSS and a Ag working electrode. Additionally, a Ag wire ground electrode (0.3 mm diameter) was threaded through the other side of the cell and was inserted into the hydrogel, so that the distance between the capillary tip and the ground electrode was always more than 5 mm. The current source was a Princeton Applied Research 173 potentiostat (PAR) (Princeton, NJ). The circuitry was described previously.[164] Image sequences were acquired using MetaMorph 7.6.2.0 software (MDS Analytical Technologies, Sunnyvale, CA) using an UPlan Fl 4× Olympus objective lens. MetaMorph software triggered the onset and cessation of current during image acquisition. The potential across the system was monitored by the PAR potentiostat. Currents ran for up to 40 minutes, ranging from 0.2 to 1.5 μA. These experiments were conducted for both the ~50 μm and the ~100 μm diameter unpulled capillaries.

Image sequences were analyzed by drawing a line scan from approximately the center of the capillary tip to the end of the field of view on the same axis as the capillary lumen. Intensity data were recorded along the line scan before the initiation of current (background intensity), and at 30 seconds intervals after the current was applied. Background intensity was subtracted from line scan intensities. Reported intensity values are between 0 and 4,095. Values of I_0 (maximum fluorescence intensity), I_1, and *Pe* were determined by nonlinear fitting of Equation 5.1, similar as in Chapter 3, to data with Mathcad 14 (PTC, Needham, MA). I_1 is included to correct for baseline intensity. The penetration distance in SI units of distance, *r*, was obtained by multiplying ρ by the capillary tip radius.

$$I(\rho) = I_0\left(\frac{1-e^{-Pe/\rho}}{1-e^{-Pe}}\right) + I_1 \qquad 5.1$$

5.2.5 Infusions of a Small, Cationic Solute into OHSC

Fused silica capillaries (99.5 ± 0.2 μm inner diameter, 361.1 ± 0.7 μm outer diameter, length 10 cm) (Polymicro Technologies, Phoenix, AZ) were cleanly cut to a blunt tip with the same diameter dimensions. The unpulled infusion capillary was filled with the 45 mM $Ru(bpy)_3^{2+}$ solution. Experiments in the OHSC were secured on an Olympus IX-81 inverted fluorescence microscope stage and imaged with a high-resolution charged-coupled device camera (ORCA-ER), with the setup described by Figure 5.1. An insert membrane with an OHSC was placed in a glass dish without GF-HBSS underneath the insert membrane, so that the current path would travel through the OHSC. The infusion capillary was positioned at a 90° angle relative to the plane of the OHSC using a manipulator arm on a Narishige NMN-21

micromanipulator (Tokyo, Japan). The tip was inserted onto the CA1 region of the OHSC. The distal end of the fused silica capillary was immersed in a vial containing GF-HBSS and a Ag working electrode. The counter Ag electrode was guided into the CA3 region of the OHSC by a second manipulator arm on a Narishige NMN-21 micromanipulator (Tokyo, Japan). The electrode circuitry was also the same as the hydrogel experiment.[164] The current source was the Princeton Applied Research 173 potentiostat (PAR) (Princeton, NJ). Image sequences were acquired using MetaMorph 7.6.2.0 software (MDS Analytical Technologies, Sunnyvale, CA) using an UPlan Fl 4× Olympus objective lens. MetaMorph software triggered the onset and cessation of current during image acquisition. The potential across the system was monitored by the PAR potentiostat. A 1.0 μA current was applied for up to 15 minutes with longer times causing dryness of the tissue.

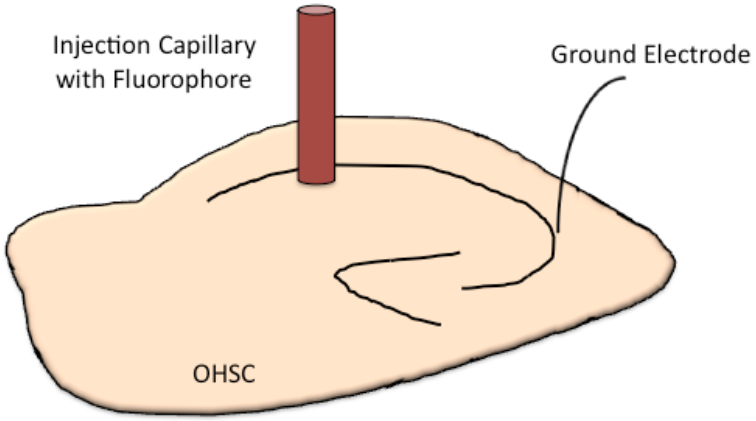

Figure 5.1. Setup for ejections of $Ru(bpy)_3^{2+}$ into OHSC with 1.0 μA applied current. The infusion capillary is filled with $Ru(bpy)_3^{2+}$ and placed in the CA1 at a 20° angle from the OHSC plane, while the counter electrode was inserted into CA3.

In a separate experiment, the OHSC and insert membrane were placed in a glass dish containing GF-HBSS, filled so that the fluid level made contact with the underside of the insert membrane. This fluid contact with the insert membrane introduced an alternate current path, so

that it was no longer directed through the OHSC and instead downward through the insert membrane. All other experimental constraints, including the current, experiment time, and imaging parameters remained the same.

5.2.6 Dual-Capillary Infusions into OHSC

Fused silica capillaries (99.5 ± 0.2 μm inner diameter, 361.1 ± 0.7 μm outer diameter, length 10 cm) (Polymicro Technologies, Phoenix, AZ) were cleanly cut to a blunt tip with the same diameter dimensions or pulled using the Sutter P-2000 capillary puller to tips of 20 μm inner diameter. Tip size and shape were measured using an Olympus BX41 optical microscope. The pulled capillary (termed the infusion capillary) was filled with a 0.32 mM **TR70** solution in GF-HBSS. The unpulled capillary (termed the counter capillary) was filled with GF-HBSS. The distal end of each capillary was placed into a vial containing GF-HBSS and an Ag electrode. The vial containing the infusion capillary contained the working Ag electrode, while the vial containing only the GF-HBSS contained the ground Ag electrode.

Experiments in the OHSC were setup as described by Figure 5.2. An insert membrane with an OHSC was placed in a glass dish. The infusion capillary filled with **TR70** was positioned at a 20° angle from the plane of the OHSC using a manipulator arm on a Narishige NMN-21 micromanipulator (Tokyo, Japan). The pulled capillary tip was inserted adjacent to the dentate gyrus of the OHSC. The counter capillary was positioned at a 90° angle from the plane of the OHSC using a second manipulator arm on a Narishige NMN-21 micromanipulator (Tokyo, Japan). The unpulled counter capillary was inserted near the interface of CA1 and CA3 of the OHSC, so that the distance between the two capillaries was approximately 350 μm.

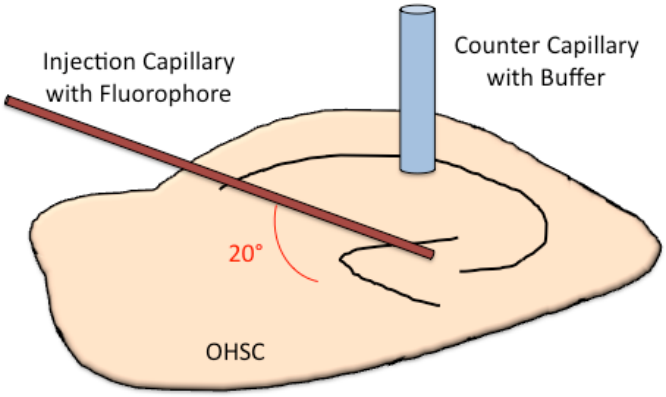

Figure 5.2. Dual-capillary ejection of **TR70** into OHSC with 0.3 μA applied current. The infusion capillary is filled with **TR70** and placed adjacent to the dentate gyrus at a 20° angle from the OHSC plane, while the counter capillary was filled with GF-HBSS and positioned between CA3 and CA1 at a 90° angle from the OHSC plane.

The current source was a Princeton Applied Research 173 potentiostat (PAR) (Princeton, NJ), attached to the secured electrodes as described previously.[164] The entire setup was positioned in a glass dish over the objective lens of an Olympus IX-81 inverted fluorescence microscope. Image sequences were acquired using MetaMorph 7.6.2.0 software (MDS Analytical Technologies, Sunnyvale, CA) using an UPlan Fl 4× Olympus objective lens. MetaMorph software triggered the onset and cessation of current during image acquisition. The potential across the system was monitored by the PAR potentiostat. A 0.3 μA current was applied for 20 minutes.

5.2.7 Doped Hydrogel Infusions into OHSC

A 25% acrylic acid poly(acrylamide-*co*-acrylic acid) hydrogel was placed in a solution of 0.5 mM **TR3** in GF-HBSS, and allowed to equilibrate overnight. The doped hydrogel was removed from the solution and cut to a size of 3 mm × 3 mm at the base × 2 mm high. The hydrogel was placed over the subiculum and entorhinal cortex portions of an OHSC on its culture insert membrane. A second 25% acrylic acid poly(acrylamide-*co*-acrylic acid) hydrogel

that did not contain fluorophore (only GF-HBSS) was placed over the opposite border of the OHSC, just adjacent to the CA3 region. The distance between the doped and counter hydrogels was 1.5 mm. Two Ag wires with 0.3 mm diameter were each placed into the hydrogels. The Digital Midgard™ Precision Current Source iontophoretic pump (Stoelting Co., Wood Dale, IL) was used as the current source, attached to the secured electrodes as described previously.[164] The entire setup was positioned in a glass dish over the objective lens of an Olympus IX-81 inverted fluorescence microscope. No buffer solution was below the OHSC and insert membrane, again to direct the current flow through the OHSC. This setup is shown in Figure 5.3.

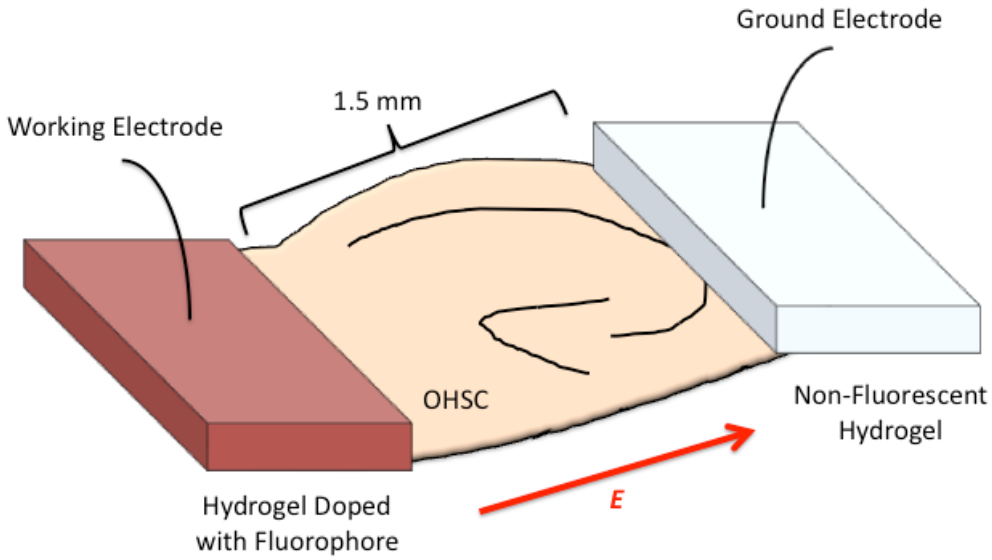

Figure 5.3. Experimental setup for the doped hydrogel perfusion of **TR3** through OHSC with 10.0 μA applied current, viewed from the side. Two hydrogels are spaced by 1.5 mm over the OHSC. In the control experiment, the counter electrode is not placed into the hydrogel, and is instead placed remotely.

Image sequences were acquired using MetaMorph 7.6.2.0 software (MDS Analytical Technologies, Sunnyvale, CA) using an UPlan Fl 4× Olympus objective lens. **TR3** was imaged using a 560/25 excitation filter, a 625/26 emission filter, both obtained from Olympus, and the Semrock triple-band dichroic mirror described earlier, with intensity values between 0 and 4,095.

An image was acquired every 30 seconds. MetaMorph software triggered the onset and cessation of current during image acquisition. The potential across the system was monitored by the Midgard^{TM} pump. A 10.0 μA current was applied for 12 minutes. However, after 10 minutes, the insert membrane began to dry out and the imaging was obscured. As a result, the data is presented up to 10 minutes.

In a separate experiment, the OHSC and insert membrane were placed in a glass dish containing GF-HBSS, filled so that the fluid level made contact with the underside of the insert membrane. The fluid contact with the insert membrane introduced an alternate current path, so that it was no longer directed through the tissue and instead downward through the insert membrane. The working and counter electrodes were still placed in the doped and counter hydrogels respectively. All other experimental constraints, including the current, experiment time, and imaging parameters remained the same.

5.2.8 Electrokinetic Infusions *In Vivo*

The following procedures were approved by the University of Pittsburgh Institutional Animal Care and Use Committee. Male Sprague-Dawley rats (Hilltop, Scottsdale, PA), with weights ranging from 260 to 290 g, were anesthetized with isoflurane, and wrapped in a 37 °C homoeothermic blanket (EKEG Electronics, Vancouver, BC, Canada). An incisor bar was set at 0 mm at the interaural line. Rats underwent aseptic stereotactic surgery, whereby bilateral craniotomies were made to position an infusion capillary and counter capillary into the thalami bilaterally (from bregma: 4.0 mm lateral, 1.3 mm posterior, and 5.0 mm below the dura) for volumetric analysis. The capillaries were also implanted into the hippocampi bilaterally (from bregma: 4.0 mm lateral, 1.3 mm posterior, and 2.5 mm below the dura).

Fused silica capillaries (99.5 ± 0.2 μm inner diameter, 361.1 ± 0.7 μm outer diameter, length 15 cm) (Polymicro Technologies, Phoenix, AZ) were cleanly cut to a blunt tip with the same diameter dimensions, and were used as the two implanted capillaries. The infusion capillary was filled with the fluorophore solution of interest: a 45 mM solution of $Ru(bpy)_3^{2+}$ in GF-HBSS or a co-solution of 0.1 mM **TR70** and 0.1 mM **BODIPY10** in GF-HBSS were used. The counter capillary was filled with GF-HBSS. The distal ends of the fused silica capillaries were immersed into a vial containing the same fluorophore solution or GF-HBSS for the infusion and counter capillaries respectively. Ag wire electrodes were inserted into each of these vials and connected to the Digital Midgard™ Precision Current Source iontophoretic pump (Stoelting Co., Wood Dale, IL). A current of 25.0 μA was applied for 45 minutes. For experiments that evaluated diffusional transport, the same setup was used but no current was applied.

After the electrokinetic infusion period, the rats underwent rapid transcardial perfusion with 250 mL of 8% cold paraformaldehyde in PBS. The brain was immediately isolated, sectioned into 4 mm coronal slices, and then further sectioned on a vibratome into 300 μm thick coronal slices. Vibratome sectioning was quantitative, with no discarded tissue between slices with a visible fluorophore spot. The time required for the transcardial perfusion and vibratome sectioning was less than 30 minutes, while the transcardial perfusion itself was completed in less than 5 minutes. The 300 μm thick coronal slices were mounted onto glass slides and imaged with the Olympus IX-81 inverted fluorescence microscope. Image sequences were acquired using MetaMorph 7.6.2.0 software (MDS Analytical Technologies, Sunnyvale, CA) using a PlanApo 1.25× Olympus objective lens and Olympus filters. **TR70** was imaged using a 555/25 excitation filter and a 605/52 emission filter. **BODIPY10** was imaged using a 490/20 excitation filter and a 525/36 emission filter. $Ru(bpy)_3^{2+}$ was imaged using a 460-490 excitation filter and a 605/52

emission filter. The fluorescence intensity values were between 0 and 4,095. Slices were cryo-protected and stored at -20 °C until further use.

The volumes of distribution from the infusions were determined by evaluating the fluorescence intensities amongst the coronal tissue slices. The overall maximum fluorescence intensity (I_0) at the infusion capillary implantation site was determined for each rat. The distance along eight radii was measured from a central point of maximum fluorescence intensity (in that slice) to the point where the fluorescence intensity was 25% of I_0. The eight radii were averaged together to arrive at a radius to determine the area of tissue impacted by the infusions, assuming a circular area. The coronal area within each slice was multiplied by the thickness of the slice to arrive at a volume per tissue slice. The volumes of each slice were summed to arrive at a final volume of distribution for each rat and fluorophore.

5.3 RESULTS AND DISCUSSION

5.3.1 Effect of Capillary Tip Size and Current on Infusions

Using fused silica capillaries and the poly(acrylamide-*co*-acrylic acid) hydrogel model for brain tissue, the effect of capillary tip diameter on the infusion profile and penetration distance was evaluated. The capillary tip diameters evaluated were approximately 50 and 100 μm. A small dicationic fluorescent molecule ($Ru(bpy)_3^{2+}$, MW 570) was infused from each capillary for up to 40 minutes, with results shown in Figure 5.4. As expected, further penetration distances were achieved in comparison to the roughly 4 μm diameter tips employed in Chapter 3, with the penetration distance where the fluorescence intensity was 25% of I_0 occurring at 4,516 ±

112 μm (N = 5) away from the 100 μm diameter capillary tip and at 1,489 ± 27 μm (N = 5) away from the 50 μm diameter capillary tip, both at 1.0 μA (data are presented as means ± SEM). There was only an approximately 2% error in the penetration distances, indicating the highly reproducible nature of the infusion profile. In comparison to the work presented in Chapter 3, the dimensionless distance, ρ, was no longer needed to normalize penetration distances for variations in capillary tip size because the 50 and 100 μm diameter tips were unpulled, cut to a blunt tip, and were reproducible size. As such, the penetration distance data in Figure 5.4 is presented in SI units of micrometers.

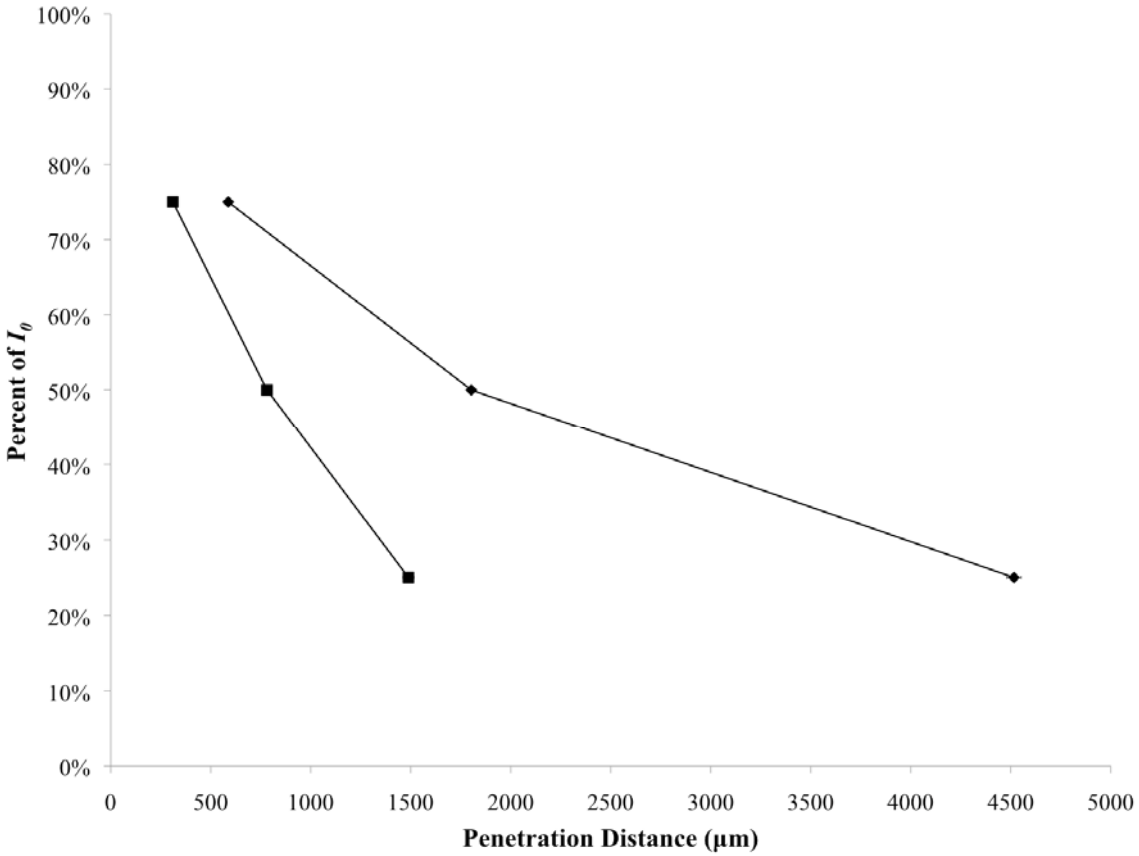

Figure 5.4. Effect of capillary tip size on penetration distance (μm) from 1 μA infusions for 40 min of $Ru(bpy)_3^{2+}$ in a hydrogel with -24.7 mV ζ-potential: square, 50 μm diameter tip (N = 5), diamond, 100 μm diameter tip (N = 5).

The expression for the diffusional concentration distribution (directly related to the fluorescence intensity profile) of a molecule at steady-state is provided by Equation 5.2, where r is the distance from the hemispherical source and a is the radius of the hemispherical source.[168]

$$C(r) = C(a)\frac{a}{r} \qquad 5.2$$

It is noteworthy that the diffusion coefficient does not influence the ultimate distribution of a molecule, rather only the time needed to reach steady-state. Since the fluorescence intensity is directly related to the concentration of the fluorophore, 25% of I_0 may be expressed as $C(r)/C(a)$ equal to 0.25. The penetration distance achievable by diffusion alone is r=4a. For a 50 μm diameter capillary tip, this corresponds to a penetration distance of roughly 100 μm. For a 100 μm diameter capillary tip, this corresponds to a penetration distance of roughly 200 μm. Therefore, a ratio of the penetration distance at 25% of I_0 of the electrokinetic transport of $Ru(bpy)_3^{2+}$ to diffusion alone at 40 minutes was calculated as 22 and 15 for the 100 μm and 50 μm diameter capillary tips respectively.

The infusions can also be evaluated in terms of *Pe*, obtained from fitting the experimental fluorescence intensity versus distance data to Equation 5.1. Equation 5.1 was derived for the steady-state condition, as discussed in Chapter 3, but it was applied to this data set because it had been previously validated for small capillary tips and not due to a belief that 40 minute infusions achieved steady-state. In fact, the time to steady-state should scale linearly with the capillary tip diameter. For instance, the time to steady-state for 1.0 μA ejections of **TR70** from an approximately 4 μm capillary tip diameter into a -24.7 mV ζ-potential hydrogel was estimated as 1,610 seconds (~27 minutes) in Chapter 3, and therefore the time to steady-state would take roughly 20,125 seconds (~335 minutes) for similar infusions from a 50 μm diameter capillary

tip. Nonetheless, fitting the intensity versus distance data to Equation 5.1 yielded R^2 greater than 0.98 in all instances. A plot of the experimentally derived *Pe* versus time are provided in Figure 5.5.

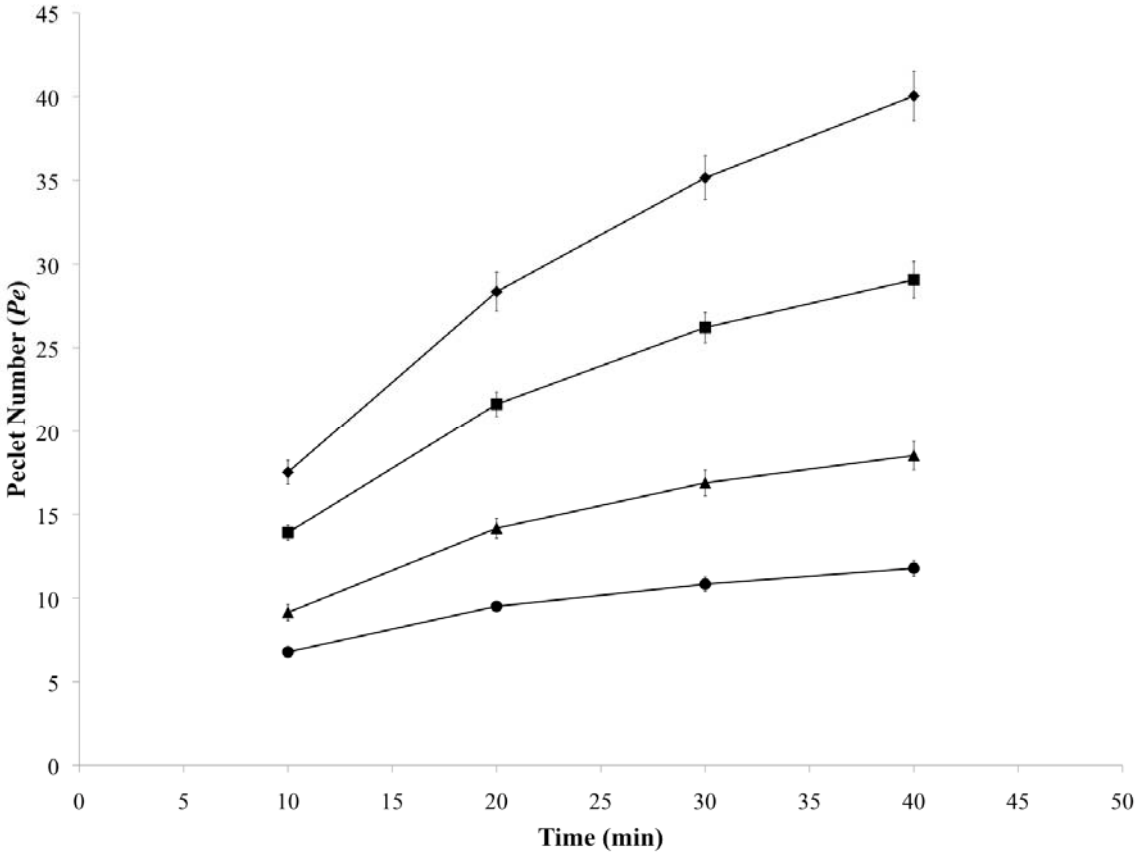

Figure 5.5. Effect of applied current on *Pe* over time (min) for $Ru(bpy)_3^{2+}$ from a 50 µm diameter capillary tip in a hydrogel with -24.7 mV ζ-potential: circle, 0.2 µA (N = 5), triangle, 0.5 µA (N = 5), square, 1.0 µA (N = 5), diamond, 1.5 µA (N = 5).

The *Pe* demonstrated a time-dependent increase over the range of currents from 0.2 to 1.5 µA. With the lowest current (0.2 µA), *Pe* began to approach its limit after around 40 minutes, while *Pe* continued to increase with higher currents during the same timeframe. Based on data from Chapter 3 and Equation 5.2, the time to steady state for 0.2 µA infusions from a 50 µm diameter capillary tip should take roughly 6,150 seconds (~103 minutes). Furthermore, the *Pe*

should not vary during steady-state infusions of a molecule from a capillary tip. Clearly there was variability of *Pe* over time with a particular capillary tip size from 0.2 to 1.5 μA, indicating the infusions were not actually at steady-state. The time to reach constant *Pe* may be considered as an indirect indicator of the time to reach steady-state. Of note, lower applied currents seemed to be reaching constant *Pe* (and thus steady-state) faster than with higher applied currents. This result is consistent with the data presented in Chapter 3 for short-distance ejections.

With a particular capillary tip size (~50 μm diameter) and the same $Ru(bpy)_3^{2+}$ infusate, experimental time, and hydrogel conditions, only the applied electrical current was varied. As shown in Figure 5.6, the penetration distance increased predictably over a range of currents from 0.5 to 1.5 μA, for percentages of I_0 equal to 75%, 50%, and 25%. Over this narrow range of applied currents, the distances where 25% of I_0 occurred at 1,342 ± 67 μm (N = 5) away from the capillary tip and 1,682 ± 36 μm (N = 5) away from the capillary tip after 40 minutes of infusion for 0.5 and 1.5 μA currents respectively. Furthermore, there was only an approximately 2 to 5% error in the penetration distances, indicating the highly reproducible nature of the infusions. The ratio of the penetration distance at 25% of I_0 of the electrokinetic transport of $Ru(bpy)_3^{2+}$ to diffusion alone was 14 and 17 for the 0.5 and 1.5 μA currents respectively. Thus, increasing the applied electrical current resulted in greater perfusion distances.

Finally, Figure 5.7 shows the current-dependent change in maximum fluorescence intensity (I_0) of $Ru(bpy)_3^{2+}$ after 40 minutes of infusion using varying applied electrical currents. With increasing current from 0.2 to 1.5 μA, the fluorescence intensity just outside of the capillary tip began to approach its limit. At higher currents (i.e.: 1.5 μA), the fluorescence intensity outside of the tip started to approximate the fluorescence intensity within the capillary itself.

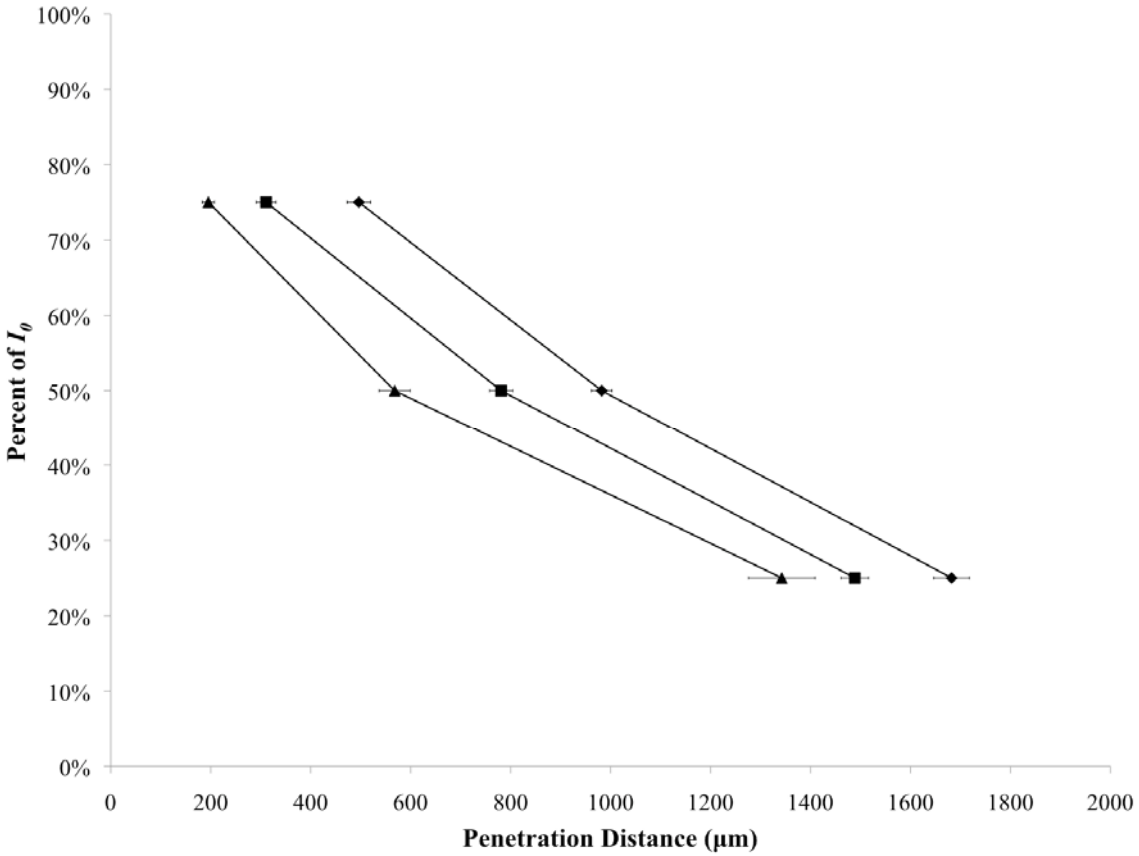

Figure 5.6. Effect on penetration distance (μm) with varying current from 50 μm capillary tip infusions for 40 min of $Ru(bpy)_3^{2+}$ in a hydrogel with -24.7 mV ζ-potential: triangle, 0.5 μA (N = 5), square, 1.0 μA (N = 5), diamond, 1.5 μA (N = 5).

It should be noted that these experiments all utilized a small, highly charged molecule, $Ru(bpy)_3^{2+}$, as the electrokinetic infusate. This molecule was selected because it has an appreciably positive electrophoretic mobility, and was therefore expected to strongly interact with the applied electric field. As such, the electrophoretic and electroosmotic velocity vectors were aligned, with resulting enhancement of electrokinetic transport. As discussed in Chapter 1 and elucidated in subsequent chapters, electrokinetic transport is fastest when the electroosmotic and electrophoretic vectors are aligned, as in the case of $Ru(bpy)_3^{2+}$. In the case of a neutral molecule of similar size, the electroosmotic velocity vector is the primary motivating force

behind transport and the molecule would travel a shorter distance since there is no contribution from electrophoresis. Finally, for negatively charged molecules of a similar size, the electrophoretic and electroosmotic velocity vectors are opposed to one another, and consequently the rate of transport would be even less (if it all). With the significant ζ-potential of fused silica capillaries,[170, 173, 214, 215] the molecules used in previous chapters – **TR70**, **FL70**, **TR3**, and $Ru(bpy)_3^{2+}$ – all may be ejected. However, the rate of transport away from the capillary is based upon molecular weight and electrophoretic mobilities, $Ru(bpy)_3^{2+}$ is expected to travel furthest in a given time, followed by **TR3**, then **TR70**, and finally **FL70**.

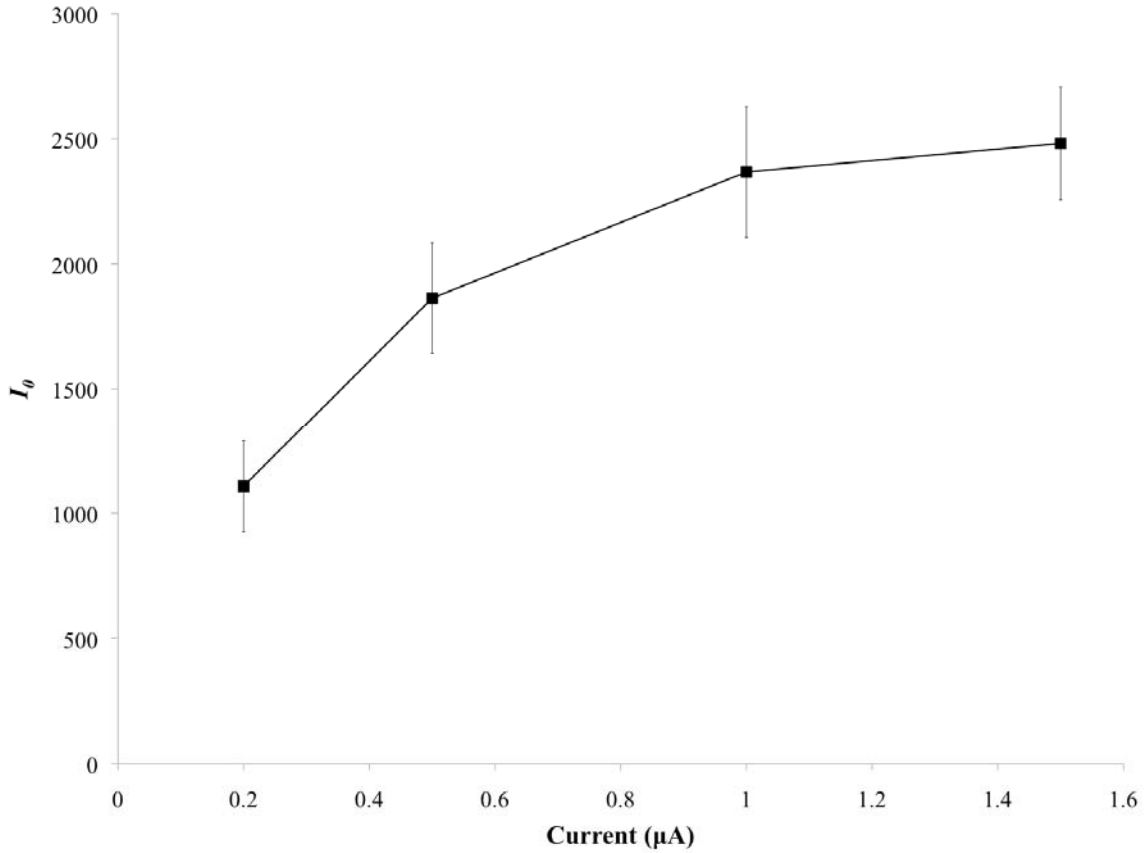

Figure 5.7. Effect of applied current on the maximum fluorescence intensity (I_0) for $Ru(bpy)_3^{2+}$ infusions from a 50 μm capillary tip in a hydrogel with -24.7 mV ζ-potential. Data taken after 40 minutes of ejection, $N = 5$ each data point.

5.3.2 Electrokinetic Transport Determined by Current Path

Pressure-driven delivery of molecules in clinical trials elucidated several complications related to controlling the direction of fluid flow.[195, 202, 203, 205-212] In these trials, infusions followed paths of least pressure resistance (which did not usually coincide with their target path), and often penetrated ependymal linings with uncontrolled ejections into the ventricular system, flowed backwards along the infusion cannula, or deformed the brain tissue itself. Electrokinetic transport utilizes the path of current flow, as demonstrated from prior work with 2 μm borosilicate capillary tips.[164] Building from this work, a greater control of transport over wider tissue areas is necessary for clinical applications. For example, placement of a counter-electrode within a tumor may direct the flow of a molecule towards the tumor interior.

To test this hypothesis, the ability to control the directional path of capillary infusions with counter-electrode placement was examined. Figure 5.8 shows dramatic bending of a fluorophore's path over more than 400 μm, as a **TR70** solution in GF-HBSS was infused from an approximately 20 μm diameter capillary tip positioned at the dorsal tip of the dentate gyrus towards an unpulled 100 μm diameter counter capillary placed at the interface between CA1 and CA3 in an OHSC, as described in Figure 5.2. In this example, **TR70** was transported along a current path towards the counter capillary, with no backflow along the infusion capillary. Moreover, because **TR70** had an essentially zero electrophoretic mobility, this anisotropic transport was predominantly due to electroosmosis. As with the ejections of **TR70** into OHSC presented in Chapter 3, a roughly spherical infusion profile was seen if the counter electrode was placed remotely. The ejection shown in Figure 5.8 is unique because of the dramatic bending towards the counter capillary, which cannot be a result of diffusion.

To quantify this ejection, a series of three regions of interest were identified to determine the average fluorescence intensities at the initiation and cessation of electrical current application. One region was drawn over the lumen of the counter capillary 420 μm away from the injection capillary tip (Region 1), a second was 420 μm away from the injection capillary tip (Region 2), and a third was drawn remotely (1,025 μm from counter capillary) to determine the background fluorescence (Region 3). The background-corrected average fluorescence intensities were 50.1 (range: 5 to 100) and 26.5 (range: 19 to 29) for Regions 1 and 2 respectively prior to the initiation of the electrical current. After a 0.3 μA current was applied for 20 minutes, the background-corrected average fluorescence intensities were 148.7 (range: 64 to 224) and 13.4 (range: 12 to 23) for Regions 1 and 2 respectively. Anisotropic transport of **TR70** towards the counter capillary is not possible by diffusion.

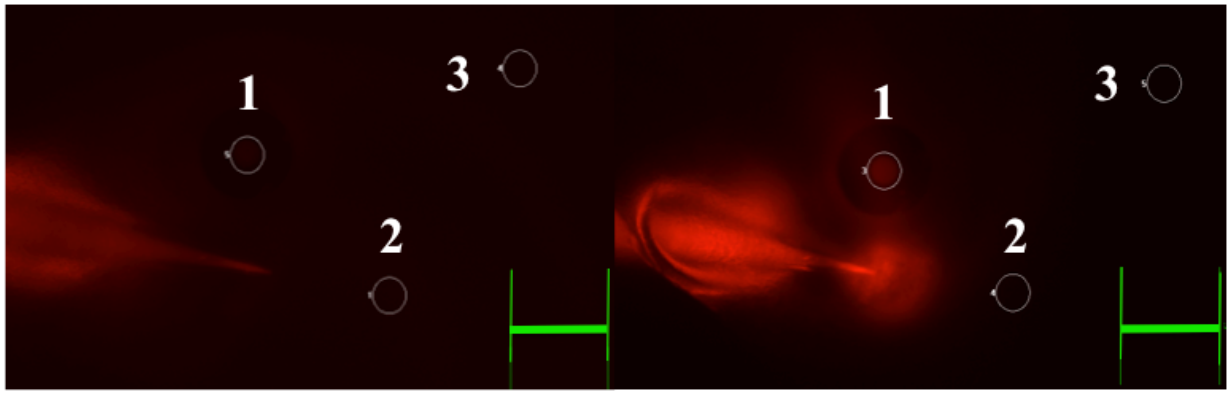

Figure 5.8. Dual capillary experiment in OHSC with 0.3 μA of applied current. The pulled 20 μm diameter infusion capillary is filled with **TR70** and inserted at the dorsal tip of the dentate gyrus at a 20° angle to the OHSC surface. The 100 μm diameter unpulled counter capillary is filled with GF-HBSS and inserted approximately 420 μm away at the interface between CA1 and CA3 at a 90° angle to the OHSC surface. The left panel was at the start of the experiment and the right panel is following 20 minutes of applied current. The fluorescence intensities were determined in each region of interest, denoted by the white circles. The green scale bar is 350 μm.

A defined current path affords greater control of electrokinetic infusion and addresses a key limitation of pressure-infusion borne out through clinical trials.[211, 212] The counter capillary

may not be positioned at any distance away from the infusion capillary, however. The electric field away from a point source is proportional to $1/r^2$ (where r is the distance away), and therefore decays rapidly from the capillary tip. It is reasonable to conclude that electrokinetic transport cannot occur when the electric field becomes zero, and as the electric field diminishes at further distances, the rate of transport decreases.

In a second example shown in Figure 5.9, the counter capillary was replaced with an Ag wire (0.3 mm diameter) as the counter electrode and inserted into CA3 of an OHSC. The 20 μm pulled infusion capillary was replaced with an 100 μm unpulled infusion capillary filled with a 45 mM $Ru(bpy)_3^{2+}$ solution in GF-HBSS. The infusion capillary was inserted onto CA1 perpendicular to the plane of the OHSC. This setup was shown in Figure 5.1. As the diameter of the infusion capillary tip was significantly increased in this example, the corresponding electric field emanating from the tip was expected to remain appreciable at much further distances in the OHSC. Three linescans were drawn in Figure 5.9, shown as bold white lines to quantify the fluorescence intensity through the same drawn planes. Figure 5.9 shows the infusion of $Ru(bpy)_3^{2+}$, with a bent path towards the counter electrode and increased fluorescence within the OHSC, after 25 minutes of applied 1.5 μA current with no GF-HBSS below the insert membrane.

To direct the electrical current away from the OHSC, the counter electrode was placed remotely and immersed in GF-HBSS beneath the insert membrane. Under these conditions, the preferential transport of $Ru(bpy)_3^{2+}$ through the OHSC was abolished, and the fluorescence was instead localized around the capillary tip in an approximately isotropic manner, with a diminished fluorescence intensity within the OHSC.

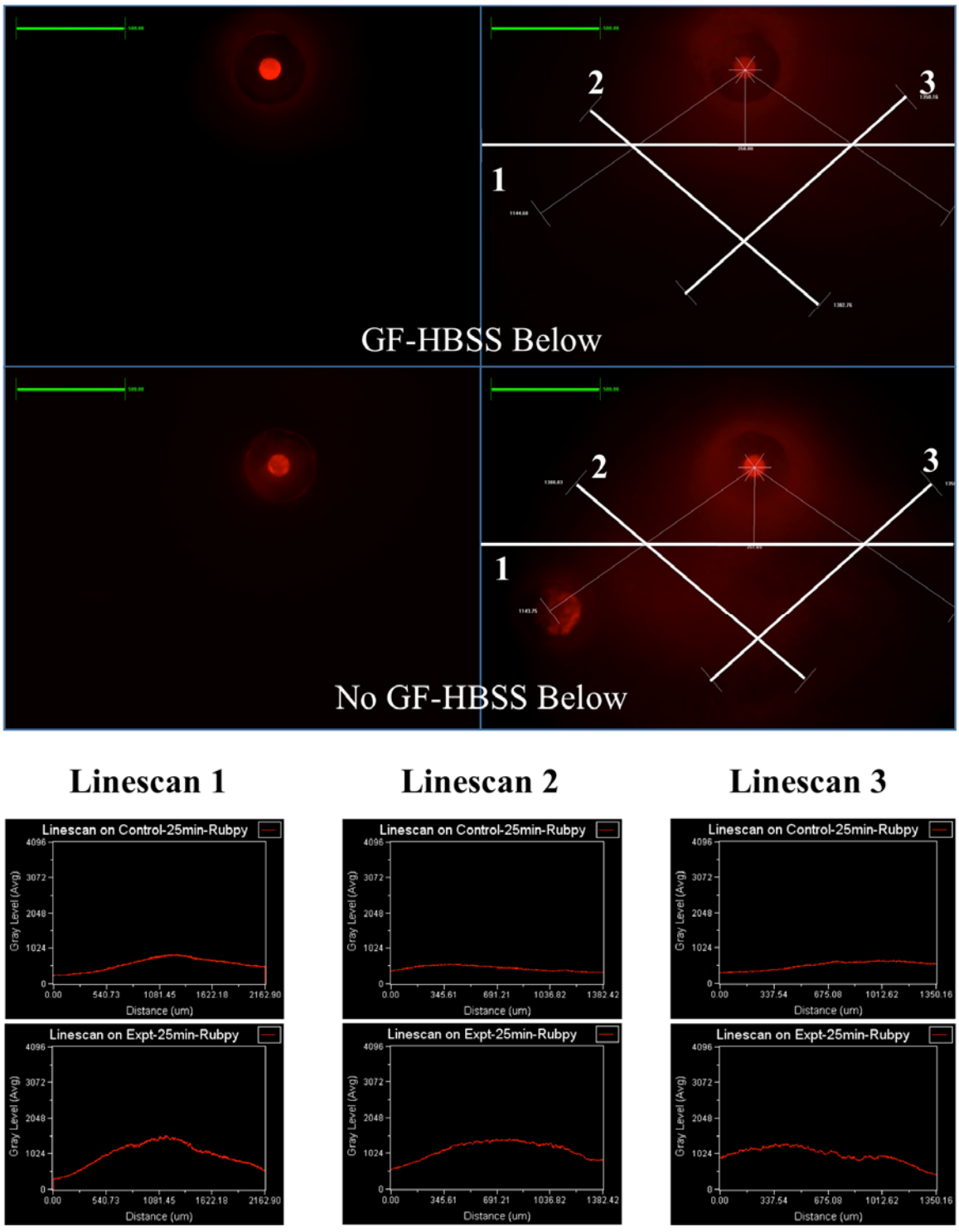

Figure 5.9. Single capillary experiment in OHSC with 1.5 μA of applied current for 25 minutes. The unpulled 100 μm diameter infusion capillary was filled with $Ru(bpy)_3^{2+}$ and inserted onto CA1 at a 90° angle to the OHSC surface. The Ag counter electrode was inserted approximately 1 mm away into CA3 (bottom panel) or remotely in GF-HBSS beneath the insert membrane (top panel). The fluorescence intensity linescans on the far right represent the white horizontal lines drawn across the middle two panels, with those for the top panel above those of the bottom panel. The green scale bar is 500 μm.

Linescan 1 represented the horizontal plane across the imaging field, located 350 μm away from the infusion capillary. Linescan 2 represented the perpendicular plane 600 μm between the infusion capillary and counter electrode. Linescan 3 represented a mirrored plane of linescan 2 that was 600 μm away from the infusion capillary. There was considerably more fluorescence across the linescans when the current was directed through the OHSC, as compared to the control experiment. Linescan 1 revealed an almost two-fold increase in the fluorescence intensity when the current path was directed through the OHSC. In linescan, 2 the lower distances describe the region nearest the infusion capillary, while the larger distances describe the same region in linescan 3. When the current was not passed through the OHSC due to the introduction of GF-HBSS below the insert membrane, the maximum fluorescence intensity occurred at roughly 380 and 1,015 μm on linescans 1 and 2 respectively. In contrast, the maximum fluorescence intensity occurred at approximately 710 and 390 μm on linescans 1 and 2 respectively when the current was passed through the OHSC. This indicates that the maximum intensity passing through the linescan planes was further from the region of the infusion capillary when the current path was directed through the OHSC. Thus, Figure 5.9 further demonstrates the potential for controlled electrokinetic transport, whereby the current path may dictate molecular transport.

5.3.3 Infusion from a Doped Hydrogel

Because of issues with backflow and lack of directional control with pressure-driven infusion, only deep areas of the brain may be targeted. One can intuitively imagine that surface ejections using pressure would cause the infusate to spread across the cortical surface without deep penetration. To address this limitation with electrokinetic delivery, a hydrogel with a ζ-

potential similar to brain tissue (OHSC) was used as a flexible infusion pad to deliver a fluorophore over wide areas, with the experimental setup described in Figure 5.3. Figure 5.10 shows the hydrogel doped with **TR3** placed over the subiculum and entorhinal cortex at one end of an OHSC. A second undoped, non-fluorescent hydrogel was placed on the other edge of the OHSC over the edge of CA3. The distance between the two hydrogels was 1,500 μm. A Ag electrode was inserted into each hydrogel, with current flow from the doped hydrogel through the OHSC towards the non-fluorescent hydrogel.

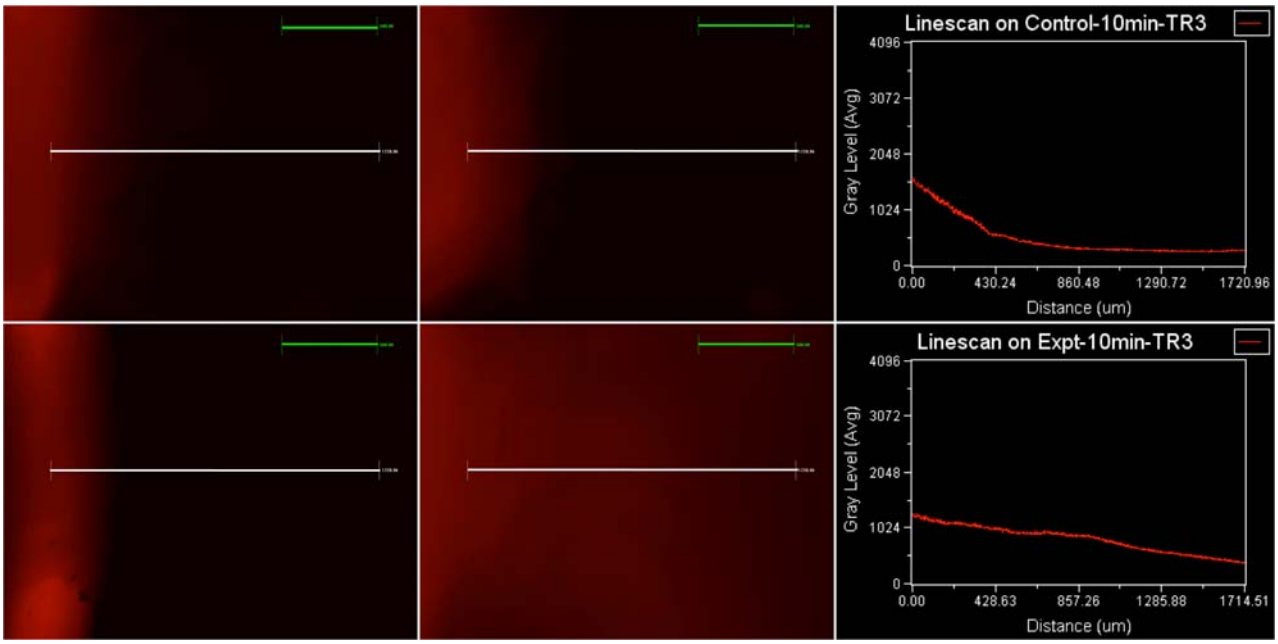

Figure 5.10. Doped hydrogel infusion of **TR3** through OHSC after 10 minutes of a 10.0 μA of applied current. The Ag counter electrode was inserted into a non-fluorescent hydrogel over the opposite edge of the OHSC, approximately 1.5 mm away. When GF-HBSS was in contact with the insert membrane (top panel), the current path was different than without GF-HBSS below the insert membrane (bottom panel). The fluorescence intensity linescans on the far right represent the white horizontal lines drawn across the middle two panels. The green scale bar is 500 μm.

With an applied current of 10.0 μA, **TR3** was transported across the entire OHSC (distance ~1,500 μm) over a period of 10 minutes. Though current was actually applied for 12 minutes, the insert membrane began to dry out after 10 minutes resulting in obscured imaging for

the remaining two minutes. When the current path was directed away from the OHSC (and instead was directed through the insert membrane to the GF-HBSS underneath), diminished electrokinetic transport across the OHSC was observed.

The horizontal linescans provided quantification of the **TR3** fluorescence intensity passing through the OHSC. When the current path passed through the OHSC, the linescan revealed the penetration distance at 25% of I_0 to be approximately 1,260 μm away from the doped hydrogel, almost fully across the distance between the two hydrogels. In contrast, when the current was directed away from the OHSC, and instead through the insert membrane to the GF-HBSS below, the penetration distance at 25% of I_0 occurred at nearly 320 μm away from the doped hydrogel. Similar to the results presented in section 5.3.2, the electrical current path may be used to control the path of electrokinetic transport.

This experiment also provided evidence that larger tissue areas may be impacted by doped hydrogel infusions, in a faster time and at higher currents, than by capillary infusions. This is partly due to a striking difference in the decay of the electric field within the OHSC. A hemispherical point source for the electric field can no longer be assumed for doped hydrogel infusions. Instead, the electric field between the two hydrogels can be better approximated by the electric field between two conducting plates. If the plates are of infinite in size, the electric field between the plates is constant and does not decay. Furthermore, the distance between the conducting plates determines the magnitude of the electric field. As the dimensions of the bases of the doped and counter hydrogels were larger than the OHSC, the electric field was roughly constant throughout the OHSC between the hydrogels (assuming negligible edge effects due to the hydrogels not actually being “infinite” in size).

Of note, the doped infusion hydrogel became dehydrated after the application of 10.0 μA of current, with transfer of the fluid (and **TR3**) into the OHSC and towards the counter hydrogel. This result indicated that molecules may be delivered to the cortical surface or a resection bed using electroosmosis, a feat not achievable with pressure-driven delivery.

5.3.4 Electrokinetic Ejections *In Vivo*

In section 5.3.1, the transport properties of various molecules were predicted from electrophoretic mobilities and molecular weights. Three molecules of varying molecular weight and electrophoretic mobilities were utilized for *in vivo* infusions. **BODIPY10** and **TR70** were selected because of their dissimilar molecular weights, their ability to be resolved spectroscopically, and their small electrophoretic mobilities, as shown in Table 5.1. Therefore, a difference between the volumes of tissue impacted by these two fluorescent dextran conjugates was predominantly due to the molecular weight difference. The small, cationic molecule – $Ru(bpy)_3^{2+}$ – was expected to travel a much further distance than **BODIPY10** or **TR70** during a particular infusion time because of its relatively small molecular weight and dicationic nature (positive electrophoretic mobility).

Table 5.1. Comparison of molecules used during *in vivo* infusions and their volumes of distribution (V_d).

Infusate	Molecular Weight	Electrophoretic Mobility (μ_{ep}) (10^{-9} m^2/Vs)	V_d at 25% of I_0 (μL)
TR70	70,000	0.46 ± 0.03 (N = 3)	0.60 ± 0.04 (N = 3)
BODIPY10	10,000	-0.89 ± 0.22[21] (N = 3)	1.71 ± 0.12 (N = 3)
$Ru(bpy)_3^{2+}$	570	25.86 ± 0.02 (N = 3)	13.0 ± 2.0 (N = 4)

Infusion of the three molecules was completed by stereotactic placement of two 100 μm diameter fused silica capillaries into the thalami of rat brains. The infusion capillary contained the fluorophore in a GF-HBSS solution, whereas the counter capillary contained only GF-HBSS. As shown in Figure 5.11 for the infusion of $Ru(bpy)_3^{2+}$, the volume of distribution may be quantitatively determined by determining the infusion area within each slice, multiplying by the slice thickness (300 μm), and finally by summing together the volumes of the individual slices. The trajectory of the infusion capillary is clearly observed in Figure 5.11. One of the experimental runs for the co-infusion of **TR70** and **BODIPY10** was excluded because the capillary slipped during the infusion, and was consequently spread over a significantly larger volume and was a clear outlier.

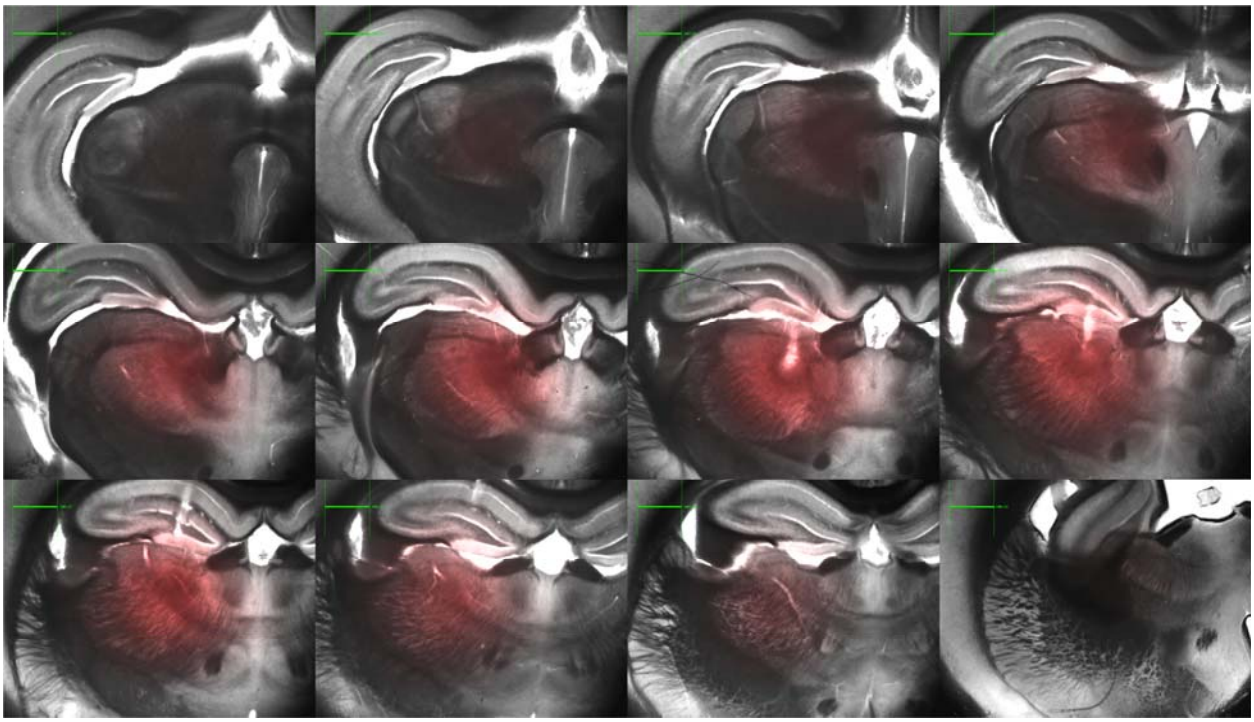

Figure 5.11. Typical *in vivo* ejection of $Ru(bpy)_3^{2+}$ into the rat thalamus with 25.0 μA of applied current for 45 minutes. Fluorescence was overlaid upon bright field images, and presented left-to-right from anterior (top left) to posterior (bottom right). The green scale bar is 1,000 μm.

With this volumetric analysis method, it was critical to quantitatively section the tissue without discarding tissue in the region where there is fluorescence. This was achieved by transcardial perfusion and rapid fixation of the tissue with an 8% paraformaldehyde, followed by vibratome sectioning, and imaging. This method for tissue preparation typically was completed in less than 30 minutes. Discrete, well-delineated fluorescence spots were visible more than three days after tissue fixation with unchanged spot sizes. Thus, negligible diffusion of the molecules beyond the region attained by electrokinetic transport occurred during the 30 minutes required for tissue preparation period, as the transcardial perfusion was completed less than five minutes after termination of the electrical current.

As described in Table 5.1, the volumes of distribution (V_d) for the three molecules at 25% of I_0 were obtained with good reproducibility (data presented as means ± standard error of the mean). The largest molecule evaluated, **TR70**, had a molecular weight of 70,000 and a roughly zero electrophoretic mobility. The V_d of **TR70** fluorescence was determined as 0.60 ± 0.04 μL (N = 3). **BODIPY10** had a molecular weight of 10,000 and also demonstrated a roughly zero electrophoretic mobility. The V_d of **BODIPY10** fluorescence was determined as 1.71 ± 0.12 μL (N = 3). Finally, $Ru(bpy)_3^{2+}$ was the smallest molecule evaluated, with a molecular weight of roughly 570, though its electrophoretic mobility was significant and positive as a result of its dicationic nature. The V_d of $Ru(bpy)_3^{2+}$ fluorescence was determined as 13.0 ± 2.0 μL (N = 4).

To control for diffusional transport from the capillary tip, an identical 100 μm diameter fused silica capillary was filled with the fluorophore solution and implanted into the rat thalamus for 45 minutes with no applied current. Immediately following this time period, the rat was perfused transcardially and 300 μm slices were obtained, as described earlier. For **TR70**,

BODIPY10, and $Ru(bpy)_3^{2+}$, no fluorescence was observed in the brain tissue around the capillary implantation site.

The error in V_d presented in Table 5.1 ranged from roughly 5 to 15%. Moreover, the shape of the ejection spot was only sometimes circular, and therefore approximating the area within a slice as πr^2 may not be accurate in all instances. To arrive at the value of r, eight different radii were measured at 45° intervals and averaged together. The center of each spot, from which the radii are drawn, was determined by locating the maximal fluorescence intensity. Finally, the location of the capillary implantation site was slightly variable between rats. Though injections occurred in the thalamus in all instances, there was some variability in the depth, due to differences in rat weight. If the capillary was implanted near the tissue edge of the thalamus, the radius along a particular measurement direction may theoretically be truncated with a consequently smaller area. The percent error of the volume distribution was highest for $Ru(bpy)_3^{2+}$, which most readily encountered the tissue margins due to its large ejection areas. Thus, this final point is thought to play a role in the measurement error.

Of particular interest, the tortuosity – and in particular the frictional drag force – also determined the penetration distance (and V_d) a molecule achieved in a given time span. The frictional drag force generated by the tissue for the three molecules was likely not the same. As presented in Chapter 1, this drag force includes steric effects, reptation and entropic barrier transport of linear, flexible molecules, changes in the diameter of channels in the extracellular space during non-homeostatic conditions, anisotropy of the tissue architecture, clearance of a molecule from the extracellular space, and any biochemical reactions that may occur in the tissue itself.

Through this dissertation and others, it has been determined that the tortuosity is larger with increasing molecular weight in brain tissue,[59] and this effect is likely due to steric effects, reptation, entropic barrier transport, and the diameter of channels in the brain extracellular space. The tortuosity for a 70 kDa dextran conjugate in cortical slices from rats was found to be 2.25 ± 0.09, whereas this value was only 1.63 ± 0.05 for a 10 kDa dextran conjugate.[59] Furthermore, the fluorescent dextran conjugates used in these experiments do not show affinity for cellular membranes or reactivity in the extracellular matrix.[21] The rate of fluid clearance from the given volume of brain tissue *in vivo* (such as for fluid introduced by an infusion) ranges from approximately 0.3 to 0.5 μL min^{-1} mL^{-1}.[89] For an adult rat brain, with a volume on the order of 1.75 mL, this corresponds to a clearance rate of roughly 0.53 to 0.88 μL/min. This clearance rate was appreciable with respect to the volume of solution introduced into the rat brains (V_i) during infusions.

The V_i was estimated by determining the electroosmotic velocity through the capillary tip multiplied by the area of the capillary tip. To determine the electroosmotic velocity, the ζ-potential of the brain tissue was estimated to be approximately -22.8 mV.[22] The flow rate through a 100 μm fused silica capillary with a current of 25.0 μA was therefore 0.016 μL/min. Thus, over 45 minutes, approximately 0.72 μL of the fluorophore solution was introduced into the thalamus.

Estimating the electrokinetic flow rate was not trivial, especially at the interface of two media with varying ζ-potentials. In the absence of a ζ-potential mismatch, the flow rate would be calculated with the ζ-potential of fused silica, and would be higher (approximately 0.04 μL/min). The ζ-potential of the fused silica capillary was estimated to range from approximately -50 to -60 mV,[173] while the ζ-potential of the OHSC was assumed to be -22.8 mV,[22] and provided a

reasonable estimation for the thalamus. Thus, a ζ-potential mismatch did occur, with the development of positive-pressure just outside of the capillary tip.[20, 174] However, no visible tissue deformation due to increased pressure was observed at the capillary implantation site. Therefore, the pressure outside of the capillary tip likely decreased the flow rate from the capillary instead. Using the ζ-potential of the brain tissue provided a conservative estimate of the electrokinetic flow rate.

To compare the electrokinetic V_d to those obtained by pressure-driven infusion, whereby the volume of distribution was estimated at a distance of more than 15% of the concentration of the infusion solution,[195] the electrokinetic V_d must be translated to distances of 15% rather than 25% of I_0. Due to fluorescence signal to noise issues at such low intensities, especially for **TR70**, this was not determined experimentally. Instead, this may be accomplished by Equation 5.3, assuming a spherical ejection.

$$\text{Volume}_{15\%\text{ "Edge"}} = \left(\frac{0.85}{0.75}\right)^3 \times \text{Volume}_{25\%\text{ "Edge"}} \qquad 5.3$$

Therefore, the V_d at 15% of I_0 were 0.87 ± 0.06 μL for **TR70** (N = 3), 2.49 ± 0.18 μL for **BODIPY10** (N = 3), and 18.88 ± 2.85 μL for $Ru(bpy)_3^{2+}$ (N = 4).

According to Chen *et al*., the resulting V_d of radiolabeled albumin (MW 69 kDa) was 20.8 ± 2.10 μL, assuming an infusion volume of only 4.0 μL into the rat striatum with a 0.5 μL/min flow rate.[195] This resulted in a ratio of the V_d to V_i of 5.2 ± 0.5. With this flow rate, a roughly 5% leakage was observed, and at higher flow rates (1.0 μL/min) the leakage exceeded 20%.[195] In contrast, electrokinetic infusion of **TR70** (MW 70 kDa) using a 100 μm fused silica capillary with a current of 25.0 μA resulted in a V_d of 0.87 ± 0.06 μL and a V_i of 0.72 μL. Therefore, the ratio of the V_d to V_i for **TR70** was 1.2 ± 0.1. The ratios of the volume of distribution to the volume of infusion for **BODIPY10** and $Ru(bpy)_3^{2+}$ were 3.5 ± 0.3 and 26.2 ±

4.0 respectively. The ratio for **TR70** was lower, yet comparable, to pressure-driven infusion in the rat brain.[195] While a 0.5 μL/min flow rate represented the highest flow rate without substantial backflow, the data for albumin by pressure-driven infusion represented a maximum V_d to V_i in brain tissue. In contrast, the electrokinetic flow rate of 0.016 μL/min was limited only by the available electronic equipment and not by the brain tissue. In contrast, V_d to V_i ratio was determined as 13:1 for radiolabeled sucrose (MW 359) in the cat brain to the 1% isodose,[194] though this may have been limited by the volume of brain tissue itself. If Equation 5.3 was calculated to the 1% edge for a comparably-sized molecule – $Ru(bpy)_3^{2+}$ – then the V_d to V_i ratio was roughly 41:1.

The current density for a 100 μm diameter capillary tip with 25.0 μA of applied current, as utilized *in vivo*, was 3,180 A/m^2 at the tip. In contrast, the current density for 0.5 μA ejections from an approximately 4 μm diameter capillary tip, as utilized in Chapter 3 for OHSC ejections, was 39,790 A/m^2 at the tip. No appreciable cell death, as evident by propidium iodide staining, was visible at this current density in OHSC.[164] Finally, electroporation from a 2 μm diameter capillary tip with a typical current of 0.125 μA also yielded a current density of 39,790 A/m^2 at the tip.[216] To achieve higher, yet "safe," current densities similar to the OHSC or electroporation conditions for *in vivo* ejections from a 100 μm diameter capillary tip, the applied current would need to be around 0.3 mA. Milliamp currents are regularly used in patients with deep brain stimulation (DBS), with a 25.5 mA current passed through a 0.06 cm^2 electrode surface resulting in a current density of 4,250 A/m^2.[217] Therefore, there is considerable opportunity to increase the applied electrical current in this system with a 100 μm diameter capillary tip, and ultimately increase the flow rate from the capillary and eventually the V_d achieved by electrokinetic transport.

A number of interesting observations were compiled during the course of these *in vivo* experiments. Before the evaluation of volumetric data was attempted from thalamic infusions, a number of hippocampal infusions were conducted. The tissue volume of the hippocampus is much less than the thalamus, and in the case of $Ru(bpy)_3^{2+}$ the hippocampal tissue margins were always reached during 25.0 μA ejections over 45 minutes with a 100 μm diameter capillary tip. As such, these infusions were not included in the volumetric data presented in Table 5.1. Nonetheless, migration of $Ru(bpy)_3^{2+}$ was observed along several points of tissue connections.

As shown in Figure 5.12, hippocampal infusions of $Ru(bpy)_3^{2+}$ resulted in transport into the contralateral hippocampus and other adjacent areas through points where the tissue was physically (and biologically) connected or even simply touching, such as through the posterior sections of the corpus callosum. The posterior portion of the corpus callosum has two orthogonal linescans drawn through it in Figure 5.12. The infusion capillary was inserted into the hippocampus at the left, 300 μm anterior to the plane of this image. In the top right panel of Figure 5.12, the vertical linescan was evaluated. Appreciable fluorescence was observed primarily within the posterior corpus callosum tissue connection, but nowhere else. This fluorescence extends into the contralateral hippocampus (and towards the site of the counter capillary), as described by the bottom right panel that describes the horizontal linescan. Building upon sections 5.3.2 and 5.3.3, this transport through connected and adjacent tissue was likely related to the current path, as some anisotropy appears to exist in the transport of $Ru(bpy)_3^{2+}$ with preferential movement towards the contralateral hippocampus with the counter capillary.

Meanwhile, this same phenomenon seemed to hold for thalamic infusions also. Figure 5.13 demonstrates transport of $Ru(bpy)_3^{2+}$ through tissue connections towards the contralateral thalamus and counter capillary. In this case, the massa intermedia (interthalamic adhesion) was

appreciably fluorescent, while the surrounding milieu approximated the baseline fluorescence intensity. The infusion capillary tract may be visualized in Figure 5.13. The top right panel of Figure 5.13 quantifies an appreciable fluorescence through the roughly 600 μm thick interthalamic adhesion that exists between the two thalami (linescan taken along the skewed vertical line). The bottom right panel shows the fluorescence intensity plot along the interthalamic adhesion (linescan taken along the skewed horizontal line), whereby there was a gradual decrease in fluorescence intensity as $Ru(bpy)_3^{2+}$ was transported towards the contralateral thalamus from the ipsilateral thalamus with a higher $Ru(bpy)_3^{2+}$ concentration.

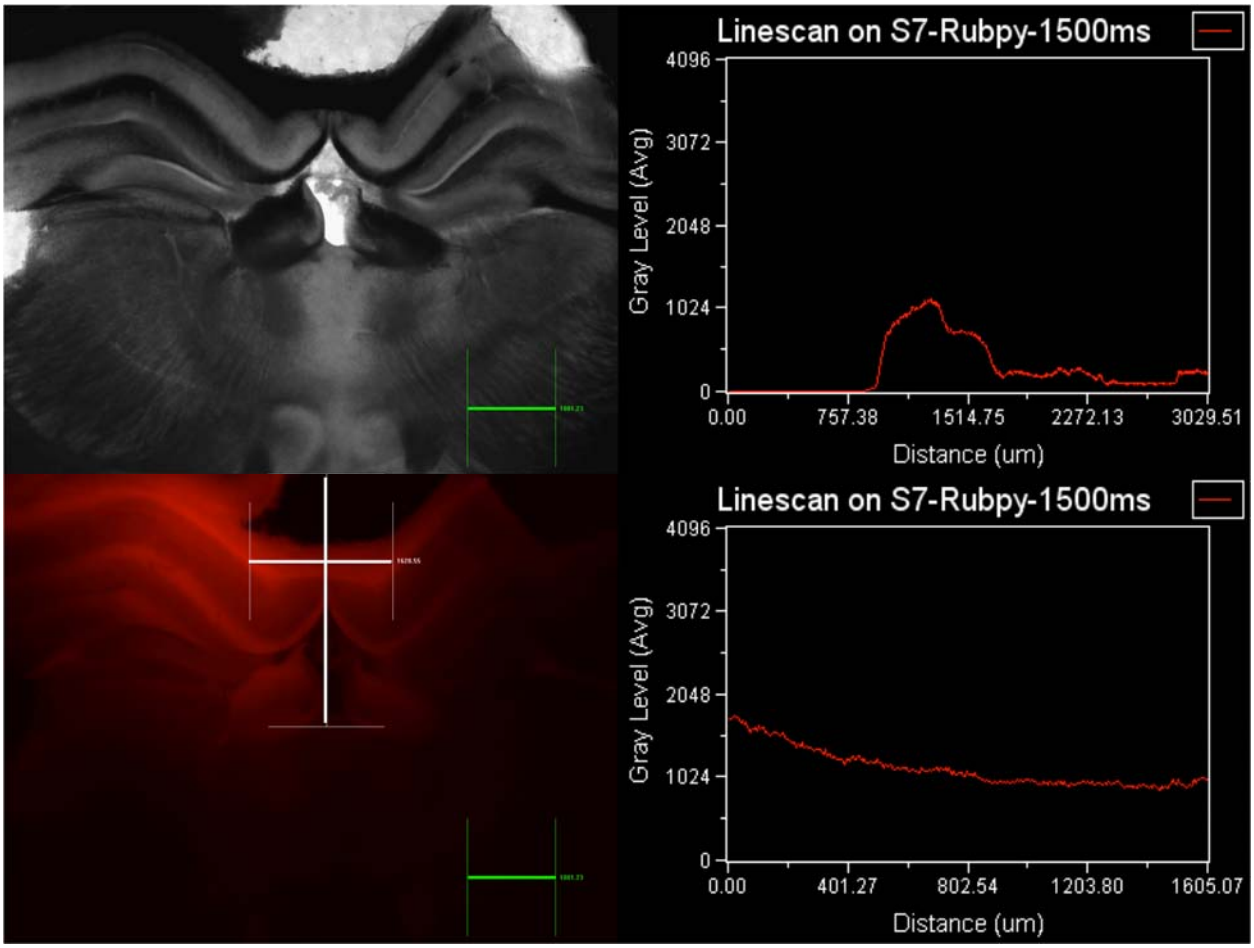

Figure 5.12. Example *in vivo* ejection of $Ru(bpy)_3^{2+}$ into the rat hippocampus with 25.0 μA applied current for 45 minutes with bright field (top left) and fluorescence (bottom left). The right panels represent the fluorescence intensity along the vertical (top right) and horizontal (bottom right) white linescans. The green scale bar is 1,000 μm.

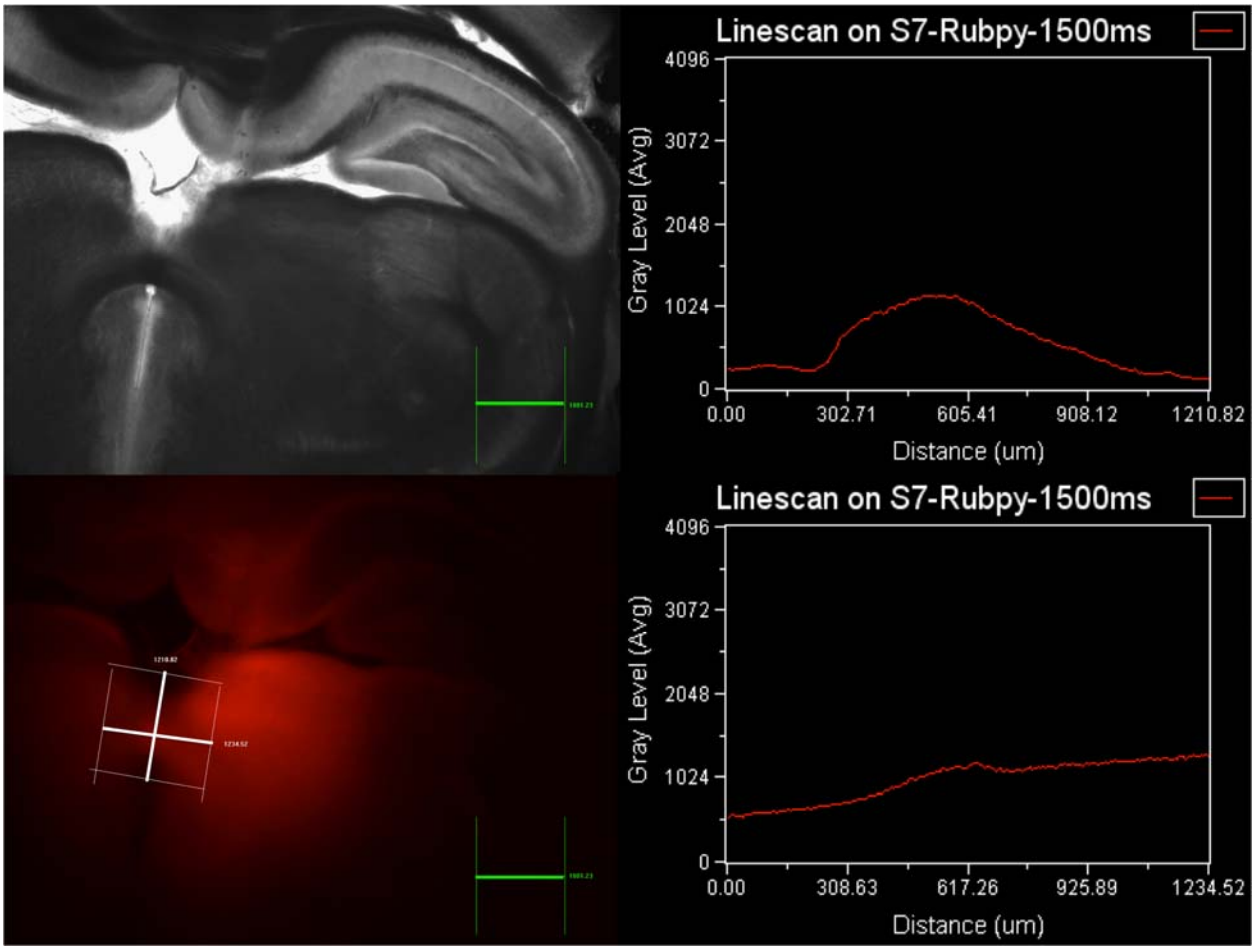

Figure 5.13. Example *in vivo* ejection of $Ru(bpy)_3^{2+}$ into the rat thalamus with 25.0 μA applied current for 45 minutes with bright field (top left) and fluorescence (bottom left). The right panels represent the fluorescence intensity along the skewed vertical (top right) and skewed horizontal (bottom right) white linescans. The green scale bar is 1,000 μm.

These two examples for hippocampal and thalamic infusions provide an interesting point for further research. Control of electrokinetic transport along a current path was previously elucidated in hydrogels[164] and OHSC. The data presented in this section provided some additional evidence that electrokinetic transport may be directed *in vivo* as well, with migration of a molecule along a current path towards a counter capillary positioned in the contralateral hippocampus or thalamus. The preferential transport of a molecule through the tissue may be contrasted with pressure-driven infusion.[195, 202, 203, 205-212] Tissue deformation and tearing,

backflow along catheter tracts, and the overall propensity for fluid to move along paths of least pressure resistance obfuscated clinical trial results, as discussed in Chapter 4. With all of the electrokinetic infusions, no visible tissue deformation or tearing occurred due to the volume of infusate. However, there was residual damage from implantation of the infusion and counter capillaries, which was visualized in some instances. However, the extent of damage resulting from capillary implantation in the small rat brain (and resulting neurological deficit) would likely be negligible in the much larger human brain.

5.4 CONCLUSIONS AND FUTURE DIRECTIONS

This chapter utilized fused silica capillaries with a more negative ζ-potential[170-173] and larger tip radii than presented in Chapter 3 with borosilicate capillaries. These modifications allowed for a significantly greater penetration distance to be achieved in hydrogels and OHSC. A range of applied currents was examined to deliver reproducible infusions of a small, highly charged molecule from a capillary tip. This methodology was further developed to rapidly infuse large surface areas from a hydrogel doped with a molecule of interest. Control of directional transport was also observed over several hundred micrometers to millimeters in OHSC. Finally, this work culminated in an *in vivo* proof-of-principle in the adult rat brain, whereby the ratio of the volume of distribution to volume of infusion by electrokinetic infusions were compared to those from pressure-driven infusions. With these *in vivo* experiments, a series of three molecules of varying electrophoretic mobilities and molecular weights were ejected to demonstrate the resilience of electrokinetic transport, and the effect of the tortuosity and its related frictional drag force, on achieving an ultimate volume of distribution. Anisotropic transport was observed in some

instances, whereby a molecule was directed towards the contralateral side (and counter capillary) through tissue connections.

These experiments, as are typical in scientific research, open the door for additional investigation. In particular, due to instrument limitations, applied currents greater than 25.0 μA were not evaluated. It is possible to utilize higher current densities *in vivo* than were examined in the present work.[164, 216, 217] Therefore, there is considerable opportunity to increase the applied current, as instrumentation allows.

Increasing the capillary tip size has also been shown to result in a dramatic increase of the penetration distance of a molecule. Doubling the capillary diameter for equivalent current ejections of $Ru(bpy)_3^{2+}$ into hydrogels yielded an approximately three-fold increase in the penetration distance. This relationship is hypothesized to be linear, and therefore it may be possible to achieve even greater volumes of tissue impacted as a result of ejections from a larger diameter capillary tip.

Longer infusion times may also be evaluated *in vivo*. Clinical pressure-driven infusions typically proceed over several hours, whereas our maximum infusion time was only 45 minutes (to prevent hydrogel and tissue dehydration). Our ejections *in vivo* were not at steady-state, despite fitting Equation 5.1 with good correlation, therefore it was difficult to make comparisons based on time. The time to steady-state increases for larger capillary tip diameters and greater applied electrical currents.

Finally, directional transport *in vivo* may be further evaluated, building from the several examples presented in this dissertation. For example, larger volumes of tissue may be impacted by the implantation of multiple capillaries spaced at given intervals to afford overlap of the electric field lines. In this instance, directional transport of a molecule may be controlled with

greater accuracy. Perfusion of a surgical resection bed or natural tissue cavity from a doped hydrogel may allow rapid conveyance of a molecule to wide areas of tissue. These hypotheses all warrant additional investigation to further delineate the robust nature of this methodology.

In conclusion, this chapter described electrokinetic transport over wide tissue areas with considerable volumes of impacted tissue, with comparison to pressure-driven infusion. Because electrokinetic transport impacted a substantially greater volume of tissue than by diffusion alone, it represents a novel form of convection-enhanced delivery. Future investigation will focus on the application of this methodology to malignant brain gliomas, though it remains pertinent to all matrices with a ζ-potential and the capacity for electrokinetic transport.

5.5 ACKNOWLEDGEMENTS

This work was made possible by grant numbers UL1 RR024153 from the National Center for Research Resources (NCRR) and R01 GM044842 from the National Institute of General Medical Sciences, both components of the National Institutes of Health (NIH). The *in vivo* work was completed with Andrea Jaquins-Gerstl. Special thanks goes to Chuck Fleishaker and Tom Gasmire in the Department of Chemistry electronics and machine shops for their respective assistance in developing the electronics and setup required for these experiments.

REFERENCES

1. Savtchenko, L. P.; Kulahin, N.; Korogod, S. M.; Rusakov, D. A., Electric fields of synaptic currents could influence diffusion of charged neurotransmitter molecules. *Synapse* **2004,** 51, (4), 270-8.
2. Anastassiou, C. A.; Montgomery, S. M.; Barahona, M.; Buzsaki, G.; Koch, C., The effect of spatially inhomogeneous extracellular electric fields on neurons. *J Neurosci* **2010,** 30, (5), 1925-36.
3. Jefferys, J. G., Nonsynaptic modulation of neuronal activity in the brain: electric currents and extracellular ions. *Physiol Rev* **1995,** 75, (4), 689-723.
4. Frohlich, F.; McCormick, D. A., Endogenous electric fields may guide neocortical network activity. *Neuron* **2010,** 67, (1), 129-43.
5. Chang, B. S.; Lowenstein, D. H., Epilepsy. *N Engl J Med* **2003,** 349, (13), 1257-66.
6. Leao, A., Spreading depression of activity in cerebral cortex. *J Neurophysiol* **1944,** 7, 359-390.
7. Eikermann-Haerter, K.; Ayata, C., Cortical spreading depression and migraine. *Curr Neurol Neurosci Rep* **2010,** 10, (3), 167-73.
8. Somjen, G. G., Mechanisms of spreading depression and hypoxic spreading depression-like depolarization. *Physiol Rev* **2001,** 81, (3), 1065-96.

9. Hartings, J. A.; Strong, A. J.; Fabricius, M.; Manning, A.; Bhatia, R.; Dreier, J. P.; Mazzeo, A. T.; Tortella, F. C.; Bullock, M. R., Spreading depolarizations and late secondary insults after traumatic brain injury. *J Neurotrauma* **2009,** 26, (11), 1857-66.

10. Dohmen, C.; Sakowitz, O. W.; Fabricius, M.; Bosche, B.; Reithmeier, T.; Ernestus, R. I.; Brinker, G.; Dreier, J. P.; Woitzik, J.; Strong, A. J.; Graf, R., Spreading depolarizations occur in human ischemic stroke with high incidence. *Ann Neurol* **2008,** 63, (6), 720-8.

11. Dreier, J. P.; Woitzik, J.; Fabricius, M.; Bhatia, R.; Major, S.; Drenckhahn, C.; Lehmann, T. N.; Sarrafzadeh, A.; Willumsen, L.; Hartings, J. A.; Sakowitz, O. W.; Seemann, J. H.; Thieme, A.; Lauritzen, M.; Strong, A. J., Delayed ischaemic neurological deficits after subarachnoid haemorrhage are associated with clusters of spreading depolarizations. *Brain* **2006,** 129, (Pt 12), 3224-37.

12. Gorelova, N. A.; Koroleva, V. I.; Amemori, T.; Pavlik, V.; Bures, J., Ketamine blockade of cortical spreading depression in rats. *Electroencephalogr Clin Neurophysiol* **1987,** 66, (4), 440-7.

13. Gorji, A.; Scheller, D.; Straub, H.; Tegtmeier, F.; Kohling, R.; Hohling, J. M.; Tuxhorn, I.; Ebner, A.; Wolf, P.; Werner Panneck, H.; Oppel, F.; Speckmann, E. J., Spreading depression in human neocortical slices. *Brain Res* **2001,** 906, (1-2), 74-83.

14. Jorgensen, P. L.; Hakansson, K. O.; Karlish, S. J., Structure and mechanism of Na,K-ATPase: functional sites and their interactions. *Annu Rev Physiol* **2003,** 65, 817-49.

15. D'Ambrosio, R.; Gordon, D. S.; Winn, H. R., Differential role of KIR channel and Na^+/K^+-pump in the regulation of extracellular K^+ in rat hippocampus. *J Neurophysiol* **2002,** 87, (1), 87-102.

16. Dichgans, M.; Freilinger, T.; Eckstein, G.; Babini, E.; Lorenz-Depiereux, B.; Biskup, S.; Ferrari, M. D.; Herzog, J.; van den Maagdenberg, A. M.; Pusch, M.; Strom, T. M., Mutation in the neuronal voltage-gated sodium channel SCN1A in familial hemiplegic migraine. *Lancet* **2005,** 366, (9483), 371-7.

17. Johnston, D.; Magee, J. C.; Colbert, C. M.; Cristie, B. R., Active properties of neuronal dendrites. *Annu Rev Neurosci* **1996,** 19, 165-86.

18. Moskowitz, M. A.; Bolay, H.; Dalkara, T., Deciphering migraine mechanisms: clues from familial hemiplegic migraine genotypes. *Ann Neurol* **2004,** 55, (2), 276-80.

19. Ranck, J. B., Jr., Synaptic "Learning" Due to Electroosmosis: a Theory. *Science* **1964,** 144, 187-9.

20. Probstein, R., Physiochemical Hydrodynamics, An Introduction: Second Edition. **1994**.

21. Guy, Y.; Sandberg, M.; Weber, S. G., Determination of zeta-potential in rat organotypic hippocampal cultures. *Biophys J* **2008,** 94, (11), 4561-9.

22. Guy, Y.; Muha, R. J.; Sandberg, M.; Weber, S. G., Determination of zeta-potential and tortuosity in rat organotypic hippocampal cultures from electroosmotic velocity measurements under feedback control. *Anal Chem* **2009,** 81, (8), 3001-7.

23. Stone, T. W., *Microiontophoresis and pressure ejection.* Wiley: Chichester, 1985.

24. von Helmholtz, H., Studien über electrische Grenzschichten. *Annalen der Physik und Chemie* **1879,** 7, 337-382.

25. Gouy, G., *Phys. Radium (Paris)* **1910,** 9, 457.

26. Chapman, D., *Philos. Mag.* **1913,** 25, (475).

27. Stern, O., The theory of the electrolytic double-layer. *Zeit. Elektrochem.* **1924,** 30, 508.

28. Sykova, E.; Nicholson, C., Diffusion in brain extracellular space. *Physiol Rev* **2008,** 88, (4), 1277-340.

29. Epstein, N., On tortuosity and the tortuosity factor in flow and diffusion through porous media. *Chemical Engineering Science* **1989,** 44, (3), 777-779.

30. Fick, A., Ueber Diffusion. *Annalen der Physik* **1855,** 170, (1), 59-86.

31. Loren, N.; Nyden, M.; Hermansson, A. M., Determination of local diffusion properties in heterogeneous biomaterials. *Adv Colloid Interface Sci* **2009,** 150, (1), 5-15.

32. Anderova, M.; Kubinova, S.; Mazel, T.; Chvatal, A.; Eliasson, C.; Pekny, M.; Sykova, E., Effect of elevated K^+, hypotonic stress, and cortical spreading depression on astrocyte swelling in GFAP-deficient mice. *Glia* **2001,** 35, (3), 189-203.

33. Cragg, S. J.; Nicholson, C.; Kume-Kick, J.; Tao, L.; Rice, M. E., Dopamine-mediated volume transmission in midbrain is regulated by distinct extracellular geometry and uptake. *J Neurophysiol* **2001,** 85, (4), 1761-71.

34. Cserr, H. F.; DePasquale, M.; Nicholson, C.; Patlak, C. S.; Pettigrew, K. D.; Rice, M. E., Extracellular volume decreases while cell volume is maintained by ion uptake in rat brain during acute hypernatremia. *J Physiol* **1991,** 442, 277-95.

35. Homola, A.; Zoremba, N.; Slais, K.; Kuhlen, R.; Sykova, E., Changes in diffusion parameters, energy-related metabolites and glutamate in the rat cortex after transient hypoxia/ischemia. *Neurosci Lett* **2006,** 404, (1-2), 137-42.

36. Hrabetova, S., Extracellular diffusion is fast and isotropic in the stratum radiatum of hippocampal CA1 region in rat brain slices. *Hippocampus* **2005,** 15, (4), 441-50.

37. Hrabetova, S.; Nicholson, C., Dextran decreases extracellular tortuosity in thick-slice ischemia model. *J Cereb Blood Flow Metab* **2000,** 20, (9), 1306-10.

38. Krizaj, D.; Rice, M. E.; Wardle, R. A.; Nicholson, C., Water compartmentalization and extracellular tortuosity after osmotic changes in cerebellum of Trachemys scripta. *J Physiol* **1996,** 492 (Pt 3), 887-96.

39. Kume-Kick, J.; Mazel, T.; Vorisek, I.; Hrabetova, S.; Tao, L.; Nicholson, C., Independence of extracellular tortuosity and volume fraction during osmotic challenge in rat neocortex. *J Physiol* **2002,** 542, (Pt 2), 515-27.

40. Lehmenkuhler, A.; Sykova, E.; Svoboda, J.; Zilles, K.; Nicholson, C., Extracellular space parameters in the rat neocortex and subcortical white matter during postnatal development determined by diffusion analysis. *Neuroscience* **1993,** 55, (2), 339-51.

41. Mazel, T.; Richter, F.; Vargova, L.; Sykova, E., Changes in extracellular space volume and geometry induced by cortical spreading depression in immature and adult rats. *Physiol Res* **2002,** 51 Suppl 1, S85-93.

42. Mazel, T.; Simonova, Z.; Sykova, E., Diffusion heterogeneity and anisotropy in rat hippocampus. *Neuroreport* **1998,** 9, (7), 1299-304.

43. McBain, C. J.; Traynelis, S. F.; Dingledine, R., Regional variation of extracellular space in the hippocampus. *Science* **1990,** 249, (4969), 674-7.

44. Nicholson, C.; Phillips, J. M., Ion diffusion modified by tortuosity and volume fraction in the extracellular microenvironment of the rat cerebellum. *J Physiol* **1981,** 321, 225-57.

45. Perez-Pinzon, M. A.; Tao, L.; Nicholson, C., Extracellular potassium, volume fraction, and tortuosity in rat hippocampal CA1, CA3, and cortical slices during ischemia. *J Neurophysiol* **1995,** 74, (2), 565-73.

46. Piet, R.; Vargova, L.; Sykova, E.; Poulain, D. A.; Oliet, S. H., Physiological contribution of the astrocytic environment of neurons to intersynaptic crosstalk. *Proc Natl Acad Sci U S A* **2004,** 101, (7), 2151-5.

47. Rice, M. E.; Okada, Y. C.; Nicholson, C., Anisotropic and heterogeneous diffusion in the turtle cerebellum: implications for volume transmission. *J Neurophysiol* **1993,** 70, (5), 2035-44.

48. Slais, K.; Vorisek, I.; Zoremba, N.; Homola, A.; Dmytrenko, L.; Sykova, E., Brain metabolism and diffusion in the rat cerebral cortex during pilocarpine-induced status epilepticus. *Exp Neurol* **2008,** 209, (1), 145-54.

49. Sykova, E.; Fiala, J.; Antonova, T.; Vorisek, I., Extracellular space volume changes and diffusion barriers in rats with kaolin-induced and inherited hydrocephalus. *Eur J Pediatr Surg* **2001,** 11 Suppl 1, S34-7.

50. Sykova, E.; Mazel, T.; Simonova, Z., Diffusion constraints and neuron-glia interaction during aging. *Exp Gerontol* **1998,** 33, (7-8), 837-51.

51. Sykova, E.; Mazel, T.; Hasenohrl, R. U.; Harvey, A. R.; Simonova, Z.; Mulders, W. H.; Huston, J. P., Learning deficits in aged rats related to decrease in extracellular volume and loss of diffusion anisotropy in hippocampus. *Hippocampus* **2002,** 12, (2), 269-79.

52. Sykova, E.; Vorisek, I.; Mazel, T.; Antonova, T.; Schachner, M., Reduced extracellular space in the brain of tenascin-R- and HNK-1-sulphotransferase deficient mice. *Eur J Neurosci* **2005,** 22, (8), 1873-80.

53. Sykova, E.; Vorisek, I.; Antonova, T.; Mazel, T.; Meyer-Luehmann, M.; Jucker, M.; Hajek, M.; Ort, M.; Bures, J., Changes in extracellular space size and geometry in APP23

transgenic mice: a model of Alzheimer's disease. *Proc Natl Acad Sci U S A* **2005,** 102, (2), 479-84.

54. van der Toorn, A.; Sykova, E.; Dijkhuizen, R. M.; Vorisek, I.; Vargova, L.; Skobisova, E.; van Lookeren Campagne, M.; Reese, T.; Nicolay, K., Dynamic changes in water ADC, energy metabolism, extracellular space volume, and tortuosity in neonatal rat brain during global ischemia. *Magn Reson Med* **1996,** 36, (1), 52-60.

55. Vargova, L.; Homola, A.; Zamecnik, J.; Tichy, M.; Benes, V.; Sykova, E., Diffusion parameters of the extracellular space in human gliomas. *Glia* **2003,** 42, (1), 77-88.

56. Vorisek, I.; Sykova, E., Evolution of anisotropic diffusion in the developing rat corpus callosum. *J Neurophysiol* **1997,** 78, (2), 912-9.

57. Vorisek, I.; Sykova, E., Ischemia-induced changes in the extracellular space diffusion parameters, K^+, and pH in the developing rat cortex and corpus callosum. *J Cereb Blood Flow Metab* **1997,** 17, (2), 191-203.

58. Zoremba, N.; Homola, A.; Rossaint, R.; Sykova, E., Brain metabolism and extracellular space diffusion parameters during and after transient global hypoxia in the rat cortex. *Exp Neurol* **2007,** 203, (1), 34-41.

59. Nicholson, C.; Tao, L., Hindered diffusion of high molecular weight compounds in brain extracellular microenvironment measured with integrative optical imaging. *Biophys J* **1993,** 65, (6), 2277-90.

60. Tao, L.; Nicholson, C., Diffusion of albumins in rat cortical slices and relevance to volume transmission. *Neuroscience* **1996,** 75, (3), 839-47.

61. Thorne, R. G.; Nicholson, C., In vivo diffusion analysis with quantum dots and dextrans predicts the width of brain extracellular space. *Proc Natl Acad Sci U S A* **2006,** 103, (14), 5567-72.

62. Xiao, F.; Nicholson, C.; Hrabe, J.; Hrabetova, S., Diffusion of flexible random-coil dextran polymers measured in anisotropic brain extracellular space by integrative optical imaging. *Biophys J* **2008,** 95, (3), 1382-92.

63. Prokopova-Kubinova, S.; Vargova, L.; Tao, L.; Ulbrich, K.; Subr, V.; Sykova, E.; Nicholson, C., Poly[*N*-(2-hydroxypropyl)methacrylamide] polymers diffuse in brain extracellular space with same tortuosity as small molecules. *Biophys J* **2001,** 80, (1), 542-8.

64. Stroh, M.; Zipfel, W. R.; Williams, R. M.; Ma, S. C.; Webb, W. W.; Saltzman, W. M., Multiphoton microscopy guides neurotrophin modification with poly(ethylene glycol) to enhance interstitial diffusion. *Nat Mater* **2004,** 3, (7), 489-94.

65. Thorne, R. G.; Hrabetova, S.; Nicholson, C., Diffusion measurements for drug design. *Nat Mater* **2005,** 4, (10), 713; author reply 714.

66. Fenstermacher, J. D.; Patlak, C. S.; Blasberg, R. G., Transport of material between brain extracellular fluid, brain cells and blood. *Fed Proc* **1974,** 33, (9), 2070-4.

67. Fenstermacher, J.; Kaye, T., Drug "diffusion" within the brain. *Ann N Y Acad Sci* **1988,** 531, 29-39.

68. Rosenberg, G. A.; Kyner, W. T.; Estrada, E., Bulk flow of brain interstitial fluid under normal and hyperosmolar conditions. *Am J Physiol* **1980,** 238, (1), F42-9.

69. Patlak, C. S.; Fenstermacher, J. D., Measurements of dog blood-brain transfer constants by ventriculocisternal perfusion. *Am J Physiol* **1975,** 229, (4), 877-84.

70. Kohling, R.; Lehmenkukhler, A.; Nicholson, C.; Speckmann, E. J., Superfusion of verapamil on the cerebral cortex does not suppress epileptic discharges due to restricted diffusion (rats, in vivo). *Brain Res* **1993,** 626, (1-2), 149-55.

71. Lehmenkuhler, A.; Kersting, U.; Nicholson, C., Diffusion of penicillin in agar and cerebral cortex of the rat. *Brain Res* **1988,** 444, (1), 181-3.

72. Lucke, A.; Lehmenkuhler, A.; Altrup, U.; Nicholson, C.; Reith, H.; Schmitz-Moormann, C.; Speckmann, E. J., Diffusion analysis of valproate and trans-2-en-valproate in agar and in cerebral cortex of the rat. *Brain Res* **1993,** 631, (2), 187-90.

73. Nicholson, C.; Rice, M. E., Calcium diffusion in the brain cell microenvironment. *Can J Physiol Pharmacol* **1987,** 65, (5), 1086-91.

74. Schwindt, W.; Nicholson, C.; Lehmenkuhler, A., Critical volume of rat cortex and extracellular threshold concentration for a pentylenetetrazol-induced epileptic focus. *Brain Res* **1997,** 753, (1), 86-97.

75. Thorne, R. G.; Lakkaraju, A.; Rodriguez-Boulan, E.; Nicholson, C., In vivo diffusion of lactoferrin in brain extracellular space is regulated by interactions with heparan sulfate. *Proc Natl Acad Sci U S A* **2008,** 105, (24), 8416-21.

76. Ogston, A., The spaces in a uniform random suspension of fibres. *Trans. Faraday Soc.* **1958,** 54, 1754-1757.

77. De Gennes, P., Reptation of a polymer chain in the presence of fixed obstacles. *J. Chem. Phys.* **1971,** 55, (2), 572-579.

78. Hoagland, D.; Muthukumar, M., Evidence for Entropic Barrier Transport in Linear, Star, and Ring Macromolecules in Electrophoresis Gels. *Macromolecules* **1992,** 25, (24), 6696-6698.

79. Rodbard, D.; Chrambach, A., Unified theory for gel electrophoresis and gel filtration. *Proc Natl Acad Sci U S A* **1970,** 65, (4), 970-7.

80. Pluen, A.; Netti, P. A.; Jain, R. K.; Berk, D. A., Diffusion of macromolecules in agarose gels: comparison of linear and globular configurations. *Biophys J* **1999,** 77, (1), 542-52.

81. Nykypanchuk, D.; Strey, H. H.; Hoagland, D. A., Brownian motion of DNA confined within a two-dimensional array. *Science* **2002,** 297, (5583), 987-90.

82. Monro, A., *Observations on structure and functions of the nervous system.* Creech and Johnson: Edinburgh, 1783.

83. Mokri, B., The Monro-Kellie hypothesis: applications in CSF volume depletion. *Neurology* **2001,** 56, (12), 1746-8.

84. Kellie, G., Appearances observed in the dissection of two individuals; death from cold and congestion of the brain. *Trans. Med-Chir. Soc. Edinburgh* **1824,** 1, 84.

85. Linninger, A. A.; Somayaji, M. R.; Mekarski, M.; Zhang, L., Prediction of convection-enhanced drug delivery to the human brain. *J Theor Biol* **2008,** 250, (1), 125-38.

86. Moseley, M. E.; Cohen, Y.; Kucharczyk, J.; Mintorovitch, J.; Asgari, H. S.; Wendland, M. F.; Tsuruda, J.; Norman, D., Diffusion-weighted MR imaging of anisotropic water diffusion in cat central nervous system. *Radiology* **1990,** 176, (2), 439-45.

87. Basser, P. J.; Mattiello, J.; LeBihan, D., MR diffusion tensor spectroscopy and imaging. *Biophys J* **1994,** 66, (1), 259-67.

88. Mori, S.; Crain, B. J.; Chacko, V. P.; van Zijl, P. C., Three-dimensional tracking of axonal projections in the brain by magnetic resonance imaging. *Ann Neurol* **1999,** 45, (2), 265-9.

89. Ito, U.; Reulen, H.; Tomita, H.; Ikeda, J.; Saito, J.; Maehara, T., *Brain Edema*. Raven: New York, 1990.

90. Andersen, P.; Morris, R.; Amaral, D.; Bliss, T.; O'Keefe, J., *The Hippocampus Book*. First ed.; Oxford University Press, USA: 2006.

91. Gahwiler, B. H.; Capogna, M.; Debanne, D.; McKinney, R. A.; Thompson, S. M., Organotypic slice cultures: a technique has come of age. *Trends Neurosci* **1997,** 20, (10), 471-7.

92. Stoppini, L.; Buchs, P. A.; Muller, D., A simple method for organotypic cultures of nervous tissue. *J Neurosci Methods* **1991,** 37, (2), 173-82.

93. Guy, Y.; Rupert, A. E.; Sandberg, M.; Weber, S. G., A simple method for measuring organotypic tissue slice culture thickness. *J Neurosci Methods* **2011,** 199, (1), 78-81.

94. Starling, E., On the absorption of fluids from the connective tissue spaces. *J. Physiological Soc.* **1896,** 19, 312-326.

95. Starling, E., Physiological factors involved in the causation of dropsy. *Lancet* **1896,** May.

96. Deen, W. M.; Robertson, C. R.; Brenner, B. M., A model of glomerular ultrafiltration in the rat. *Am J Physiol* **1972,** 223, (5), 1178-83.

97. Korthuis, R. J.; Wang, C. Y.; Spielman, W. S., Transient effects of histamine on the capillary filtration coefficient. *Microvasc Res* **1984,** 28, (3), 322-44.

98. Fenstermacher, J. D.; Johnson, J. A., Filtration and reflection coefficients of the rabbit blood-brain barrier. *Am J Physiol* **1966,** 211, (2), 341-6.

99. Paulson, O. B.; Hertz, M. M.; Bolwig, T. G.; Lassen, N. A., Filtration and diffusion of water across the blood-brain barrier in man. *Microvasc Res* **1977,** 13, (1), 113-24.

100. Xu, H.; Guy, Y.; Hamsher, A.; Shi, G.; Sandberg, M.; Weber, S. G., Electroosmotic sampling. Application to determination of ectopeptidase activity in organotypic hippocampal slice cultures. *Anal Chem* **2010,** 82, (15), 6377-83.

101. Hamsher, A. E.; Xu, H.; Guy, Y.; Sandberg, M.; Weber, S. G., Minimizing tissue damage in electroosmotic sampling. *Anal Chem* **2010,** 82, (15), 6370-6.

102. Raymond, S.; Weintraub, L., Acrylamide gel as a supporting medium for zone electrophoresis. *Science (Washington, DC, U. S.)* **1959,** 130, 711.

103. Raymond, S.; Nakamichi, M.; Aurell, B., Acrylamide gel as an electrophoresis medium. *Nature (London, U. K.)* **1962,** 195, 697-8.

104. Hjerten, S., "Molecular-sieve" electrophoresis in cross-linked polyacrylamide gels. *J. Chromatogr.* **1963,** 11, 66-70.

105. Keutel, H. J.; Ammons, C. R., Jr.; Boyce, W. H., Synthetic gel, polyacrylamide, as a medium for microimmunoelectrophoresis. *Invest. Urol.* **1964,** 2, (1), 22-9.

106. Cole, K. D.; Tellez, C. M.; Nguyen, R. B., Modification of the electrokinetic properties of reversible electrophoresis gels for the separation and preparation of DNA: addition of linear polymers. *Appl. Biochem. Biotechnol.* **1999,** 82, (1), 57-76.

107. Matos, M. A.; White, L. R.; Tilton, R. D., Electroosmotically enhanced mass transfer through polyacrylamide gels. *J. Colloid Interface Sci.* **2006,** 300, (1), 429-436.

108. Markstroem, M.; Cole, K. D.; Kerman, B., DNA electrophoresis in gellan gels. The effect of electroosmosis and polymer additives. *J. Phys. Chem. B* **2002,** 106, (9), 2349-2356.

109. Lengyel, T.; Guttman, A., Effect of linear polymer additives on the electroosmotic characteristics of agarose gels in ultrathin-layer electrophoresis. *J. Chromatogr., A* **1999,** 853, (1 + 2), 511-518.

110. Fujimoto, C.; Kino, J.; Sawada, H., Capillary electrochromatography of small molecules in polyacrylamide gels with electroosmotic flow. *J. Chromatogr., A* **1995,** 716, (1 + 2), 107-13.

111. Wu, M.; Wu, R. a.; Wang, F.; Ren, L.; Dong, J.; Liu, Z.; Zou, H., "One-Pot" Process for Fabrication of Organic-Silica Hybrid Monolithic Capillary Columns Using Organic Monomer and Alkoxysilane. *Anal. Chem. (Washington, DC, U. S.)* **2009,** 81, (9), 3529-3536.

112. Koide, T.; Ueno, K., Enantiomeric separations by capillary electrochromatography with charged polyacrylamide gels incorporating chiral selectors. *Anal. Sci.* **2000,** 16, (10), 1065-1070.

113. Koide, T.; Ueno, K., Enantiomeric separations of primary amino compounds by capillary electrochromatography with monolithic chiral stationary phases of chiral crown ether-bonded negatively charged polyacrylamide gels. *J. Chromatogr., A* **2001,** 909, (2), 305-315.

114. Sui, Z.; Schlenoff, J. B., Phase separations in pH-responsive polyelectrolyte multilayers: charge extrusion versus charge expulsion. *Langmuir* **2004,** 20, (14), 6026-31.

115. Akaneya, Y.; Jiang, B.; Tsumoto, T., RNAi-induced gene silencing by local electroporation in targeting brain region. *J Neurophysiol* **2005,** 93, (1), 594-602.

116. Gluckman, B. J.; Nguyen, H.; Weinstein, S. L.; Schiff, S. J., Adaptive electric field control of epileptic seizures. *J Neurosci* **2001,** 21, (2), 590-600.

117. LeBeau, F. E.; Malmierca, M. S.; Rees, A., Iontophoresis in vivo demonstrates a key role for $GABA_A$ and glycinergic inhibition in shaping frequency response areas in the inferior colliculus of guinea pig. *J Neurosci* **2001,** 21, (18), 7303-12.

118. Lerner, E. N.; van Zanten, E. H.; Stewart, G. R., Enhanced delivery of octreotide to the brain via transnasal iontophoretic administration. *J Drug Target* **2004,** 12, (5), 273-80.

119. McCaig, C. D.; Sangster, L.; Stewart, R., Neurotrophins enhance electric field-directed growth cone guidance and directed nerve branching. *Dev Dyn* **2000,** 217, (3), 299-308.

120. Miranda, P. C.; Hallett, M.; Basser, P. J., The electric field induced in the brain by magnetic stimulation: a 3-D finite-element analysis of the effect of tissue heterogeneity and anisotropy. *IEEE Trans Biomed Eng* **2003,** 50, (9), 1074-85.

121. Pikal, M. J., The role of electroosmotic flow in transdermal iontophoresis. *Adv Drug Deliv Rev* **2001,** 46, (1-3), 281-305.

122. Beisler, A. T.; Schaefer, K. E.; Weber, S. G., Simple method for the quantitative examination of extra column band broadening in microchromatographic systems. *J Chromatogr A* **2003,** 986, (2), 247-51.

123. Hong, W.; Zhao, X.; Suo, Z., Large deformation and electrochemistry of polyelectrolyte gels. *Journal of the Mechanics and Physics of Solids* **2010,** 58, (4), 558-577.

124. Shiga, T.; Hirose, Y.; Okada, A.; Kurauchi, T., Electric field-associated deformation of polyelectrolyte gel near a phase transition point. *Journal of Applied Polymer Science* **1992,** 46, (4), 635-640.

125. Shiga, T.; Hirose, Y.; Okada, A.; Kurauchi, T., Bending of poly(vinyl alcohol)-poly(sodium acrylate) composite hydrogel in electric fields. *Journal of Applied Polymer Science* **1992,** 44, (2), 249-253.

126. Shiga, T.; Hirose, Y.; Okada, A.; Kurauchi, T., Bending of ionic polymer gel caused by swelling under sinusoidally varying electric fields. *Journal of Applied Polymer Science* **1993,** 47, (1), 113-119.

127. Shiga, T.; Kurauchi, T., Deformation of polyelectrolyte gels under the influence of electric field. *Journal of Applied Polymer Science* **1990,** 39, (11-12), 2305-2320.

128. Jabbari, E.; Tavakoli, J.; Sarvestani, A. S., Swelling characteristics of acrylic acid polyelectrolyte hydrogel in a dc electric field. *Smart Materials and Structures* **2007,** 15, (5), 1614-1620.

129. Osada, Y.; Okuzaki, H.; Hori, H., A polymer gel with electrically driven motility. *Nature* **1992,** 355, 242-244.

130. Budtova, T.; Navard, P., Hydrogel suspensions as an electro-rheological fluid. *Polymer* **2001,** 42, 4853-4858.

131. Sykova, E., Extrasynaptic volume transmission and diffusion parameters of the extracellular space. *Neuroscience* **2004,** 129, (4), 861-76.

132. Heegaard, N. H., Affinity in electrophoresis. *Electrophoresis* **2009,** 30 Suppl 1, S229-39.

133. Meagher, R. J.; Won, J. I.; McCormick, L. C.; Nedelcu, S.; Bertrand, M. M.; Bertram, J. L.; Drouin, G.; Barron, A. E.; Slater, G. W., End-labeled free-solution electrophoresis of DNA. *Electrophoresis* **2005,** 26, (2), 331-50.

134. Kleparnik, K.; Bocek, P., Electrophoresis today and tomorrow: Helping biologists' dreams come true. *Bioessays* **2010,** 32, (3), 218-26.

135. Stellwagen, N. C., Apparent pore size of polyacrylamide gels: comparison of gels cast and run in Tris-acetate-EDTA and Tris-borate-EDTA buffers. *Electrophoresis* **1998,** 19, (10), 1542-7.

136. Curtis, D. R.; Perrin, D. D.; Watkins, J. C., The excitation of spinal neurones by the ionophoretic application of agents which chelate calcium. *J Neurochem* **1960,** 6, 1-20.

137. Lux, H. D.; Neher, E., The equilibration time course of K^+ in cat cortex. *Exp Brain Res* **1973,** 17, (2), 190-205.

138. Nicholson, C.; Phillips, J. M.; Gardner-Medwin, A. R., Diffusion from an iontophoretic point source in the brain: role of tortuosity and volume fraction. *Brain Res* **1979,** 169, (3), 580-4.

139. Norman, R. S., Diffusional spread of iontophoretically injected ions. *J Theor Biol* **1975,** 52, (1), 159-62.

140. Hao, J.; Li, S. K.; Liu, C.-Y.; Kao, W. W. Y., Electrically assisted delivery of macromolecules into the corneal epithelium. *Exp. Eye Res. FIELD Full Journal Title:Experimental Eye Research* **2009,** 89, (6), 934-941.

141. Hughes, M., Ocular drug delivery: expanding the field of vision. *Drug Delivery Technology* **2009,** 9, (4), 34-35.

142. Colombo, R.; Brausi, M.; Da Pozzo, L.; Salonia, A.; Montorsi, F.; Scattoni, V.; Roscigno, M.; Rigatti, P., Thermo-chemotherapy and electromotive drug administration of mitomycin C in superficial bladder cancer eradication. a pilot study on marker lesion. *Eur Urol FIELD Full Journal Title:European urology* **2001,** 39, (1), 95-100.

143. Barcroft, H.; Bonnar, W.; Edholm, O.; Effron, A., On sympathetic vasoconstrictor tone in human skeletal muscle. *J. Physiol.* **1943,** 102, 21-31.

144. Curtis, D. R.; Eccles, R. M., The effect of diffusional barriers upon the pharmacology of cells within the central nervous system. *J Physiol* **1958,** 141, (3), 446-63.

145. Curtis, D. R.; Eccles, R. M., The excitation of Renshaw cells by pharmacological agents applied electrophoretically. *J Physiol* **1958,** 141, (3), 435-45.

146. Curtis, D. R., A method for assembly of "parallel" micro-pipettes. *Electroencephalogr Clin Neurophysiol* **1968,** 24, (6), 587-9.

147. Bevan, P.; Bradshaw, C. M.; Pun, R. Y.; Slater, N. T.; Szabadi, E., Electro-osmotic and iontophoretic release of noradrenaline from micropipettes. *Experientia* **1981,** 37, (3), 296-7.

148. Hicks, T. P., The history and development of microiontophoresis in experimental neurobiology. *Prog Neurobiol* **1984,** 22, (3), 185-240.

149. Murthy, A.; Humphrey, A. L., Inhibitory contributions to spatiotemporal receptive-field structure and direction selectivity in simple cells of cat area 17. *J Neurophysiol* **1999,** 81, (3), 1212-24.

150. Hill-Smith, I.; Purves, R. D., Synaptic delay in the heart: an ionophoretic study. *J Physiol* **1978,** 279, 31-54.

151. Herr, N. R.; Kile, B. M.; Carelli, R. M.; Wightman, R. M., Electroosmotic flow and its contribution to iontophoretic delivery. *Anal Chem* **2008,** 80, (22), 8635-41.

152. Hoffer, B. J.; Neff, N. H.; Siggins, G. R., Microiontophoretic release of norepinephrine from micropipettes. *Neuropharmacology* **1971,** 10, (21), 175-80.

153. Clarke, G.; Hill, R. G.; Simmonds, M. A., Microiontophoretic release of drugs from micropipettes: use of ^{24}Na as a model. *Br J Pharmacol* **1973,** 48, (1), 156-61.

154. Purves, R. D., Iontophoresis - progress and pitfalls. *Trends in Neurosciences* **1980,** 3, (10), 245-247.

155. Shoemaker, W. J.; Balentine, L. T.; Siggins, G. R.; Hoffer, B. J.; Henriksen, S. J.; Bloom, F. E., Characteristics of the release of adenosine 3':5'-monophosphate from micropipets by microiontophoresis. *J Cyclic Nucleotide Res* **1975,** 1, (2), 97-106.

156. Bloom, F. E., To spritz or not to spritz: the doubtful value of aimless iontophoresis. *Life Sci* **1974,** 14, (10), 1819-34.

157. Dionne, V. E., Characterization of drug iontophoresis with a fast microassay technique. *Biophys J* **1976,** 16, (7), 705-17.

158. Chen, K. C.; Nicholson, C., Measurement of diffusion parameters using a sinusoidal iontophoretic source in rat cortex. *J Neurosci Methods* **2002,** 122, (1), 97-108.

159. Hrabetova, S.; Masri, D.; Tao, L.; Xiao, F.; Nicholson, C., Calcium diffusion enhanced after cleavage of negatively charged components of brain extracellular matrix by chondroitinase ABC. *J Physiol* **2009,** 587, (Pt 16), 4029-49.

160. Herr, N. R.; Daniel, K. B.; Belle, A. M.; Carelli, R. M.; Wightman, R. M., Probing presynaptic regulation of extracellular dopamine with iontophoresis. *ACS Chem Neurosci* **2010,** 1, (9), 627-638.

161. Armstrong-James, M.; Fox, K.; Kruk, Z. L.; Millar, J., Quantitative ionophoresis of catecholamines using multibarrel carbon fibre microelectrodes. *J Neurosci Methods* **1981,** 4, (4), 385-406.

162. Armstrong-James, M.; Millar, J.; Kruk, Z. L., Quantification of noradrenaline iontophoresis. *Nature* **1980,** 288, (5787), 181-3.

163. Purves, R. D., The physics of iontophoretic pipettes. *J Neurosci Methods* **1979,** 1, (2), 165-78.

164. Guy, Y. *Determination and Implications of Electroosmotic Transport in the Brain*. University of Pittsburgh, Pittsburgh, PA, 2010.

165. Scott, E. R.; Laplaza, A. I.; White, H. S.; Phipps, J. B., Transport of ionic species in skin: contribution of pores to the overall skin conductance. *Pharm Res* **1993,** 10, (12), 1699-709.

166. Uitto, O. D.; White, H. S., Electroosmotic pore transport in human skin. *Pharm Res* **2003,** 20, (4), 646-52.

167. Trubatch, J.; Van Harreveld, A., Spread of iontophoretically injected ions in a tissue. *J Theor Biol* **1972,** 36, (2), 355-66.

168. Drouin, H., On microelectrode ionophoresis. *Biophys J* **1984,** 46, (5), 597-604.

169. Noraberg, J.; Kristensen, B. W.; Zimmer, J., Markers for neuronal degeneration in organotypic slice cultures. *Brain Res Brain Res Protoc* **1999,** 3, (3), 278-90.

170. Barz, D. P.; Vogel, M. J.; Steen, P. H., Determination of the zeta potential of porous substrates by droplet deflection. I. The influence of ionic strength and pH value of an aqueous electrolyte in contact with a borosilicate surface. *Langmuir* **2009,** 25, (3), 1842-50.

171. Thormann, W.; Zhang, C.-X.; Caslavska, J.; Gebauer, P.; Mosher, R., Modeling of the impact of ionic strength on the electroosmotic flow in capillary electrophoresis with uniform and discontinuous buffer systems. *Anal Chem* **1998,** 70, (3), 549-562.

172. McGuffin, V.; Tavares, M., Computer-Assisted Optimization of Separations in Capillary Zone Electrophoresis. *Anal Chem* **1997,** 69, (2), 152-164.

173. Scales, P.; Grieser, F.; Healy, T.; White, L.; Chan, D., Electrokinetics of the Silica-Solution Interface: A Flat Plate Streaming Potential Study. *Langmuir* **1992,** 8, (3), 965-974.

174. Scales, N.; Tait, R. N., Modeling electroosmotic and pressure-driven flows in porous microfluidic devices: zeta potential and porosity changes near the channel walls. *J Chem Phys* **2006,** 125, (9), 094714.

175. Zoski, C.; Bond, A.; Allinson, E.; Oldham, K., How long does it take a microelectrode to reach a voltammetric steady state? *Anal Chem* **1990,** 62, (1), 37-45.

176. Ohm, G., *Die galvanische Kette, mathematisch bearbeitet*. T.H. Riemann: Berlin, 1827.

177. Barrande, M.; Bouchet, R.; Denoyel, R., Tortuosity of porous particles. *Anal Chem* **2007,** 79, (23), 9115-21.

178. Kilb, W.; Dierkes, P. W.; Sykova, E.; Vargova, L.; Luhmann, H. J., Hypoosmolar conditions reduce extracellular volume fraction and enhance epileptiform activity in the CA3 region of the immature rat hippocampus. *J Neurosci Res* **2006,** 84, (1), 119-29.

179. Wen, P. Y.; Kesari, S., Malignant gliomas in adults. *N Engl J Med* **2008,** 359, (5), 492-507.

180. Furnari, F. B.; Fenton, T.; Bachoo, R. M.; Mukasa, A.; Stommel, J. M.; Stegh, A.; Hahn, W. C.; Ligon, K. L.; Louis, D. N.; Brennan, C.; Chin, L.; DePinho, R. A.; Cavenee, W. K., Malignant astrocytic glioma: genetics, biology, and paths to treatment. *Genes Dev* **2007,** 21, (21), 2683-710.

181. Ohgaki, H.; Kleihues, P., Genetic pathways to primary and secondary glioblastoma. *Am J Pathol* **2007,** 170, (5), 1445-53.

182. Watanabe, K.; Tachibana, O.; Sata, K.; Yonekawa, Y.; Kleihues, P.; Ohgaki, H., Overexpression of the EGF receptor and p53 mutations are mutually exclusive in the evolution of primary and secondary glioblastomas. *Brain Pathol* **1996,** 6, (3), 217-23; discussion 23-4.

183. Ueki, K.; Ono, Y.; Henson, J. W.; Efird, J. T.; von Deimling, A.; Louis, D. N., CDKN2/p16 or RB alterations occur in the majority of glioblastomas and are inversely correlated. *Cancer Res* **1996,** 56, (1), 150-3.

184. Stupp, R.; Mason, W. P.; van den Bent, M. J.; Weller, M.; Fisher, B.; Taphoorn, M. J.; Belanger, K.; Brandes, A. A.; Marosi, C.; Bogdahn, U.; Curschmann, J.; Janzer, R. C.; Ludwin, S. K.; Gorlia, T.; Allgeier, A.; Lacombe, D.; Cairncross, J. G.; Eisenhauer, E.; Mirimanoff, R. O., Radiotherapy plus concomitant and adjuvant temozolomide for glioblastoma. *N Engl J Med* **2005,** 352, (10), 987-96.

185. Walker, M. D.; Alexander, E., Jr.; Hunt, W. E.; MacCarty, C. S.; Mahaley, M. S., Jr.; Mealey, J., Jr.; Norrell, H. A.; Owens, G.; Ransohoff, J.; Wilson, C. B.; Gehan, E. A.; Strike, T. A., Evaluation of BCNU and/or radiotherapy in the treatment of anaplastic gliomas. A cooperative clinical trial. *J Neurosurg* **1978,** 49, (3), 333-43.

186. Liang, B. C.; Thornton, A. F., Jr.; Sandler, H. M.; Greenberg, H. S., Malignant astrocytomas: focal tumor recurrence after focal external beam radiation therapy. *J Neurosurg* **1991,** 75, (4), 559-63.

187. Brandes, A. A.; Tosoni, A.; Franceschi, E.; Sotti, G.; Frezza, G.; Amista, P.; Morandi, L.; Spagnolli, F.; Ermani, M., Recurrence pattern after temozolomide concomitant with and adjuvant to radiotherapy in newly diagnosed patients with glioblastoma: correlation With MGMT promoter methylation status. *J Clin Oncol* **2009,** 27, (8), 1275-9.

188. Newlands, E. S.; Blackledge, G. R.; Slack, J. A.; Rustin, G. J.; Smith, D. B.; Stuart, N. S.; Quarterman, C. P.; Hoffman, R.; Stevens, M. F.; Brampton, M. H.; et al., Phase I trial of temozolomide (CCRG 81045: M&B 39831: NSC 362856). *Br J Cancer* **1992,** 65, (2), 287-91.

189. Brem, H.; Tamargo, R. J.; Olivi, A.; Pinn, M.; Weingart, J. D.; Wharam, M.; Epstein, J. I., Biodegradable polymers for controlled delivery of chemotherapy with and without radiation therapy in the monkey brain. *J Neurosurg* **1994,** 80, (2), 283-90.

190. Westphal, M.; Hilt, D. C.; Bortey, E.; Delavault, P.; Olivares, R.; Warnke, P. C.; Whittle, I. R.; Jaaskelainen, J.; Ram, Z., A phase 3 trial of local chemotherapy with biodegradable carmustine (BCNU) wafers (Gliadel wafers) in patients with primary malignant glioma. *Neuro Oncol* **2003,** 5, (2), 79-88.

191. Westphal, M.; Ram, Z.; Riddle, V.; Hilt, D.; Bortey, E., Gliadel wafer in initial surgery for malignant glioma: long-term follow-up of a multicenter controlled trial. *Acta Neurochir (Wien)* **2006,** 148, (3), 269-75; discussion 275.

192. Fleming, A. B.; Saltzman, W. M., Pharmacokinetics of the carmustine implant. *Clin Pharmacokinet* **2002,** 41, (6), 403-19.

193. Fung, L. K.; Ewend, M. G.; Sills, A.; Sipos, E. P.; Thompson, R.; Watts, M.; Colvin, O. M.; Brem, H.; Saltzman, W. M., Pharmacokinetics of interstitial delivery of carmustine, 4-hydroperoxycyclophosphamide, and paclitaxel from a biodegradable polymer implant in the monkey brain. *Cancer Res* **1998,** 58, (4), 672-84.

194. Bobo, R. H.; Laske, D. W.; Akbasak, A.; Morrison, P. F.; Dedrick, R. L.; Oldfield, E. H., Convection-enhanced delivery of macromolecules in the brain. *Proc Natl Acad Sci U S A* **1994,** 91, (6), 2076-80.

195. Chen, M. Y.; Lonser, R. R.; Morrison, P. F.; Governale, L. S.; Oldfield, E. H., Variables affecting convection-enhanced delivery to the striatum: a systematic examination of rate of infusion, cannula size, infusate concentration, and tissue-cannula sealing time. *J Neurosurg* **1999,** 90, (2), 315-20.

196. Krauze, M. T.; Saito, R.; Noble, C.; Tamas, M.; Bringas, J.; Park, J. W.; Berger, M. S.; Bankiewicz, K., Reflux-free cannula for convection-enhanced high-speed delivery of therapeutic agents. *J Neurosurg* **2005,** 103, (5), 923-9.

197. Yin, D.; Forsayeth, J.; Bankiewicz, K. S., Optimized cannula design and placement for convection-enhanced delivery in rat striatum. *J Neurosci Methods* **2009,** 187, (1), 46-51.

198. Rosenbluth, K. H.; Luz, M.; Mohr, E.; Mittermeyer, S.; Bringas, J.; Bankiewicz, K. S., Design of an in-dwelling cannula for convection-enhanced delivery. *J Neurosci Methods* **2011,** 196, (1), 118-23.

199. Oh, S.; Odland, R.; Wilson, S. R.; Kroeger, K. M.; Liu, C.; Lowenstein, P. R.; Castro, M. G.; Hall, W. A.; Ohlfest, J. R., Improved distribution of small molecules and viral vectors in the murine brain using a hollow fiber catheter. *J Neurosurg* **2007,** 107, (3), 568-77.

200. Olson, J. J.; Zhang, Z.; Dillehay, D.; Stubbs, J., Assessment of a balloon-tipped catheter modified for intracerebral convection-enhanced delivery. *J Neurooncol* **2008,** 89, (2), 159-68.

201. Lonser, R. R.; Walbridge, S.; Garmestani, K.; Butman, J. A.; Walters, H. A.; Vortmeyer, A. O.; Morrison, P. F.; Brechbiel, M. W.; Oldfield, E. H., Successful and safe perfusion of the primate brainstem: in vivo magnetic resonance imaging of macromolecular distribution during infusion. *J Neurosurg* **2002,** 97, (4), 905-13.

202. Valles, F.; Fiandaca, M. S.; Bringas, J.; Dickinson, P.; LeCouteur, R.; Higgins, R.; Berger, M.; Forsayeth, J.; Bankiewicz, K. S., Anatomic compression caused by high-volume convection-enhanced delivery to the brain. *Neurosurgery* **2009,** 65, (3), 579-85; discussion 585-6.

203. Vogelbaum, M. A.; Sampson, J. H.; Kunwar, S.; Chang, S. M.; Shaffrey, M.; Asher, A. L.; Lang, F. F.; Croteau, D.; Parker, K.; Grahn, A. Y.; Sherman, J. W.; Husain, S. R.; Puri, R. K., Convection-enhanced delivery of cintredekin besudotox (interleukin-13-PE38QQR) followed by radiation therapy with and without temozolomide in newly diagnosed malignant gliomas: phase 1 study of final safety results. *Neurosurgery* **2007,** 61, (5), 1031-7; discussion 1037-8.

204. Hall, W. A.; Rustamzadeh, E.; Asher, A. L., Convection-enhanced delivery in clinical trials. *Neurosurg Focus* **2003,** 14, (2), e2.

205. Patel, S. J.; Shapiro, W. R.; Laske, D. W.; Jensen, R. L.; Asher, A. L.; Wessels, B. W.; Carpenter, S. P.; Shan, J. S., Safety and feasibility of convection-enhanced delivery of Cotara for the treatment of malignant glioma: initial experience in 51 patients. *Neurosurgery* **2005,** 56, (6), 1243-52; discussion 1252-3.

206. Lidar, Z.; Mardor, Y.; Jonas, T.; Pfeffer, R.; Faibel, M.; Nass, D.; Hadani, M.; Ram, Z., Convection-enhanced delivery of paclitaxel for the treatment of recurrent malignant glioma: a phase I/II clinical study. *J Neurosurg* **2004,** 100, (3), 472-9.

207. Sampson, J. H.; Raghavan, R.; Brady, M. L.; Provenzale, J. M.; Herndon, J. E., 2nd; Croteau, D.; Friedman, A. H.; Reardon, D. A.; Coleman, R. E.; Wong, T.; Bigner, D. D.; Pastan, I.; Rodriguez-Ponce, M. I.; Tanner, P.; Puri, R.; Pedain, C., Clinical utility of a patient-specific algorithm for simulating intracerebral drug infusions. *Neuro Oncol* **2007,** 9, (3), 343-53.

208. Sampson, J. H.; Brady, M. L.; Petry, N. A.; Croteau, D.; Friedman, A. H.; Friedman, H. S.; Wong, T.; Bigner, D. D.; Pastan, I.; Puri, R. K.; Pedain, C., Intracerebral infusate distribution by convection-enhanced delivery in humans with malignant gliomas:

descriptive effects of target anatomy and catheter positioning. *Neurosurgery* **2007,** 60, (2 Suppl 1), ONS89-98; discussion ONS98-9.

209. Jagannathan, J.; Walbridge, S.; Butman, J. A.; Oldfield, E. H.; Lonser, R. R., Effect of ependymal and pial surfaces on convection-enhanced delivery. *J Neurosurg* **2008,** 109, (3), 547-52.

210. Sampson, J. H.; Akabani, G.; Archer, G. E.; Berger, M. S.; Coleman, R. E.; Friedman, A. H.; Friedman, H. S.; Greer, K.; Herndon, J. E., 2nd; Kunwar, S.; McLendon, R. E.; Paolino, A.; Petry, N. A.; Provenzale, J. M.; Reardon, D. A.; Wong, T. Z.; Zalutsky, M. R.; Pastan, I.; Bigner, D. D., Intracerebral infusion of an EGFR-targeted toxin in recurrent malignant brain tumors. *Neuro Oncol* **2008,** 10, (3), 320-9.

211. Kunwar, S.; Chang, S.; Westphal, M.; Vogelbaum, M.; Sampson, J.; Barnett, G.; Shaffrey, M.; Ram, Z.; Piepmeier, J.; Prados, M.; Croteau, D.; Pedain, C.; Leland, P.; Husain, S. R.; Joshi, B. H.; Puri, R. K., Phase III randomized trial of CED of IL13-PE38QQR vs Gliadel wafers for recurrent glioblastoma. *Neuro Oncol* **2010,** 12, (8), 871-81.

212. Sampson, J. H.; Archer, G.; Pedain, C.; Wembacher-Schroder, E.; Westphal, M.; Kunwar, S.; Vogelbaum, M. A.; Coan, A.; Herndon, J. E.; Raghavan, R.; Brady, M. L.; Reardon, D. A.; Friedman, A. H.; Friedman, H. S.; Rodriguez-Ponce, M. I.; Chang, S. M.; Mittermeyer, S.; Croteau, D.; Puri, R. K., Poor drug distribution as a possible explanation for the results of the PRECISE trial. *J Neurosurg* **2010,** 113, (2), 301-9.

213. Hendelman, W., *Atlas of Functional Neuroanatomy, Second Edition*. CRC Press: 2000.

214. Renaud, L.; Kleimann, P.; Morin, P., Zeta potential determination by streaming current modelization and measurement in electrophoretic microfluidic systems. *Electrophoresis* **2004,** 25, (1), 123-7.

215. Kirby, B. J.; Hasselbrink, E. F., Jr., Zeta potential of microfluidic substrates: 1. Theory, experimental techniques, and effects on separations. *Electrophoresis* **2004,** 25, (2), 187-202.

216. Agarwal, A.; Zudans, I.; Weber, E. A.; Olofsson, J.; Orwar, O.; Weber, S. G., Effect of cell size and shape on single-cell electroporation. *Anal Chem* **2007,** 79, (10), 3589-96.

217. Medtronic, *Medtronic Kinetra® 7428 Technical Manual - Dual Program Neurostimulator for Deep Brain Stimulation.* Minneapolis, MN, 2008.